# Resolving photoisomerization dynamics via ultrafast UV-visible transient absorption spectroscopy

by
Shyamal Prasad


A thesis
submitted to Victoria University of Wellington
in fulfilment of the
requirements for the degree of
Masters of Science
in Chemistry

Victoria University of Wellington
2014

# Abstract

Transient absorption spectroscopy has been employed to investigate three photo–active compounds; azobenzene, foldamer controlled by azobenzene, and oxazine. These compounds all have absorption in the ultra–violet regions responsible for their photo–active behavior. Due to this, the current transient absorption setup has been modified to extend the probing wavelength range to 320–650 nm, with the possibility of exciting the photo–active molecule in the ultra–violet.

Azobenzene is valuable in benchmarking and optimizing the transient absorption setup, it shows that the detection window has been extended out to 320 nm. By resolving the ground state bleach we have added support for the assignment of the final decay to thermalization in the ground state. Comparison of relaxation lifetime in acetonitrile and tetrahydrofuran shows no noticeable change in the photophysics of isomerization between the two solvents.

The foldamer family excited state relaxation is similar to azobenzene. There is an extension in the $S_1$ branching lifetime from 1.1 ps in azobenzene to 1.7 ps for foldamer 1 and 4.2 ps for foldamer 2. The separation of branching on the $S_1$ surface and relaxation through the $S_1$ to electronic ground state intersection was possible by comparison of azobenzene and foldamer family. The solvent effects show little difference for all members of the foldamer family expect for foldamer 2, suggesting that the dynamics of the azobenzene moiety are not affected by the larger macro–structure of the foldamer.

For oxazine it has been established, by varying solvent polarity, that isomerization happens through three states; bond breakage, transfer to a dark state, and the final photo–isomer. This is confirmed by further studies completed after the introduction of electron withdrawing fluorine atoms. Carbon–oxygen bond cleavage occurs on the picosecond timescale, with solvent dependent rotation occurring in hundreds of picoseconds. Fluorinated oxazine shows a strong solvent dependence with rotation suppressed for all but the most polar of solvents.

# Acknowledgments

This thesis is not just the product of my work but must be credited to the many people that have helped and supported me, from both an academic and personal perspective. The words I leave on this page can not express the gratitude I feel for all the help and support that has come from so many people.

First and foremost I must thank Dr. Justin Hodgkiss his supervision. His knowledge has been invaluable, and I look forward to many more years under his supervision. On countless occasions he has provided the impetus and guidance, helping me develop the skills that have not only been essential for completing this work but will be invaluable for my career in chemistry. His ability to explain things in a simple and concise manner, only conveying the most important points and leaving the rest to be discovered, kept me interested at every step. The knowledge he has available guided me through the tougher aspects and given me the confidence to undertake challenges that I never thought I would achieve. His supervision and guidance has allowed me to grow and understand aspects of chemistry I thought out of my grasp.

I also would like to thank Dr. Amar Flood and Dr. Brendan Burkett, and their students. Without them I would be left without compounds to study. They willingly synthesized the compounds, making the derivatives I requested for further investigation. The exploration of the photophysics of their compounds has just begun, with the possibility of many more compounds being developed. I look forward to further collaboration on the project.

To all the staff, fellow postgraduate students, and friends in the School of Chemical and Physical Sciences at Victoria University of Wellington. I would like to thank you all for chats in the instrument room, and how you contribute to the efficient running of equipment around the university. This has made my time here a pleasure and the university a place I enjoy spending my time. Special thanks must go to my group members who always provide a distraction from my work when needed, or a helping hand to find solutions to the many problems that I encountered. In particular I must

thank Joe Gallaher, not just for the help with proof reading but more importantly always having the answers to any questions in the wet–lab. Alex Barker, and Kai Chen deserve special thanks for their help in teaching me about ultra–fast lasers and their use in spectroscopy, specially transient absorption spectroscopy. Without them putting up with my constant questions, and helping at every step, I would not have been able to complete this thesis.

I must also thank my friends outside of university. You have all been there to provide moral support. With your belief in my ability, and the many games of Risk, have been very appreciated. A special thanks must go to Connie Payne who has read every word of my thesis many times, her support has been invaluable even if it was just a smile to lift my mood in the most difficult times.

I must also mention my family; Mum, Dad, Ved, and Krishan you have all been an important part of my life, helping to shape me into who I am today. Your willingness to put up with my constant questioning of everyday life, to the games of basketball to give me a writing break. Your encouragement and input has been appreciated, and I am so gratefully to know you will be there for in the many years to come.

Grátiás vóbís agó

# Table of Contents

**Abstract** ii

**Acknowledgments** iii

**Table of Contents** v

**List of Figures** vii

**List of Tables** x

**List of Abbreviations** 1

**1 Outline** 2

**2 Transient Absorption Spectroscopy** 5

2.1 Theory of Transient Absorption Spectroscopy . . . . . 5

2.1.1 Data Acquisition . . . . . 6

2.1.2 Experimental Artifacts . . . . . 9

2.2 Transient Absorption Setup . . . . . 16

2.2.1 Non–Linear Optics . . . . . 16

2.2.2 Layout Enhancements . . . . . 18

2.3 Data Analysis . . . . . 24

2.3.1 Artifact Correction . . . . . 24

2.3.2 Wavelength Calibration . . . . . 28

2.3.3 Interpretation of Data . . . . . 29

2.3.4 Data Modeling . . . . . 33

**3 Photo–isomerization of Azobenzene** 38

3.1 Introduction . . . . . 38

3.2 Photo–isomerization . . . . . 39

3.2.1 Mechanism . . . . . 40

3.3 Thermal Isomerization . . . . . 41

3.4 Benchmark and Validation of Transient Absorption Setup . . . . . 43

3.5 Transient Absorption Results . . . . . 44

3.5.1 Effect of Solvent . . . . . 47

3.6 Conclusion . . . . . 48

**4 Light–Controlled Capture and Release Foldamer Molecules 50**

4.1 Molecular Design . . . . . 51
4.2 Chloride Ion and Solvent Effect on Helicity . . . . . 53
4.3 Transient Absorption Spectroscopy . . . . . 54
4.3.1 Structural Effects . . . . . 55
4.3.2 Solvent Effects . . . . . 65
4.3.3 Chloride Ion Effects . . . . . 67
4.4 Conclusion . . . . . 69

**5 Oxazine - Light Activated Switch 70**

5.1 Introduction and Background . . . . . 70
5.2 Transient Absorption Spectroscopy . . . . . 72
5.2.1 Isomerization Mechanism . . . . . 76
5.3 Conclusion . . . . . 84

**6 Future Work 85**

**7 Experimental 87**

**Appendix - Transient Absorption Surfaces 89**

**References 105**

# List of Figures


1.1 Summary of photo–induced changes being studied . . . . . 3

2.1 Instrument layout for transient absorption spectroscopy . . . . . 6
2.2 Three types of transient absorption signals . . . . . 9
2.3 Jablonski diagram showing possible decay pathways . . . . . 10
2.4 Kinetic evolution of transient absorption signal . . . . . 11
2.5 Convolution of pump pulse and transient absorption signal onset . . . 12
2.6 Chirp shown on a transient absorption surface . . . . . 13
2.7 Spectral shape of cross phase modulation . . . . . 14
2.8 Virtual and vibronic levels involved with stimulated Raman scattering 15
2.9 Stimulated Raman scattering in MeCN . . . . . 15
2.10 White light continuum . . . . . 19
2.11 Comparison of generated white light . . . . . 20
2.12 Spectrometer layout . . . . . 21
2.13 Comparison of chirp in reflective and transmissive setup . . . . . 22
2.14 Reduction of cross phase modulation . . . . . 23
2.15 Minimization of stimulated Raman amplification . . . . . 23
2.16 Data analysis flow chart . . . . . 25
2.17 Convolution affect on signal peak . . . . . 26
2.18 Effect of chirp correction . . . . . 27
2.19 Linear chirp across transient absorption surface . . . . . 28
2.20 Gradient of the absorption spectra of filters for wavelength calibration 29
2.21 Example of spectral slices, azobenzene . . . . . 30
2.22 Example of an overlaid spectral comparison using F1 and azobenzene 31
2.23 Example of kinetic traces using oxazine . . . . . 32
2.24 Example of overlaid kinetic comparison for oxazine in MeCN and Hexane . . . . . 33
2.25 Global fitting results for oxazine showing the decay associated spectra and species associated spectra . . . . . 37

3.1 Isomerization of azobenzene . . . . . 38
3.2 Azobenzene absorption spectra . . . . . 39
3.3 Azobenzene isomerization mechanisms . . . . . 41

3.4 Effect of excitation on azobenzene absorption spectra . . . . . 43
3.5 Comparison of azobenzene transient absorption spectral slices to literature . . . . . 44
3.6 Transient absorption surface of azobenzene in MeCN . . . . . 45
3.7 Azobenzene isomerization energy surface . . . . . 46
3.8 Transient absorption signal arising due to thermalization . . . . . 46
3.9 Trasnsient absorption surface of azobenzene in THF . . . . . 47
3.10 Azobenzne spectral slices in MeCN and THF . . . . . 48

4.1 Foldamer chlorine capture mechanism . . . . . 50
4.2 Foldamer family . . . . . 51
4.3 Foldamer chloride ion conductivity . . . . . 52
4.4 Binding constants across foldamer family . . . . . 53
4.5 NMR titration of chloride addition to foldamer . . . . . 54
4.6 Transient absorption surface of F1 . . . . . 55
4.7 Azobenzene and F1 transient absorption surfaces . . . . . 56
4.8 F1 and azobenzene spectral slices . . . . . 57
4.9 Decay associated spectra of F1 and azobenzene in MeCN . . . . . 58
4.10 F1 and F1H spectral slices . . . . . 59
4.11 Decay associated spectra of F1 and F1H in MeCN . . . . . 60
4.12 Foldamer illustrative potential energy surface . . . . . 61
4.13 F1 and F2 spectral slices . . . . . 61
4.14 Decay associated spectra of F1 and F2 in MeCN . . . . . 62
4.15 F2 and F2H spectral slices . . . . . 63
4.16 Decay associated spectra of F2 and F2H in MeCN . . . . . 63
4.17 Decay associated spectra for the foldamer family . . . . . 64
4.18 Spectral slices of F1 in both MeCN and THF . . . . . 65
4.19 Spectral slices of F2 in; MeCN, THF, and 1:1 mixture of both . . . . 66
4.20 Comparison of the F2 and F2H surface collected in THF . . . . . 67
4.21 Spectral slices of F1 with and without chloride . . . . . 68
4.22 Spectral slices of F2 with and without chloride . . . . . 68

5.1 Oxazine isomerization pathway . . . . . 71
5.2 Absorption spectra of oxazine . . . . . 71
5.3 Chemical structure of oxazine and derivatives. . . . . 72
5.4 Transient absorption surface of oxazine . . . . . 73
5.5 Transient absorption surface of fluorinated indole . . . . . 74
5.6 Global fitted species spectra of oxazine . . . . . 75
5.7 Nanosecond decay of oxazine . . . . . 75
5.8 Oxazine ring opening steps . . . . . 76
5.9 Polarization dependance of oxazine transient absorption signals . . . 77

5.10 Anisotropy of oxazine . . . . . 78
5.11 Various decay behaviors observed for oxazine . . . . . 80
5.12 Normalized spectral slices of fluorinated oxazine . . . . . 81
5.13 Fluorinated oxazine in different solvents . . . . . 82
5.14 Proposed ring opening mechanism . . . . . 83

# List of Tables

3.1 Lifetimes for azobenzene in MeCN and THF . . . . . 48

4.1 Fitted lifetimes for F1 and azobenzene . . . . . 57
4.2 Foldamer lifetimes associated with decay steps . . . . . 65
4.3 Comparison of F1 and F1H lifetimes . . . . . 66

5.1 Fitted rates for OX and OXF and the corresponding models assignment 83

# List of abbreviations

| | |
|---|---|
| AB | Azobenzene |
| Abs. | Absorption |
| DAS | Decay associated spectrum |
| F1 | Foldamer 1 |
| F1H | Half foldamer 1 |
| F2 | Foldamer 2 |
| F2H | Half foldamer 2 |
| GSA | Ground state absorption |
| GSB | Ground state bleach |
| IRF | Instrument response function |
| MeCN | Acetonitrile |
| Norm. | Normalized |
| OD | Optical density |
| OPA | Optical parametric amplification |
| OX | Oxazine |
| OXF | Fluorinated oxazine |
| PES | Potential energy surface |
| PIA | Photo–induced absorption |
| SAS | Species associated spectra |
| SE | Stimulated emission |
| SFG | Sum frequency generation |
| SRA | Stimulated Raman amplification |
| SVD | Single value decomposition |
| TA | Transient absorption spectroscopy |
| THF | Tetrahydrofuran |
| TPA | Two photon absorption |
| UV | Ultra–violet |
| Vib. | Vibrational |
| WLG | White light generation |
| XPM | Cross phase modulation |

# Chapter 1

# Outline

Numerous photo–isomerizing molecules have been developed, which take advantage of isomerization around a double bond, as with azobenzene, or a photo–induced bond breakage, as in oxazine. The light control achieved by these molecules has had their design tailored towards a number of applications. These include molecular motors, which rely on the isomerization and steric bulk of alkenes.[1] Expanding on this generation of motion there are also molecular shuttles,[2] and muscles.[3] The photo–active moieties have also been incorporated in molecules designed for drug delivery, this allows for targeted delivery based on external stimuli.[4] Another use is by incorporation into a mono–layer, here it is able to change the surface expressed groups, allowing for controlled adhesion.[5] Their inclusion at the surface has been used to manipulate self assembly,[6,7] and act as a microfluidic pump.[8,9] This photo–induced isomerization is also found in biology, whereby it is a key process involved in vision. The rhodopsin protein contains carbon–carbon double bonds that undergoes isomerization on exposure to light, starting a series of reactions concluding in electron signals being sent to the brain.[10]

This work focuses on using transient absorption (TA) spectroscopy to study the photophysics of two photo–active compounds; a family of light–controlled chloride ion capture and release foldamers developed and synthesized by Dr. Amar Flood and co–workers, and oxazine synthesized by Dr. Brendan Burkett and co–workers. **??** shows the two structural change involved in the isomerizations; Top has foldamer, middle azobenzene (involved with foldamer), and bottom oxazine. For the foldamer (top) capture and release of chloride ion (green) is induced by changing between a helix and random coil conformation. For this to occur the photo–active moiety azobenzene (blue) is irradiation with visible light to give the *cis* azobenzene and random coil foldamer conformation, while ultra–violet irradiation results in *trans*

azobenzene and helix foldamer conformation. Oxazine (bottom) undergoes carbon–oxygen bond cleavage on irradiation of ultra–violet light, this results in the formation of a nitrophenolate moiety (red) which is a chromophore that absorbs in the visible (~440 nm). Unlike the foldamer family relaxation to the pre–photoexcitation state is not photo–active, but happens thermally on the nanosecond timescale. These molecules present challenges in gathering transient absorption spectra; they require an ultra–violet excitation pulse and a probe pulse that reaches into ultra–violet wavelengths. This necessitates changes to the existing TA setup in this laboratory, as well as collection and processing of transient absorption data, which will be covered in the following discussion.

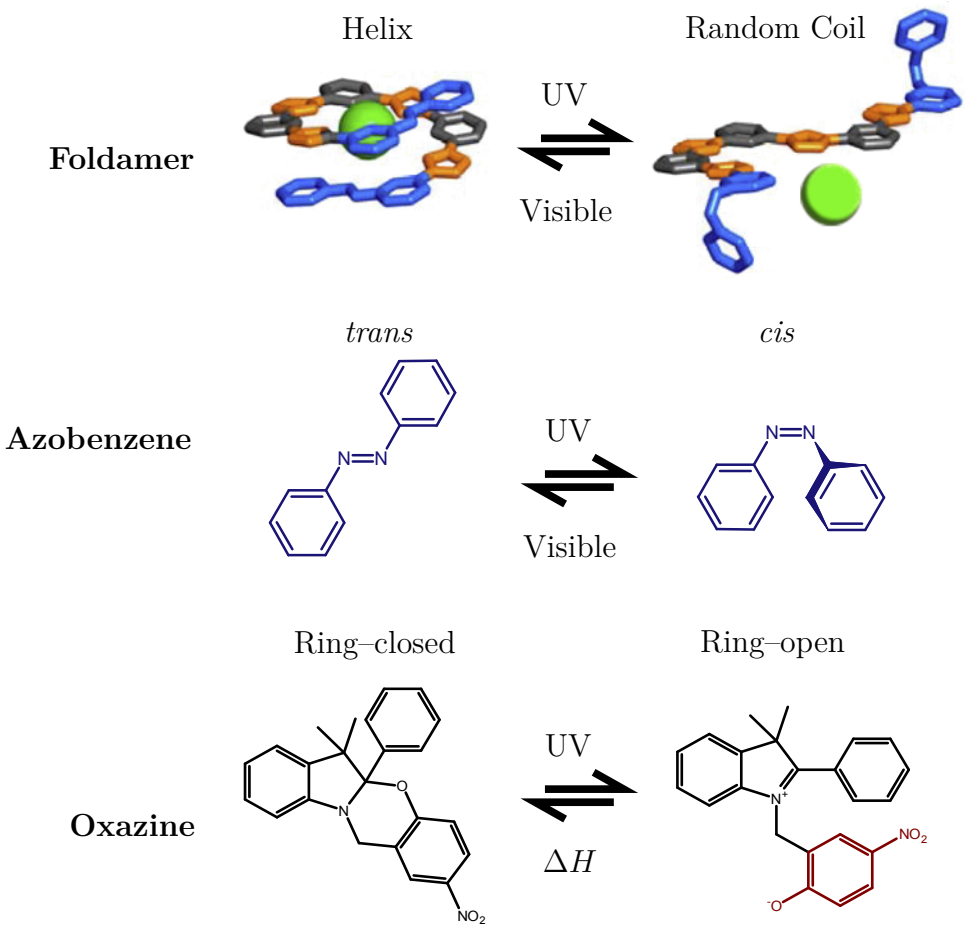


**Figure 1.1** The three molecule being studied by this work. The top has the foldamer isomerizing between a random coil and helix conformation when irradiated with ultra–violet (UV) or visible (visible) light respectively. The photo–active moiety responsible for this change is azobenzene shown in the middle. It undergoes isomerization to *cis* with UV and *trans* with visible excitation. The bottom shows oxazine undergoing carbon–oxygen bond breakage to produce the nitrophenolate chromophore (red), bond formation happens thermally.

In order to use TA spectroscopy an understanding of the setup and operation is needed. This work will provide an overview of how non–linear optical effects are exploited using femtosecond laser pulses for TA spectroscopy.[11] The effects covered

include frequency doubling, optical parametric amplification, difference frequency generation, sum frequency generation, and white light generation. The changes made to facilitate the capture of transient absorption data that spans into the ultra–violet, generation of ultra–violet pump pulse, and data processing routines implemented for this work will be highlighted.

Azobenzene will be examined first, as it is responsible for the photo–isomerization of the foldamer.[12] This will provide a reference for the setup and calibration of the TA spectrometer, as there are literature spectra available for comparison.[13–17] It will also allow the effects of solvents and introduction of chloride ions to be observed and compared with what occurs in the foldamer. Once the TA experimental setup has been benchmarked, and solvent changes expected in azobenzene have been covered, insights into the photophysics of the foldamer family and oxazine will be discussed.

# Chapter 2

# Transient Absorption Spectroscopy

Understanding the dynamics of molecular excited states is of great importance to any photophysical process. One of the main experimental tools used for this is transient absorption (TA) spectroscopy. It regularly achieves time resolution on the hundreds femtosecond time scale, with spectral intensity changes on the order of $10^{-6}$ being routinely measurable.[11]

This chapter underlines the theory behind TA, including the key aspects and processes involved in a working TA setup. A detailed description of the TA signal, and how this can be related to photophysical processes will be discussed. This includes both theoretical underpinnings and implementation of more realistic models. Particular emphasis will be given to areas that have been implemented during this work, these include; extension of the detection range into the UV spectral, artifact minimization, and the implementation of data analysis and post–processing routines.

## 2.1 Theory of Transient Absorption Spectroscopy

TA spectroscopy relies on the use of two ultra–short laser pulses to generate spectral and temporal data from a chemical system.[18] The two pulses are known as the pump and probe. The pump pulse is used to generate the excited species, and the probe pulse is used to investigate electron transition in the same manner to absorption spectroscopy.[19] Figure 2.1 gives an overview of the instrumental layout, illustrating the pump and probe pulses, and including other key components such as the

electronically controlled mechanical delay stage and spectrometer. The mechanical delay stage adjusts the timing between the pump and probe pulses, this is done by lengthening or shortening the light path of the pump pulse. The spectrometer collects the spectral changes in the probe pulse, which is done by comparing the difference in spectra with and without the pump pulse present.

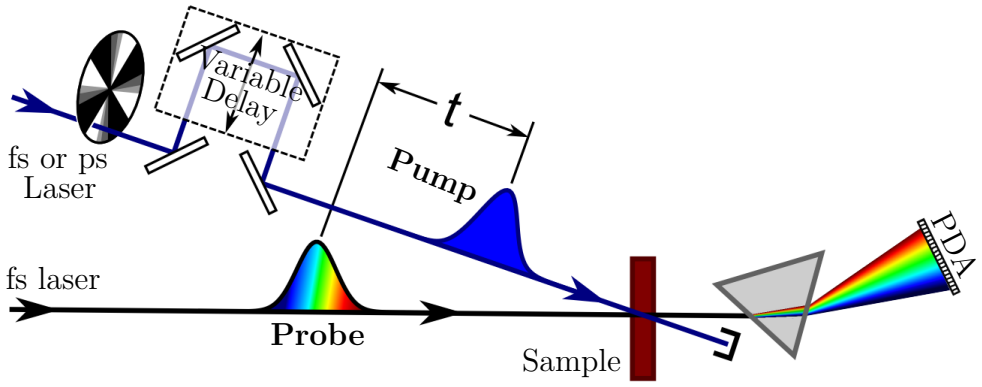


**Figure 2.1** Layout for a transient absorption system. The pump and probe pulse overlap at the sample with the probe pulse being resolved by the prism spectrometer. The time delay between the pump and probe pulses are controlled using the variable delay line. PDA stands for photodiode array,

Section 2.2 contains details on how the probe and pump pulses are generated, this section focuses on the underlying principles of data acquisition, relating the photophysical process to observed signal, and common artifacts encountered.

### 2.1.1 Data Acquisition

TA data can be broken down into three components; time, wavelength and intensity.[19–21] The spectrometer collects the wavelength component, and intensity. The delay stage is used to generate the temporal element, giving the three pieces of information needed for each data point.

The excited state spectra is determined by comparison of the absorption of the sample with and without the influence of the pump pulse. In this manner absorption by molecules in their ground state can be isolating from absorption induced by molecules in an excited state.[11,18,19,22,23] The change in optical density ($\Delta$OD) is calculated by Equation 2.1, the difference between absorption after excitation ($A_{ex}$) and ground state absorption ($A_{gs}$). $\Delta$OD is the logarithm of the ratio of probe pulse intensity with ($I_{on}$) and without ($I_{off}$) the pump pulse present. $I_0$ is the reference intensity and is not strictly needed to determine the transient signal. The wavelength range is determined by the broad spectral band probe pulse, with a spectral range

from 300 nm to the IR being possible[24] (discussed in section 2.2.2). The spectral sensitivity is determined by the shot–to–shot stability of the probe pulse.

$$\begin{aligned} \Delta OD(\lambda, t) &= A_{ex}(\lambda, t) - A_{gs}(\lambda) \\ &= -log\frac{I_{on}(\lambda, t)}{I_0(\lambda)} + log\frac{I_{off}(\lambda)}{I_0(\lambda)} \\ &= -log\frac{I_{on}(\lambda, t)}{I_{off}(\lambda)} \end{aligned} \tag{2.1}$$

Temporal resolution is achieved by delaying the pump pulse relative to the probe pulse, in this manner the sample is probed at a variable interval after pumping.[11,18,19,22,23] This allows the collection instruments to operate on a much slower timescale than the minimum time step, as the temporal resolution is determined by the delay between the laser pulses. A computer–controlled mechanical delay stage is used to control the delay between pump ($t_{pump}$) and probe ($t_{probe}$) pulses. This adjusts the pathlength along which the pump pulse travels by moving a pair of mirrors that are at right angles to each other. The right angle configuration is necessary so that the pump pulse heading into and out of the delay arm are parallel so there is no deviation in the pump pulse path at different pathlengths. A change in path length gives a change in pump–probe delay defined by Equation 2.2, with a 1 $\mu$m adjustment giving a 3 fs change in delay time. This change relates directly to the time point, with time–zero set to when the pump and probe pulses arrive at the same time.

$$\begin{aligned} \Delta t &= t_{pump} - t_{probe} \\ &= \frac{l_{pump}}{c} - \frac{l_{probe}}{c} \\ &= \frac{1}{c}(l_{pump} - l_{probe}) \end{aligned} \tag{2.2}$$

**Spectra**

The overall photophysical process can be broken down into discrete states or intermediates, many of which contribute to the TA signal.[20,22] Understanding the roles of these signals is imperative to elucidate the photophysics of the molecule. The signal can be broken down into three general categories (Figure 2.2); ground state bleach (GSB), photo–induced absorption (PIA), and stimulated emission (SE). The

broad nature of TA signals means that overlap of multiple signals results in spectra that are the sum of many different underlying features.[21] Separating the underlying components can be achieved by a combination of steady–state measurements of both ground state and model compounds, and modeling the kinetic data.[20,21]

GSB is a negative signal it has the same shape as the ground state absorption spectrum. This occurs due to the decrease in the population of the ground state as a result of excitation by the pump pulse.[21] As there is now a lower concentration of ground state species, absorption decreases.

Like GSB, SE is a negative signal, it arises from the interaction of the probe pulse with the excited molecules.[21] The probe pulse contains wavelengths that correspond to the energy of transitions to the ground state, interactions between the sample and probe pulse result in the release of a photon, known as stimulated emission. The increase in photons gives the same result as a decrease in absorption, as a higher intensity of photons are detected. The shape of the signal is related to the ground state fluorescence spectrum, as this emission occurs from a similar place in the electron energy manifold.

Unlike the other signals, PIA is a positive signal, it comes from the absorption of excited state species.[21] This absorption is from the excited state into higher excited states, and can occur from a singlet state to higher singlet states, or if the molecule has relaxed to a triplet state, higher triplet states may become populated.

### Kinetics

The Jablonski diagram in Figure 2.3 shows the relaxation pathways available afters excitation. If a higher excited state is considered there are a number of reaction pathways possible; these include vibrational relaxation, internal conversion, inter–system crossing, and external conversion.[19,25] The transfer between these states is time dependent with many of the states being observable by a TA signal, with there decays (kinetics) and spectra being resolved.

All of these can occur but the probability of each is different, with the dependence related to the orbital overlap integral. This comprises contribution from electron, spin, nuclear states, and an operator dependent on the method of transition. A higher orbital overlap integral makes the transition between the states more likely leading to greater rate of transfer. This leads to a variation in the PIA over time as the excited state returns to the ground state. Depending on the time after excitation

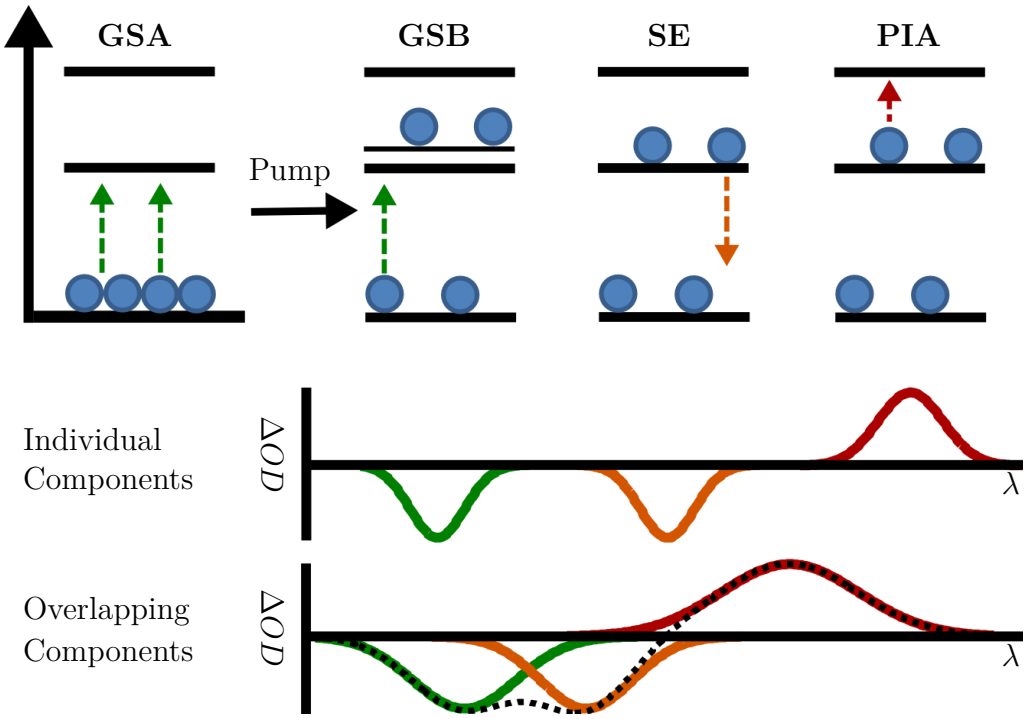


**Figure 2.2** The electronic transitions responsible for each TA signal, with the corresponding sign of the signal displayed on the axis below. Absorption is labeled ground state absorption (GSA) and the TA signals are; ground state bleach (GSB), stimulated emission (SE), and photo–induced absorption (PIA). The overall signal comprising of the three possible signals when they are overlapping is dotted in black.

the transient absorption spectra will differ.[19,21] Shortly after excitation vibrational effects dominate, and depending on the molecule there may be crossing into the triplet manifold, or to other intermediate singlet states.[15,17,26] From each of these states the absorption will differ and so result in peaks in the TA surface.

The changes of these peaks can be tracked over time to give kinetic profiles of the decays from one state to another. Figure 2.4 shows a simplified example of the transfer from one state to another and the resulting effect on spectra. This can become more complicated due to the broad nature of peaks resulting in their overlap. There can also be a number of processes possible that need to be separated from each other.

### 2.1.2 Experimental Artifacts

The signal collected by TA contains a number of artifacts. The reasons for these artifacts have been discussed in a number of publications.[19–21,27–29] These arise near time equals zero and can have a large influence on the apparent dynamics on timescales less than 1 ps. This timescale is important for photo–isomerization with the initial

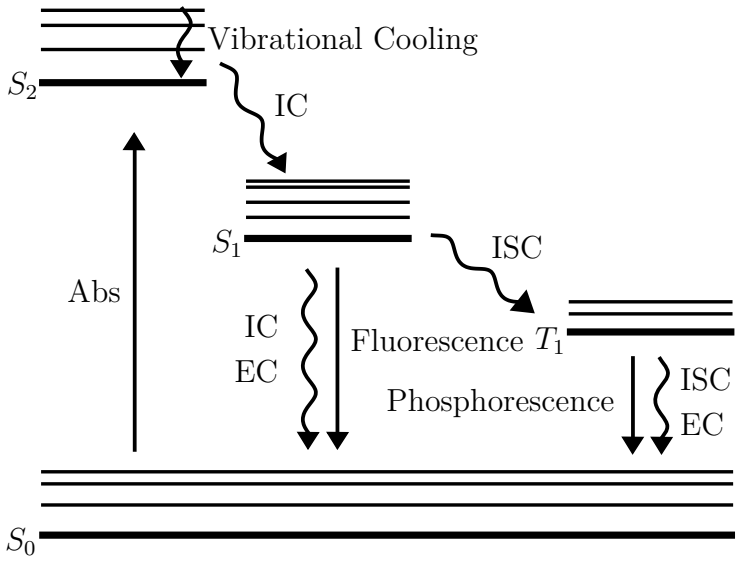


**Figure 2.3** The possible pathways back to the ground state are shown, they include; internal conversion (IC), vibrational cooling, inter–system crossing (ISC), external conversion (EC), and fluorescence.[22] The number of pathways highlights the need for temporal resolution to help identify the appropriate decay pathway.

bond–breakage or rotation occurring on these timescales.[26]

The main artifacts covered are below, and include; instrument response function (IRF), chirp, two photon absorption (TPA), cross phase modulation (XPM), and stimulated Raman amplification (SRA). To set up a useful system care must be taken to minimize these artifacts. Procedures introduced into the experimental setup are detailed in Section 2.2. Additional post processing can be used in most cases to deconvolute the underlying kinetics from the artifacts (Section 2.3).

### Instrument Response Function

IRF defines the minimum temporal resolution achievable,[11] because the temporal width of the pump and probe pulses is longer than the time delay achievable by adjusting the pump–probe pathlength.[20,21] It is also for this reason they cannot be thought of as instantaneous pulses. Upon excitation there is a distribution of excitation time, some molecules are excited by the leading and others the trailing edge of the pump pulse. Due to this, the underlying decay becomes convoluted by the temporal intensity profile of the pump pulse, which is considered to be Gaussian shaped (Figure 2.5).[20,21]

The signal intensity is given by the integral of the overlap of decay and pump pulse's temporal profiles. This intensity is ascribed to a time delay that corresponds to the

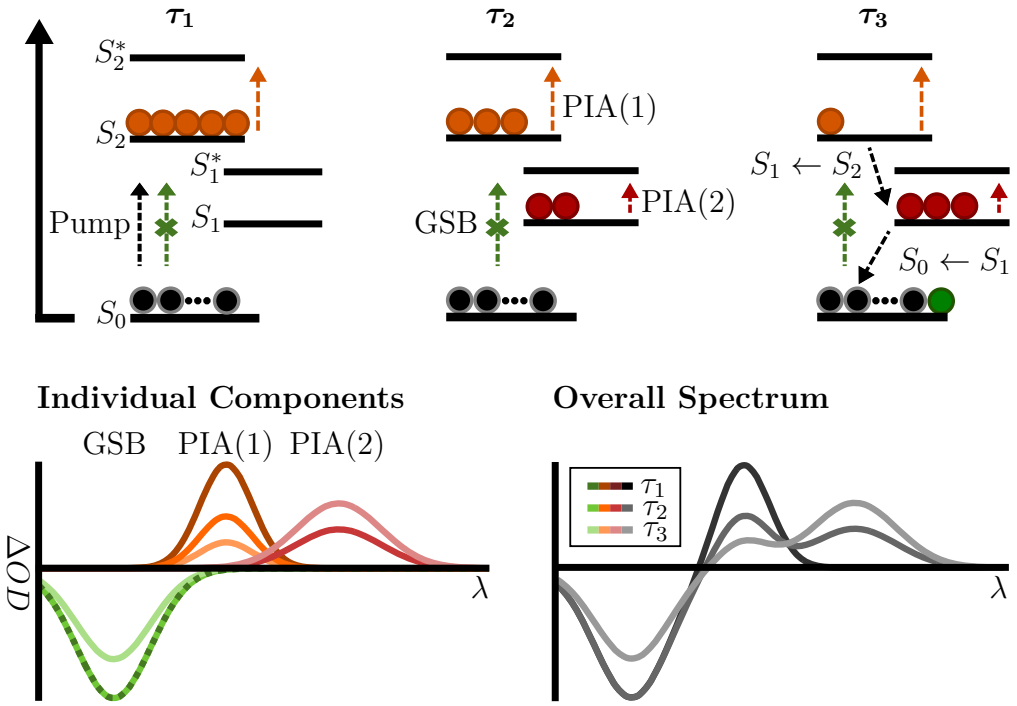


**Figure 2.4** Diagram showing how each component effects the TA, signal and how changes in each population leads to a time–dependant signal. $T_1 to T_3$ are sequential times

center of the pump pulse's profile. If the temporal width is of similar magnitude to the timescales being studied this convolution of the underlying decay becomes important. When the decay is encompassed within the pump pulse's temporal profile, any changes in decay result to minimal change to the signal intensity. This is because the decay can still be wholly encompassed by the pulse width. As the pulse width is broader than the resolution achievable by changes in pathlength, the IRF is the limiting factor of the temporal resolution.[11,20]

### Chirp

Chirp is the term used to describe the temporal offset of wavelengths within a broad spectral band pulse. This arises from the wavelength dependence of the refractive index of a transparent media, with higher energy (longer wavelength) photons associated with a higher refractive index.[11,21] This results in shorter wavelengths arriving later than longer wavelengths giving a observable effect in broad the spectrum TA signal. This can be seen in Figure 2.6, showing the onset of signal varying with wavelength. The arrival of the probe pulse before the pump pulse is indicated by the green section. With the rise of PIA seen as the transition from green to red. There is a slight dip before the signal onset (blue), this is indicative of XPM.

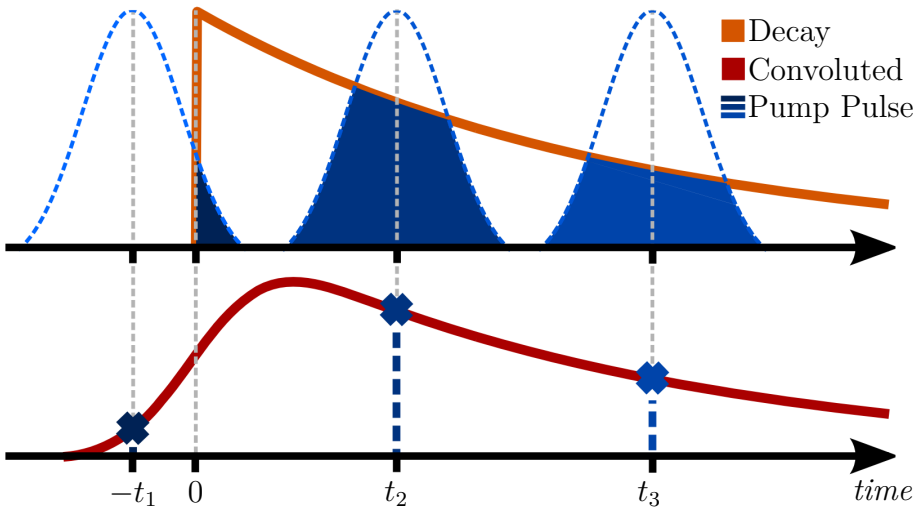


**Figure 2.5** The early time signal is a convolution of the Gaussian pump pulse profile with the underlying signal dynamics. Blue Gaussian are pump pulses at different times. The intensity of the convoluted signal at the corresponding time is given by the integral of the overlap of decay and pump pulse.

The offset of time equal zero across the wavelength range affects the kinetic traces, with a larger impact on shorter lifetime signals. The offset affects the interpretation of the kinetic traces, as the onset of each wavelength appears later, the longer the wavelength. This could appear to be a decay from a low wavelength into a higher wavelength. The importance of chirp on the signal is related to the lifetime. A nanosecond decay will have a longer signal where the picoseconds of chirp have a negligible effect, while a picosecond decay will have significant decay occurring before the signal appears at longer wavelengths. Chirp correction is covered in Section 2.3.1.

### Two photon absorption

If a medium is transparent for particular wavelengths at low radiation intensities it is not always the case that this is true for high radiation intensities. This is due to simultaneous absorption of two photons with a combined energy that is in the absorption band of the solvent. One photon can be from the high energy pump pulse, and the second from the probe pulse. This leads to a broad absorption of probe pulse wavelengths when the pump and probe pulses are incident on the sample.[28] This only occurs at time equal zero, with absorption of the probe pulse adding a positive signal to the TA surface.

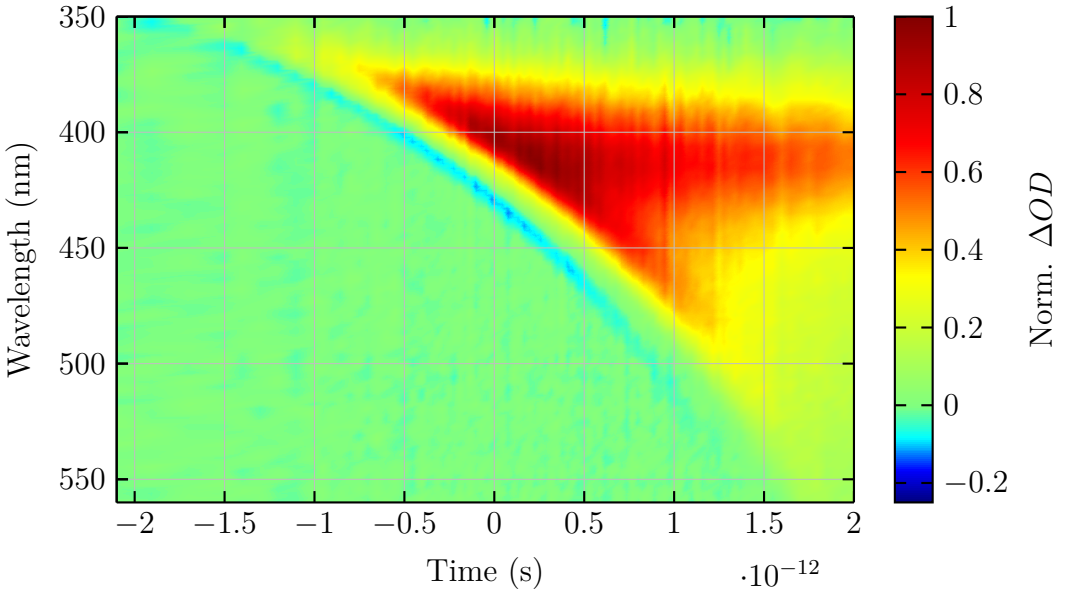


**Figure 2.6** Signal onset with chirp present, 1 $\mu M$ foldamer (F1) with 300 nm excitation.

### Cross phase modulation

The cross phase modulation (XPM) artifact appears in the spectrum only when the pump and probe pulses overlap temporally and spatially at the sample. The high instantaneous power of the pump pulse modulates the refractive index of any transparent medium it travels through. This modulation affects the probe pulse if there is both spatial and temporal overlap with the pump pulse, leading to an artifact over the temporal width of the pump pulse.[28]

The time dependence of the signal can be seen in Figure 2.7. It consists of negative wings with a positive peak at time zero. The shape is determined by the mismatched travel time of the pump and probe pulses through the transparent medium ($\tau_{GVD}$), with a larger mismatch leading to greater separation between the two peaks.

The intensity increases at lower wavelength, higher pump pulse intensity, large pump–probe overlap, and greater probe pulse chirp. The pump pulse intensity affects the degree of refractive index modulation. The pump–probe overlap affects the period that the probe pulse is affected. Increasing either leads to higher intensity XPM. Chirp dependence changes the number of frequencies that interact with the pump pulse at any one time, a smaller number leading the higher XPM.[28] A more rigorous mathematical treatment of XPM can be found in the literature.[30,31]

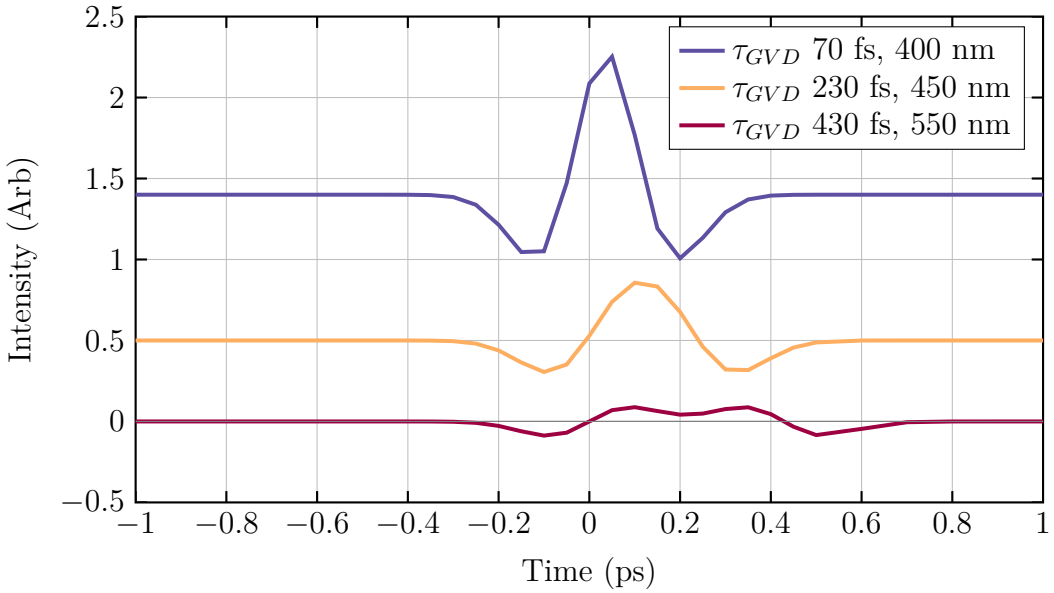


**Figure 2.7** Offset plot of XPM signal simulated using literature equations, pump pulse full width half maximum (FWHM) is 180 fs. Intensity variations are caused by change in wavelength, while the splitting of two peaks is a result difference in time taken for pump and probe pulses to pass through sample ($\tau_{GVD}$).

### Stimulated Raman Amplification

Stimulated Raman amplification (SRA) arises when the probe pulse contains wavelengths that are shifted from the pump pulse an amount comparable to vibrational transitions. Stimulated Raman amplification is a non–linear process, and is dependent on the materials third order non–linear susceptibility $\chi^3$. This is due to the involvement of three photons; pump pulse, probe pulse and that stimulated to give amplification.[28] Here a conceptual view is presented, a more rigorous mathematical description can be found in the literature.[30]

If two incident photons are considered, $h\nu_1$ is the higher energy seed for the Raman virtual energy level, while $h\nu_2$ is the lower energy stimulating photon (Figure 2.8). Excitation to the virtual Raman level by $h\nu_1$ and stimulated emission to a vibrational excited ground state by $h\nu_2$. Resulting in an increase of photon flux at Stokes shifted (lower energy) wavelengths from the pump pulse, giving Raman gain. Considering the pump pulse as $h\nu_2$, Raman loss occurs at anti–Stokes shifted (higher energy) wavelengths. Probe pulse light is absorbed to the virtual Raman level, to be driven to vibrationally excited ground states by the probe pulse.[28]

This requires both the pump and probe pulses to be coincident at the same time and place leading to an effect that is confined to the temporal width of the probe pulse. Figure 2.9 illustrates both the Stokes longer wavelength gain, and anti–Stokes shorter

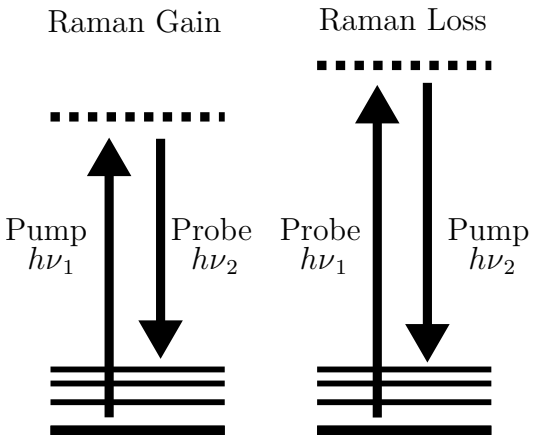


**Figure 2.8** Virtual and Vibronic levels involved with Stimulated Raman amplification. The combination of two photons; the Raman seed ($h\nu_1$) and stimulating photon ($h\nu_2$). The source of each photon is important to whether Raman gain or Raman loss is observed. If the seed is the pump pulse, Raman gain occurs, and with seed as the probe pulse, Raman loss occurs.

wavelength loss seen in a TA spectrum. Wavelength is converted to wavenumber by first taking the difference from the pump pulse wavelength, and then converting units from nanometers to wavenumber. This results in a vibrational spectra with loss and gain peaks (Figure 2.9). These peaks are broader than typical vibrational spectrum due to the lower wavelength resolution. The three main peaks are at 2960 $cm^{-1}$, 2250 $cm^{-1}$, and 1410 $cm^{-1}$, these match well with expected vibrational peaks for the solvent (acetonitrile), 2942 $cm^{-1}$, 2248 $cm^{-1}$, and 1414 $cm^{-1}$.[32]

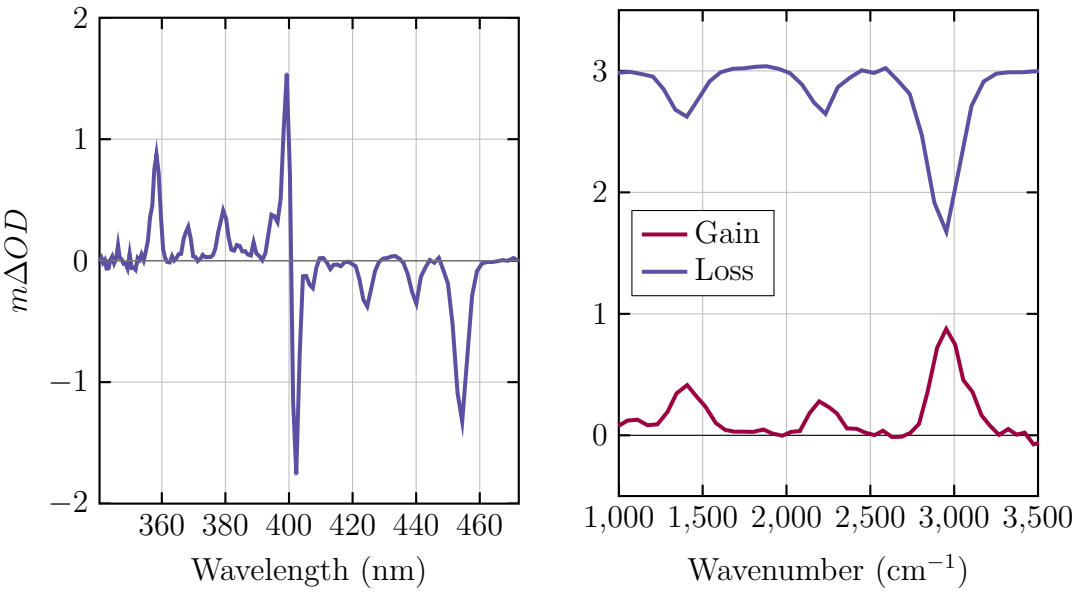


**Figure 2.9** Stimulated Raman trace from -100 to 100 fs, collected in MeCN with 400 nm pump pulse. TA signal has been minimized by subtracting the signal from a later time.

## 2.2 Transient Absorption Setup

In order to collect broad spectral band femtosecond TA spectra, a high power ultra–fast laser is used.[19,33] This is done by mode–locking to generate the ultra–short pulses, and the amplification to increase pulse power.[11] The pulse is split into two paths, one for the pump pulses and the other for the probe pulses. These two pulses undergo a number of non–linear optical processes to achieve the desired characteristics for each. The pump pulse is a spectrally tunable narrow band pulse,[34] while the probe pulse is spectrally broad[35,36] . The final step is the recording of the spectral distribution of the broad spectral band probe pulse.

### 2.2.1 Non–Linear Optics

In generating the pump and probe pulses, a number of non-linear optic effects are taken advantage of to convert the intense and ulta–short 800 nm pulses into tunable and broad pulses in spectroscopically useful wavelength regions. These arise from the intense electromagnetic fields generated when a pulse is on the femtosecond timescale.[33] They are generated because instantaneous power is great enough to breaks down the linear approximations made when consider the polarizability of light traveling through matter.[33]

Equation 2.3 can be used to model the interaction of the electromagnetic field $\widetilde{E}(t)$, and its effect on the polarization of a material $\widetilde{P}(t)$. This contains the higher order terms $\chi^2, \chi^3 \cdots$ which are the second, third, etc, order non–linear optical susceptibilities respectively.[33] These are dependent on the material being used. Crystals like $\beta$–barium borate (BBO) have large $\chi^2$ values, making them useful to harness non–linear optical affects. These terms can be related to the second and third order non–linear polarization; as shown in Equation 2.4.[33]

$$\widetilde{P}(t) = \epsilon_0(\chi^1\widetilde{E}(t)^1 + \chi^2\widetilde{E}(t)^2 + \chi^(3))\widetilde{E}(t)3 + \cdots) \tag{2.3}$$

$$\begin{aligned} \widetilde{P}(t)^2 &= \epsilon_0\chi^2\widetilde{E}(t)^2 \\ \widetilde{P}(t)^3 &= \epsilon_0\chi^3\widetilde{E}(t)^3 \end{aligned} \tag{2.4}$$

The second order effects are used for optical parametric amplification (OPA) and frequency doubling, while white light generation (WLG) is a more complex pro-

cess. Both will be covered briefly here, with more in depth coverage found in the literature.[33]

### Narrow Band Pump Pulse

Generation of an intense narrow band pump pulse of selectable wavelength is done by taking advantage of second order non–linear optical effects. These include interaction of one wavelength of light with a transparent medium to give second harmonic generation or that of two distinct frequencies, which gives sum frequency generation (SFG), or optical parametric amplification (OPA).

To select which process, SFG or OPA, occurs in a non–linearly active crystal the phase matching angle is adjusted. This is because the crystals chosen for second order process have an anisotropic refractive index. The angle of the crystal can be set such that the generated light pulse and incident pulse are in phase throughout the crystal, minimizing any destructive interference and favoring this desired process.[33,37,38] The simplest example of this is second harmonic generation, producing photons of twice the frequency. Considering an electric field with a single wavelength $\omega$, the electric field can be modeled using Equation 2.5.[33] The second–order polarization interaction can be seen in Equation 2.6 doubling the frequency from $\omega$ to $2\omega$, highlighted in red.

$$\widetilde{E}(t) = E(t)e^{-i\omega t} + E(t)e^{i\omega t} \tag{2.5}$$

$$\begin{aligned} \widetilde{P}(t)^2 &= \epsilon_0\chi^2(E(t)e^{-i\omega t} + E(t)e^{i\omega t})^2 \\ &= \epsilon_0\chi^2(E^2(t)e^{-i2\omega t} + E^2(t)e^{i2\omega t} - 2E^2) \end{aligned} \tag{2.6}$$

Similar interactions are seen for two frequency processes ($\omega_1 > \omega_2$), SFG gives $\omega_{new} = \omega_1 + \omega_2$, and OPA $\omega_{new} = \omega_1 - \omega_2$ with an amplification of $\omega_2$ as the energy from $\omega_1$ is used to produce both $\omega_2$ and $\omega_{new}$. These processes are summarized by Equation 2.7.

$$\begin{aligned} \omega_1 + \omega_2 &\rightarrow \omega_{new} & \omega_{new} &= (\omega_1 + \omega_2)\ \text{(SFG)} \\ \omega_1 + \omega_2 &\rightarrow \omega_{new} + 2\omega_2 & \omega_{new} &= (\omega_1 - \omega_2)\ \text{(OPA)} \end{aligned} \tag{2.7}$$

#### Broad Spectral Band Probe Pulse (White Light Generation)

WLG occurs when intense ultra–short laser pulse are focused onto a transparent media, this effect has been observed in gases, liquid, and solids.[24,36,39,40] The WLG process is initiated by self–phase modulation and the self–focusing associated with the pulse within the medium.[39,41] This is due to the effect that third order non–linear electronic fields have on the refractive index, leading to a self–focusing effect. This highly focused pulse has a number of other effects including; self–steeping, four–wave mixing, and ionization contributing to the overall WLG.[39,41,42] Further details can be found in the comprehensive review by Couairon and Mysyrowicz.[39]

### 2.2.2 Layout Enhancements

The layout of the existing setup needs to be modified for two reasons; first there is a need for a high power UV probe pulse, this is necessitated by the low absorption coefficient of azobenzene (<25000 $M^{-1}cm^{-1}$), and the absorption transition of interest being in the UV spectral region (>360 nm).[16] This requires changes to the pump pulse path to increase pump pulse power at the sample. Secondly, the major absorption band is in the UV region and makes probing this region highly valuable. To this end, the probe pulse needs to be adjusted to get light of high enough intensity in this region. By doing this the ground state bleach becomes observable, which provides valuable information for azobenzene (Chapter 3), foldamer (Chapter 4), and oxazine (Chapter 5).

#### Ultra–violet Pump Pulse

To achieve sufficient laser power density at the sample, losses due to lower UV reflection from mirrors need to be minimized. This was achieved using two methods. The pump pulse was generated in the visible spectral region at half the frequency of the required output. This took advantage of the much higher (>97%) reflectivity of standard mirrors for most of the pump pulse path. BBO is used for second–harmonic generation giving the desired excitation wavelength at the sample. After doubling, all standard mirrors were replaced with UV–enhanced versions increasing reflectivity at 320 nm from 88.9% to 92.7%. These changes resulted in an increase of average pump pulse laser power at the sample from 60 $\mu$W to 300 $\mu$W after enhancement.

### Ultra–violet Extension of Probe Pulse

Broad spectral band probe pulses are typically generated in a sapphire medium, this is because of the resistance to damage from the intense laser pulses used, and stability of continuum generated.[11,42] This continuum cuts out at wavelengths shorter than ~470 nm and so $CaF_2$ is required to generate a broad spectral band probe pulse that contains UV wavelengths. $CaF_2$, is not commonly used due to is susceptibility to laser ablation after prolonged exposure.[34,42] This irreversible damage adversely affects the quality of the white light generated. WLG in $CaF_2$ has been shown to span 200 nm into the IR, dependent on the seed pulse, Figure 2.10.[41] A 785 nm seed gives a range of ~310 nm into the IR, this is sufficient to overlaps with the absorption spectra of the target molecules.

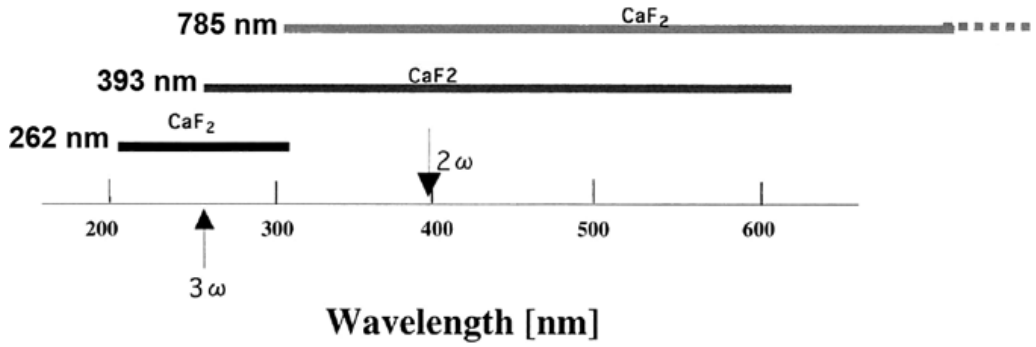


**Figure 2.10** Broad spectral band continuum generated in $CaF_2$ at 262 nm, 393 nm, and 785 nm seed wavelengths.[41]

$CaF_2$ crystal was setup and optimized with a 800 nm seed laser pulse. Optimization involves adjusting the seed laser pulse power, aperture, and focal position, until a stable source of white light is generated. Optimization begins by setting the parameters using values which can can be found in literature, from these an iterative process is used to reach a stable broad spectral band continuum.[11,41,42] To overcome laser ablation $CaF_2$ was mounted on an automated horizontal translation stage moving at millimeters per second. Translation was chosen instead of spinning to avoided fluctuations in both the polarization and intensity that have been associated with rotation of the crystal.[34] The spectral and intensity profile of the white light continuum generated can be seen in Figure 2.11, this shows a range from 310 nm to 600 nm. Any light generated around 800 nm is saturated by residual light from the 800 nm seed used for generation, making the usable range between 310 nm and 760 nm.

### Prism Spectrometer

To maximize the throughput of UV light a prism–based spectrometer was built for white light collection. A prism–based spectrometer is able to overcome the low UV throughput of the grating–based spectrometer previously used.[11] Figure 2.11 shows the collected white light, before and after the change to a prism–based spectrometer. There is a noticeable increase in throughput with wavelengths down to 310 nm being detected. The much higher intensity at longer wavelengths is due to the nature of how a prism disperses light, dispersion is closer to being linear in energy than wavelength.[11] This results in a higher photon flux per pixel as the pixel wavelengths get longer, because there is a larger range of wavelengths captured in each pixel. This effect, and the higher intensity of white light continuum at longer wavelengths, leads to a large increase in intensity from shorter to longer wavelengths.

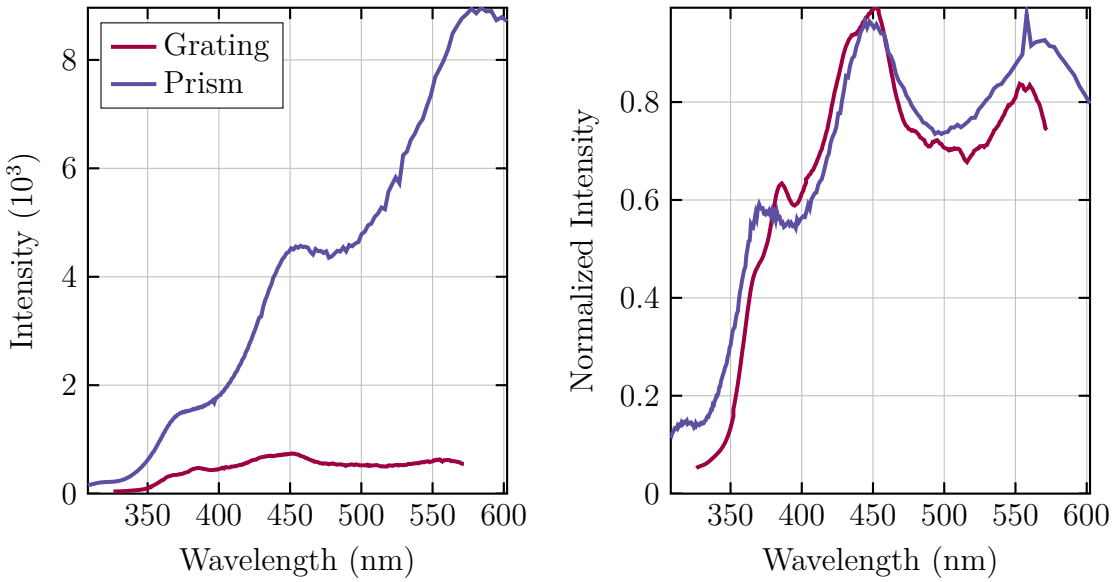


**Figure 2.11** Left, increase in intensity at each pixel. Right, improved spectral range shown on a normalized plot.

A prism is able to separate light due to the refractive index dependance on wavelength, details are discussed in Section 2.3.2. The layout, shown in Figure 2.12, consists of; a prism, mirrors, concave focusing mirrors, and photo–diode array. The choice for each depends on the desired wavelength range and photo–diode array specifications. Quartz is chosen as the prism material as it is transparent in the UV. The choice of the second concave mirror (CM2) depends on the required wavelength range and horizontal length of pixels on the detector. The geometry has to be such that the distance between the CM2 and the prism is equal to the distance between CM2 and the detector making the focal plane of the spectrum lie on the detector pixels.[11] For this setup a CM2 was chosen with f = 200 mm for 12.5 mm length rectangle of pixels, this gave a window from 310 nm to 760 nm.

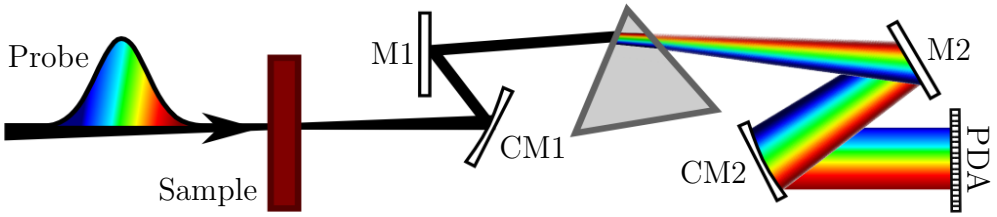


**Figure 2.12** Layout of the prism based spectrometer used for white light collection. M1 and M2 are flat mirrors while CM1 and CM2 are concave mirrors. PDA stands for photodiode array

### Artifacts Minimization

In order to minimize the effects artifacts have on early time signal it is important to carefully consider why they appear. It can be seen that they are all dependent on pump pulse power, but this cannot be minimized as both the artifacts and signal are correlated linearly with pump pulse power.[28]

Chirp can be considered as an artifact and decreasing it also leads to a reduction of cross phase modulation (XPM).[28] Chirp arises from the refractive index dependance on wavelength. The higher the refractive index the more light is slowed, this leads to longer wavelengths arriving earlier then shorter. To mitigate this, lenses in the probe pulse light path are replaced by concave mirrors. This removes from the light path a high refractive index material which has a larger variation of refractive index between shorter and longer wavelength. This results in a decrease in chirp from 3 ps to 400 fs across the 350 to 500 nm range, shown in Figure 2.13.

Figure 2.14 shows the reduction in the leading negative signal before the onset of the sample signal. This leading artifact is from XPM, allowing us to see how a reduction of chirp directly effects the magnitude of the XPM artifact.

To reduce stimulated Raman amplification (SRA) from the solvent, the sample pathlength needs to be minimized. This reduces the amount of material that the pump and probe pulses can interact with, which reduces the overall signal. To maintain the intensity of the sample signal, the concentration needs to be increased to compensate for the reduced pathlength. This can create problems with aggregation as solubility becomes an issue for some solutions.[22] For the samples studied this was not an issue. Reduction of solvent pathlength from 1 mm to 200 $\mu$m was achieved by a custom designed sample cell. This incorporated a 200 $\mu$m Teflon spacer sandwiched between two 2 mm thick quartz plates. The reduction of SRA was significant, Figure 2.15 shows the intensity going from seven times the TA signal to one and a half

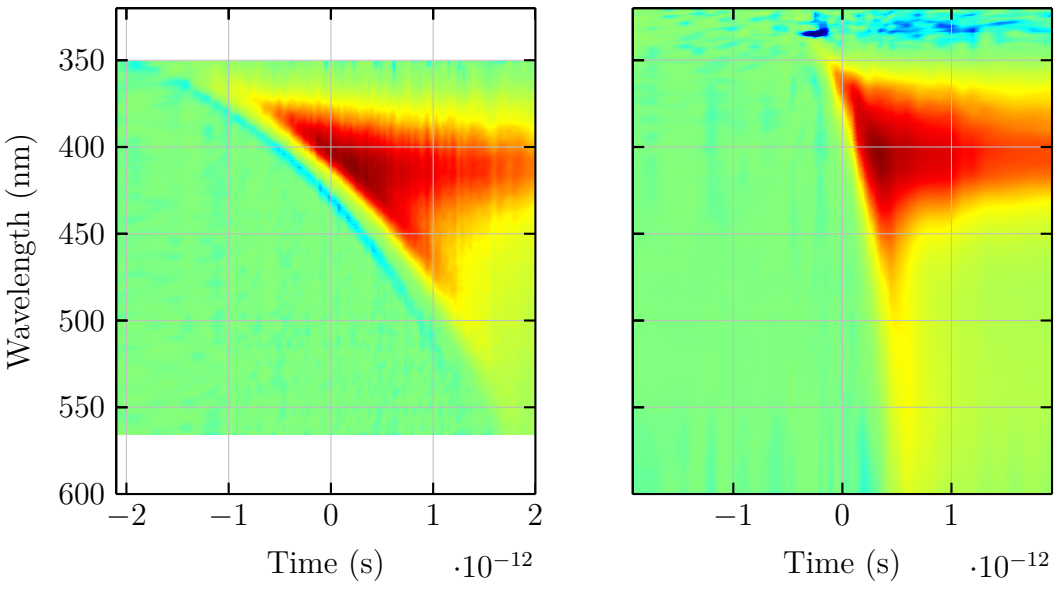


**Figure 2.13** Chirp comparison between transmissive optics (left) and reflective (right). The reduction in chirp can be see from the difference between signal onset at shorter and longer wavelengths. This has changed form 3 ps to 400 fs across the 350 nm to 500 nm range.

times. A reduction in chirp was also seen with a change from 500 fs to 450 fs in the 350 to 600 nm range. This was due to the decrease in transparent media resulting from the smaller pathlength.

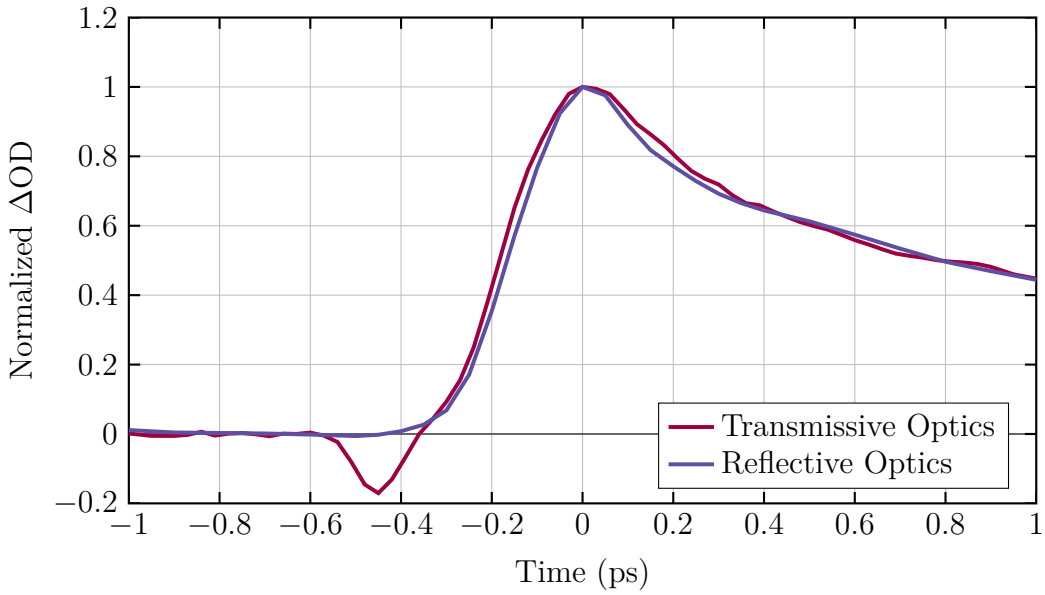


**Figure 2.14** Minimization of XPM from the implementation of all reflective optics. The transmissive optics have a dip at -450 fs, which is absent in the reflective optic setup.

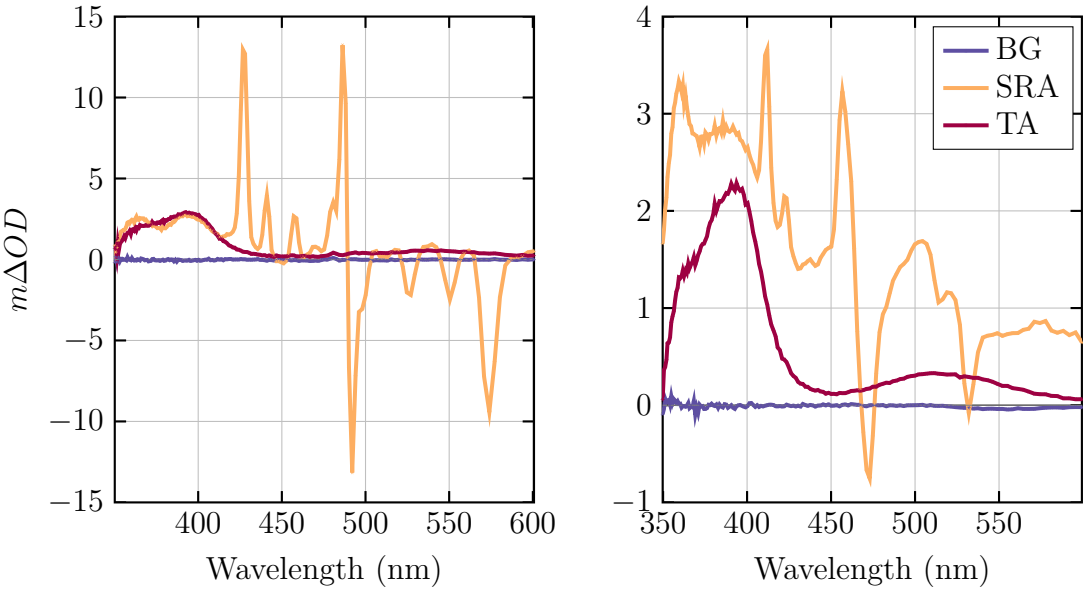


**Figure 2.15** Data collected in; *Left:* 1 mm pathlength, *Right:* 200 $\mu$m pathlength cell. Decrease of SRA intensity when compared to later time TA signal, for thinner pathlength. Stimulated Raman Amplification trace (SRA) taken at $t_0$, TA signal trace (TA) taken at 300 fs, and background trace (BG) taken before $t_0$.

## 2.3 Data Analysis

Collection of high sensitivity broad probe pulse data will provide a good basis for insight into photophysics when artifacts are properly accounted for. These include chirp, cross phase modulation, and stimulated Raman scattering. In some cases these artifacts can be corrected during the data analysis procedure.[11,20,21,28,29] Figure 2.16 shows a flow chart with all the steps taken from initial data collection to global fitting. After correcting for artifacts, and calibrating the wavelength, visual interpretation of spectral and kinetic plots is done. This gives an idea of the underlying lifetimes and number of kinetic components. The determination of the number of components can be helped by single value decomposition (SVD).[20,21,43] Using these as initial parameters the transient species kinetics can be fitted to a suitable model, this can include artifacts that perturb the data, as well as modeling the underlying photophysics.[11,20,21,43] Each of the steps involved in data analysis will be discussed below.

### 2.3.1 Artifact Correction

The utmost is done during the setup of TA to minimize artifacts, however it is not always possible to remove them completely. The next best method is to characterize them and then remove their effects from the final data. This is possible for chirp, and to some degree XPM, SRA, and TPA, but is more difficult for IRF.

#### Instrument Response Function

Deconvolution of the signal is in theory possible, but the appearance of noise in the signal makes this difficult.[20,44] As such it is not common practice to deconvolute the data before analysis, but rather any models would undergo convolution by the IRF before being fitted.[20,21] However, when initial analysis of the TA surface is done it is important to consider convolution as it leads to a shift in peaks that could affect the determination of time–zero, the onset of signals. This occurs when comparing decays with lifetimes similar to the IRF, the peaks are shifted to early time compared with those of longer lifetimes, Figure 2.17.

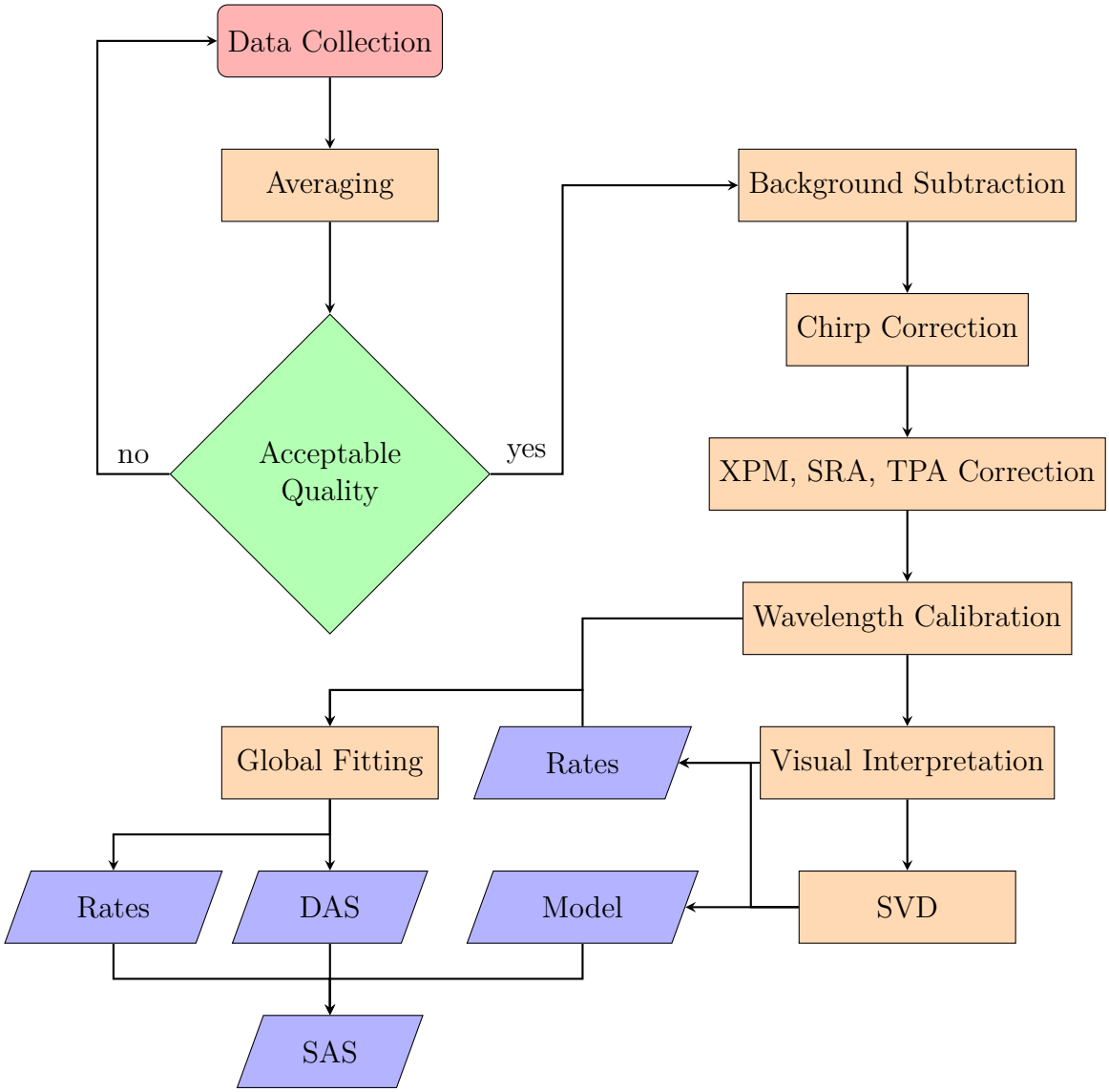


**Figure 2.16** Data analysis flow chart. SVD (single value decomposition), DAS (decay associated spectra), SAS (species associated spectra).

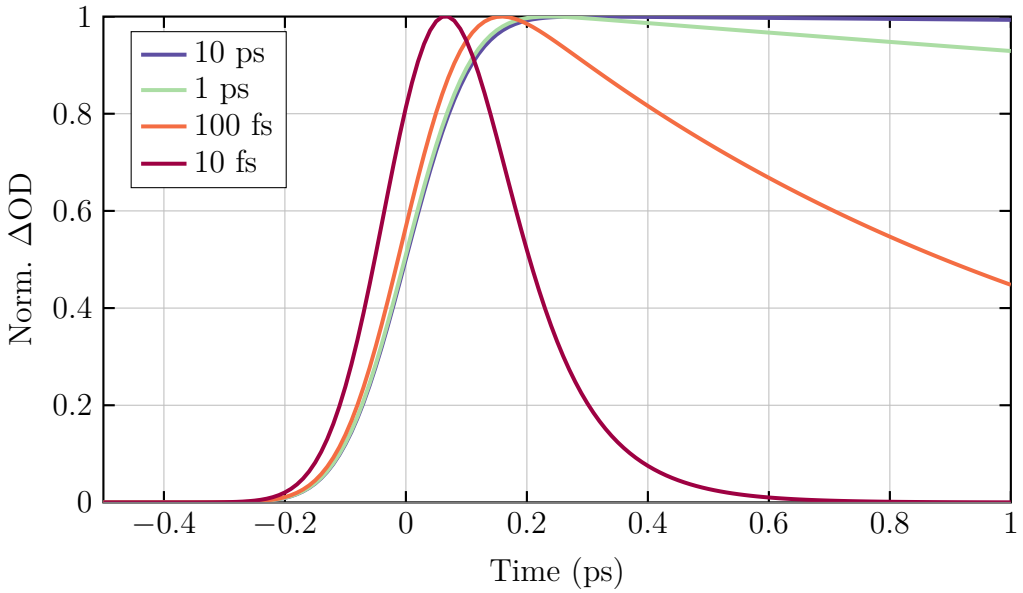


**Figure 2.17** Variation of signal peak due to convolution with IRF and underlying lifetime of species. Shorter lived signal peaks ~200 fs before the longer lived signal. Exponential decays simulated with noted $\tau$ and a IRF of 200 fs, centered at $t = 0$.

### Background Subtraction

Background subtraction is a process where the wavelength dependent signal before time equals zero is subtracted from all time points. It is used to remove artifacts that are independent of time. The most common cause are scattering of the pump pulse off; cuvette, solvent, or molecular aggregates. As the signal is not time dependent it appears before time equals zero where the signal is expected to be zero, as there is no change in absorption because the probe pulse arrives before the pump pulse.[11] The choice of negative time points to use is important as the must be significantly negative to not introduce artifacts arising from the IRF.

### Chirp Correction

Although precautions have been taken during TA setup to reduce chirp, there is still unavoidable transparent medium that the probe pulse travels through, this includes the light path through air, cuvette, and solvent. Correction for chirp can be made using software, with each wavelength offset such that time equals zero is set correctly at every wavelength. Figure 2.18 shows kinetic traces at a range of wavelengths; on the left the signal onset is spread over a 500 fs range, while on the right after correction offsets are applied time–zero is synchronized across wavelengths.

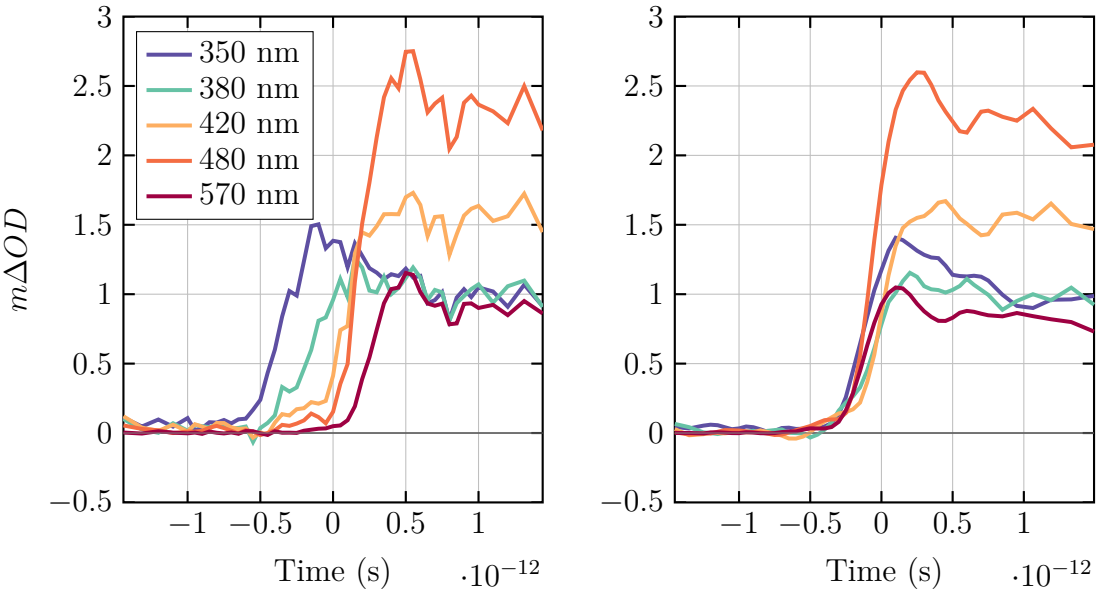


**Figure 2.18** Correction of chirp results in the signal onset overlapping at all wavelengths. Before (left), staggering of signal onset. After (right) the signal onset is simultaneous.

The difficulty in this method arises from determining the correct time offset for each wavelength. This relies on the presence of a broad signal in the spectrum that appears at time–zero. This could be from the material itself or due to one of the above discussed artifacts. The use of an artifact is preferable as it has a known relationship to time equal zero. However, there is still a downside to using XPM and SRA. XPM has a non–linear relationship to time equal zero making it more difficult to model,[28] and SRA is not a broad signal decreasing the certainty of time equal zero for the wavelengths where there is no signal.[33] The other option is to use a sample with a known long–lived broad absorption to characterize chirp, and then use this with the unknown sample. This could introduce a slight error due to refractive changes induced by different molecules in solution.

Chirp correction is carried out before wavelength calibration in order to simplify the fitting of time offsets to wavelengths. The time offsets are dependent on the refractive index of transparent medium that the probe pulse passes through. The same wavelength dependent variation in the refractive index is used to separate light in a prism spectrometer. As both the pixel and temporal domain are perturbed by the same relationship, with minor differences due to variations in refractive index between air and quartz, the resulting time offset will appear linear across pixels (Figure 2.19). This makes fitting easier, as a linear least squares method can be used. The curve is fitted by selecting points that correspond to signal onset and then performing a linear fit to get values for every wavelength.

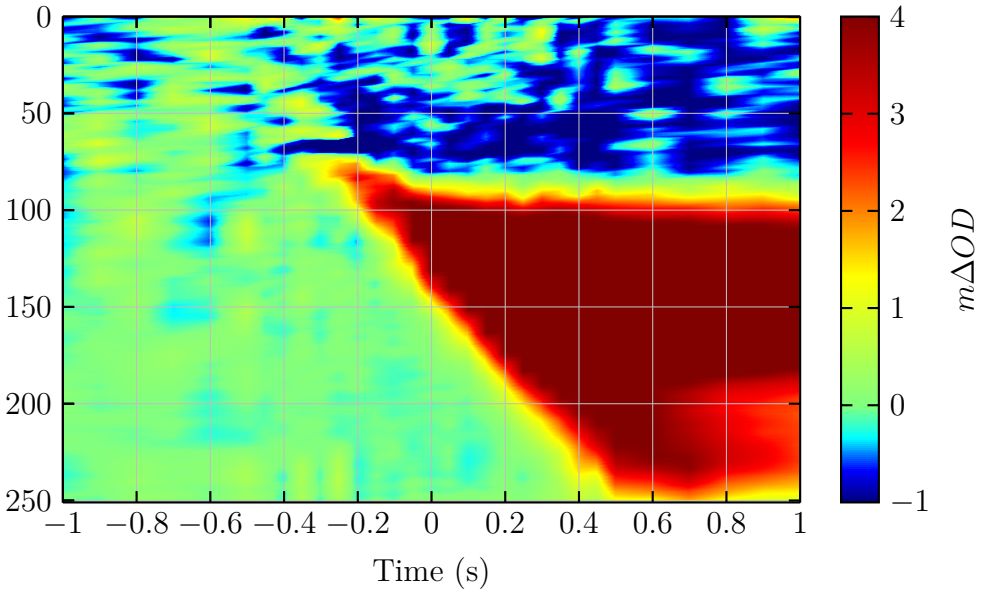


**Figure 2.19** Chirp appears linear across the TA surface when it is plotted as pixel vs time. The intensity axis (z–axis) has been cropped to highlight signal onset.

#### Two Photon Absorption, Stimulated Raman, and Cross Phase Modulation

For XMP and SRA, the collection of solvent blank and then solvent subtraction is the one solution.[19,28] Care must be taken to correct for the change in absorption once the sample is added. While chirp correction has been implemented as described above, correction for XMP and SRA proves more difficult. For SRA a second data fitting approach has been suggested to smooth out the SRA. This relies on the sharp nature of the Raman peaks compared with the broader underlying TA features.[29]

### 2.3.2 Wavelength Calibration

The use of a prism spectrometer necessitates the need for calibration due to the dispersion caused by a prism being dependent on the refractive index, prism apex angle, and the input angle.[11] To account for the deviation caused by these factors, two multi–notch filters are used to correlate wavelengths with the detector's pixels, these are BG36 and BG20 filters.[11] The absorption spectra presents many minima and maxima that can be used to determine the wavelength–pixel relationship.

This relationship is covered by the above mentioned variables, and the output deflection angle ($\theta_{out}$)can be represented by Equation 2.8, with $\theta_{in}$ representing the incident angle, and $\alpha$ the apex angle. Once the output angle is known the horizon-

tal deviation is given by Equation 2.9, with $l$ being the path length.[11] Of these only the constant offset should be unknown, but in reality the pathlength and incident angle need to be considered as well. These are optimized by using a Levenberg–Marquardt algorithm build into MATLAB, and reference spectra of both BG36 and BG20 filters. Figure 2.20 shows a comparison between the gradient of absorption spectra after wavelength corrected for both BG36 and BG20 collected via the prism spectrometer and reference spectra. There can be seen an adequate fit, with the peaks and troughs matching well across the whole wavelength range.

$$\theta_{out}(\lambda) = arcsin\left(n(\lambda) \cdot sin\left(\alpha - arcsin\frac{sin\theta_{in}}{n(\lambda)}\right)\right) \tag{2.8}$$

$$N(\lambda_i) = M - l \cdot sin(\theta_{out}(\lambda_i) - \theta_{out}(\lambda_0)) + const \tag{2.9}$$

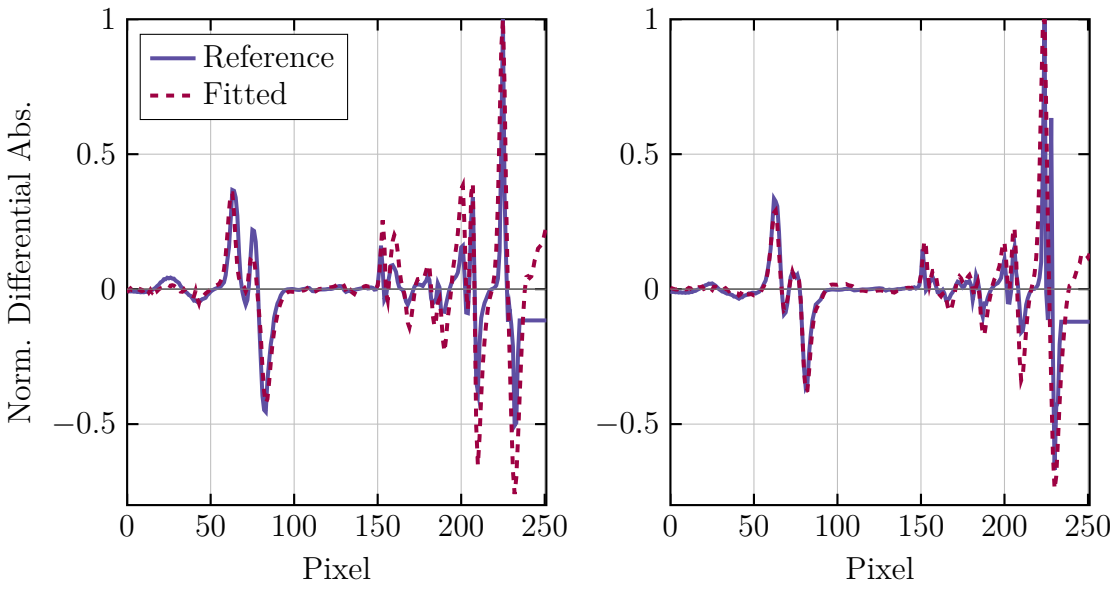


**Figure 2.20** Gradient of the absorption spectra of BG36 (left) and BG20 (right) collected using prism spectrometer after calibration in dotted red. Blue is reference spectra collected on a commercial UV/Vis spectrometer.

### 2.3.3 Interpretation of Data

After correction of artifacts, preliminary investigation of the TA surface can be done. This can be used to compare spectral and kinetic data between different samples and also to guide the design and input parameters of further data modeling. Presented below are a few spectral and kinetic traces, with basic features described. The data used was from the compounds to be discussed in the coming chapters, here only a

brief description of the data will be made.

### Spectral Components

Figure 2.21 provides an example of spectral slices of the TA surface of azobenzene taken at different time intervals. Important information is gained from this, including the visualization of GSB, which can provide yield information and the number of states involved in the decay.

The the transition through zero at a wavelength where there should be GSB (350 nm) indicates there is overlap of GSB with PIA components. This means the intensity of the GSB signature is reduced, making it harder to ascertain the concentration of molecules in the excited state. There are three PIA features at 360 nm, 390 nm, and 465 nm, each decaying with a different lifetime. The peak at 465 nm disappears after 300 fs, 390 nm after 10 ps and 360 nm does not disappear over the timescale shown. This indicates a minimum of three intermediates along the relaxation pathway.

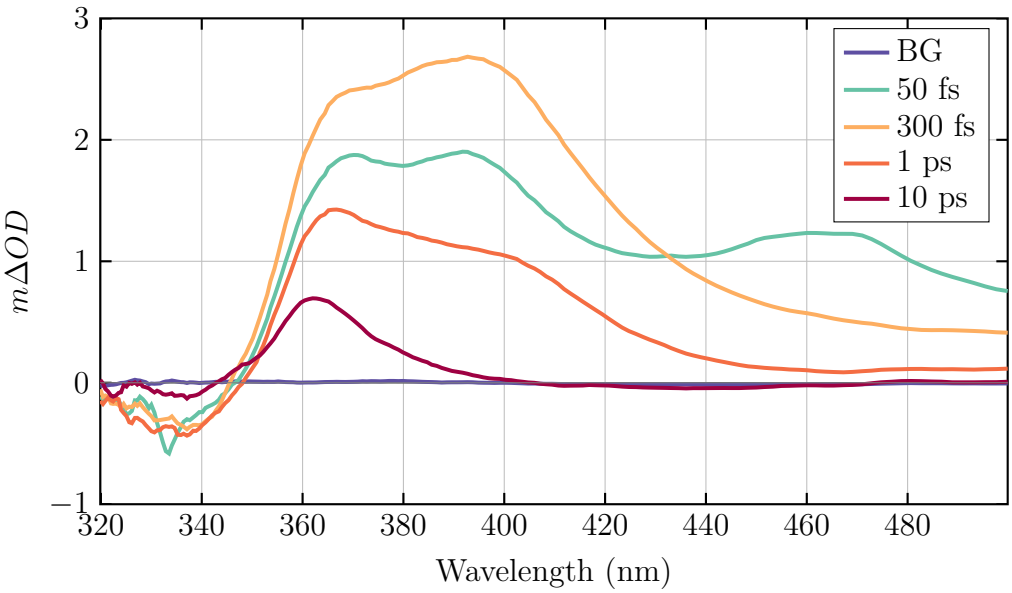


**Figure 2.21** Spectral slices of 1 $\mu M$ azobenzene in acetonitrile with 300 nm excitation, taken at various time delays.

Another approach is to compare the spectral slices between compounds of interest. Of most interest are the spectral shapes, and estimates of the decay rates and this is done by normalizing each species with respect to the intensity of the first one. For this example Figure 2.22 is used with azobenzene (AB) being overlayed with foldamer one (F1).

This shows that after 10 ps, F1 still has a signal from the state corresponding to 410 nm, while it is absent in azobenzene. The short lived AB state at 460 nm, is

not noticeable in F1 but there is indication of a peak at 550 nm. From this it is noted that there is a difference in the photophysics of the two compounds, with the decay state corresponding to 460 nm absorption being hindered in F1.

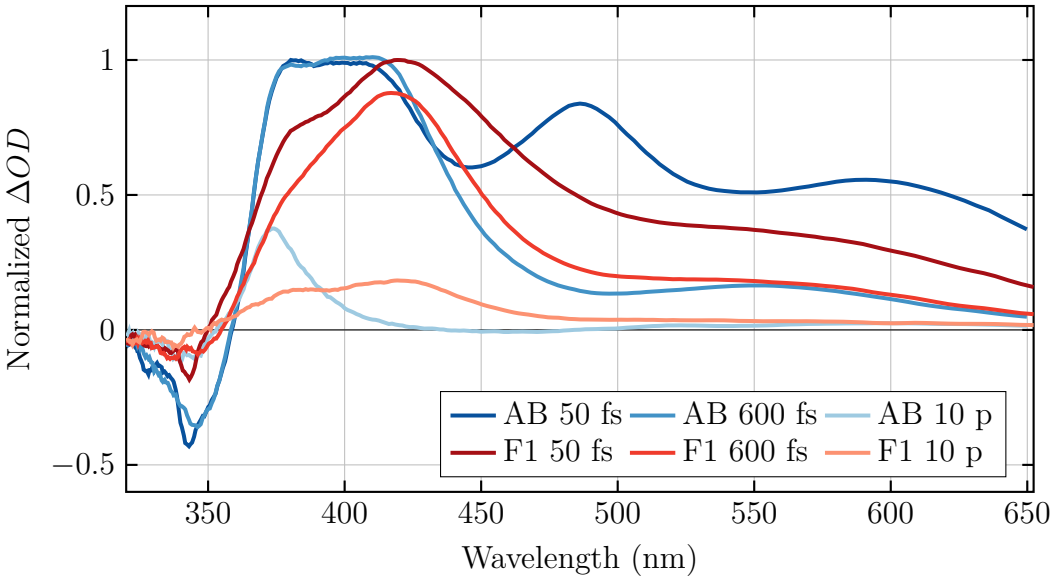


**Figure 2.22** Spectral slices of 1 $\mu M$ azobenzene and 0.5 $\mu M$ F1 both in acetonitrile with 300 nm excitation. Overlaid to compare the spectra differences at various time delays

### Kinetic Components

While some kinetic information can be derived from the change in intensity of the spectral slice, it is best to check the kinetic traces at a given wavelength. This prevents any spectral trace that is and outliers due to pump or probe pulse fluctuation leading to misinterpretation, it also allows checking of all time points overcoming the need to select the right time for a spectral slice.

In a similar manner to spectral data, kinetics slices can be taken at particular wavelengths. Figure 2.23 presents kinetic traces for oxazine (OX), traces normalized by intensity are also presented. The trace at 405 nm shows an initial decay, but then grows again after 10 ps, this is similar to 330 nm, which is initially comprised of GSB and PIA, and becomes dominated by PIA after this time. This indicates at least two states being present at later times. The 330 nm trace overlaps with the absorption band OX, and this is consistent with the existence of another state, as the GSB grows in as an overlapping PIA decays. More evidence for this can be seen in the 365 nm trace, which has a minimum at early time, due to this being within 200 fs the effects of artifacts must be kept in mind. Looking at the trace there is evidence for three intermediates, with one appearing in on the nanosecond timescale.

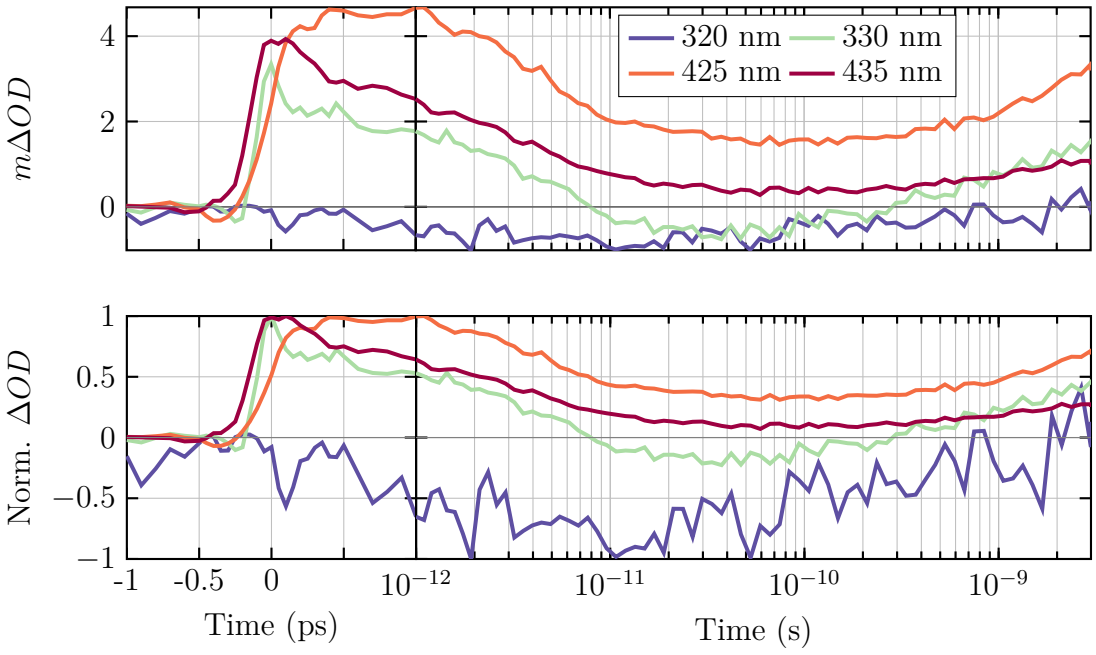


**Figure 2.23** Kinetic traces of 1 $\mu M$ oxazine in acetonitrile with 300 nm excitation at various wavelengths. The top shows spectral slices in $m\Delta OD$ and the bottom has the same traces normalized.

Figure 2.24 shows OXF in two different solvents, acetonitrile and hexane. It can be seen at both 425 nm and 535 nm that there is a difference in kinetic profile. In acetonitrile recovery occurs after 80 ps while hexane sees a decay over the whole temporal range. This shows that OXF has solvent dependent behavior.

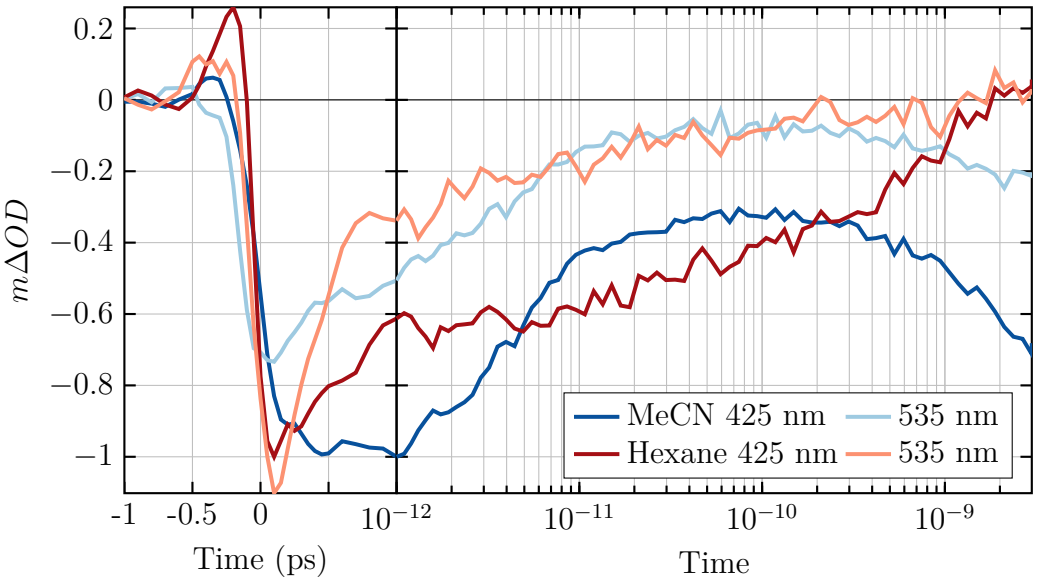


**Figure 2.24** Comparison between the decay dynamics of 1 $\mu M$ oxazine with 300 nm excitation in acetonitrile and hexane. Differences can be seen by comparing the decay shapes.

### 2.3.4 Data Modeling

Data modeling is important in the interpretation of TA results due to the large amount of data generated (eg., each TA surface consists of 251 spectral values and at least 150 time points). The use of data modeling allows the reduction to highlight the underlying chemical or physical processes. A variety of techniques have been applied to model TA data and they all require some chemical insights before fitting.[20,21]

There are two general categories of techniques commonly applied, these are 'soft' and 'hard' modeling.[21] In hard modeling, the TA surface is considered to be comprised of the sum of exponential decays or growths, with a correlation between the decay rates at each wavelength. In contrast, soft modeling starts from an underlying assumption that the TA signal is made up of the sum of molar extinction coefficients corresponding to the transient species present. With soft modeling the decays and molar extinction coefficients are not parametrized by a mathematical model, but are instead constrained by know physical properties of the materials being studies. This is the basis for the models, which then use a number of fitting techniques to determine the free parameters required for fitting TA data.[20–22,43] A number of good reviews can be found covering the modeling and techniques used for fitting TA data in detail.[20,21] For this work we have focused on implementing a global fitting routine in MATLAB. This will be expanded on in future work and is beyond the scope of this project.

### Global Fitting

For processing the data generated during the study of AB, foldamer, and OX a global fitting algorithm was implemented using MATLAB. Global fitting takes advantage of the wavelength correlation inherent in the TA data, it applies one set of decays at every wavelength to determine the best fit.[11,20]

The data can be considered to be composed of spectral and temporal components with each component contributing to the overall spectral and temporal signal. These contributions are due to their time dependent concentration $c_n(t)$ and the wavelength dependent molar extinction coefficient $\epsilon_n(\lambda)$, Equation 2.10.

$$S(\lambda, t) = \sum_{n=1}^{n_{comp}} c_n(t)\epsilon_n(\lambda) \tag{2.10}$$

The aim is to find the best fit for these underlying components. To achieve this, a mathematical expression is defined for the dependence of either the spectral shapes or temporal profiles, and these are used fit a second component. The temporal profile is the first step in the model developed. Equation 2.11 gives a simple equation to model each temporal component, this arises from kinetic models that can be decomposed into exponential decays.[20] For each wavelength the overall signal is composed of the sum of exponential decays or growths, with wavelength dependent pre–exponential factors and a consistent set of decay rates across every wavelength. An adjustment needs to be made due to the IRF as the data cannot be deconvoluted before and this necessitates Equation 2.12 being used in place of the exponential term.[20] This represents an analytical solution to the convolution of a exponential decay and Gaussian profile centered at time–zero. The use of exponential decays or growths is not a restriction of the model, any time–dependent decay could be used, it has been chosen due the theoretical calculation of how excited species decay.[20]

$$S(\lambda, t) = A_1(\lambda)e^{-k_1 t} + A_2(\lambda)e^{-k_2 t} \cdots A_n(\lambda)e^{-k_n t} \tag{2.11}$$

$$e^{-k_n t} * IRF(\Delta) = \frac{1}{2}e^{-k_n t}e^{\frac{(k\Delta)^2}{2}}\left(1 + erf\left(\frac{t - k\Delta^2}{\sqrt{2}\Delta}\right)\right) \tag{2.12}$$

A non–linear least squares fitting algorithm built into MATLAB is used (lsqcurvefit), this minimizes the residuals by varying the decay constants (k). To calculate the residuals a model was implemented using the Equation 2.11 to give the temporal profile for each component. With the determination of the pre–exponential factors done by a linear least–squares fit at each wavelength. This determined how heavily each exponential factor contributes to the observed signal at each wavelength.

The wavelength dependent weighting is called a decay associated spectrum (DAS) it shows how much each decay rate contributes to the overall time profile at each wavelength. This contribution can be attributed to either the growth or decay of a feature at the given rates, this is dependent on both the sign of the DAS, and the underlying features. For a positive TA signals (PIA and SE) a positive DAS corresponds to a decay and a negative growth, for negative TA signals (GSB) the opposite is true.

Once fitting is completed we are left with the underlying decay rates (k) and the DAS. Interpretation of the DAS can be made by applying a kinetic model, leading to a species associated spectrum (SAS) for each underlying component.[20] SAS corresponds to the absorption spectra of a species present upon evolution of the excited state, i.e a single excited state. To understand the transformation from the DAS to SAS we need to consider how to construct the DAS from SAS. Equations 2.13 show how each DAS is comprised of weighted components ($w_{ni}$) of each SAS.

$$\begin{bmatrix} DAS_1 \\ DAS_2 \\ \vdots \\ DAS_n \end{bmatrix} = \begin{bmatrix} w_{11} & w_{12} & \cdots & w_{1i} \\ w_{21} & w_{22} & \cdots & w_{2i} \\ \vdots & \vdots & \ddots & \vdots \\ w_{n1} & w_{n2} & \cdots & w_{ni} \end{bmatrix} \begin{bmatrix} SAS_1 \\ SAS_2 \\ \vdots \\ SAS_n \end{bmatrix} \tag{2.13}$$

Determination of these weightings is made by applying a kinetic model, in this case an unbranched unidirectional model will be used. This consists of a simple decay from one state to another as illustrated by Equation 2.14. Equation 2.15 gives the relation between the underlying decay rates of three states with the concentration normalized by the starting concentration of the first species.[20] The weighting of each exponential towards the species concentration is determined by the decay rates.

$$SAS_1 \xrightarrow{k_1} SAS_2 \xrightarrow{k_2} SAS_3 \cdots SAS_{n-1} \xrightarrow{k_{n-1}} SAS_n \tag{2.14}$$

$$\begin{bmatrix} [C]_1 \\ [C]_2 \\ [C]_3 \end{bmatrix} = \begin{bmatrix} 1 & 0 & 0 \\ \frac{k_1}{k_2-k_1} & \frac{k_1}{k_1-k_2} & 0 \\ \frac{k_1k_2}{(k_2-k_1)(k_3-k_1)} & \frac{k_1k_2}{(k_1-k_2)(k_3-k_2)} & \frac{k_1k_2}{(k_1-k_3)(k_2-k_3)} \end{bmatrix} \begin{bmatrix} e^{-k_1t} \\ e^{-k_2t} \\ e^{-k_3t} \end{bmatrix} \tag{2.15}$$

This provides the information needed to re–weight the DAS to generate a SAS, as the weightings of the first exponential are given by the first column and so forth for the remaining exponential. Equation 2.16 is the final form used to transform the DAS to SAS, assuming an unbranched unidirectional model. This gives quantitative data on the underlying species spectral shapes and their decay rates.[20]

$$\begin{bmatrix} DAS_1 \\ DAS_2 \\ DAS_3 \end{bmatrix} = \begin{bmatrix} 1 & \frac{k_1}{k_2-k_1} & \frac{k_1k_2}{(k_2-k_1)(k_3-k_1)} \\ 0 & \frac{k_1}{k_1-k_2} & \frac{k_1k_2}{(k_1-k_2)(k_3-k_2)} \\ 0 & 0 & \frac{k_1k_2}{(k_1-k_3)(k_2-k_3)} \end{bmatrix} \begin{bmatrix} SAS_1 \\ SAS_2 \\ SAS_3 \end{bmatrix} \tag{2.16}$$

From this process we have gathered information on both the decay rates and spectra of intermediates that are related to the model chosen. Figure 2.25 contains a surface from oxazine, the results of global fitting (this includes the DAS, SAS and the corresponding temporal decays associated with each). The SAS has been made by assuming an unbranched unidirectional model as described above. The concentration of each species is also shown, this was calculated using the decay rates for each state and the unbranched unidirectional model.

The difference between the DAS and SAS can be observed by considering the concentration profile (Figure 2.25 right). In contrast to the DAS, which has exponential decays, we can now see a build up of SAS2-4 at different time intervals with SAS1-3 decaying within our time resolution. By applying a model to transform the DAS into SAS it is easier to associate the spectra with underlying species. The DAS can contain contributions from the decay of one state into another with overlapping spectral features. This makes interpretation of the DAS difficult if there are a mixture of decay and growth signals over the wavelengths.

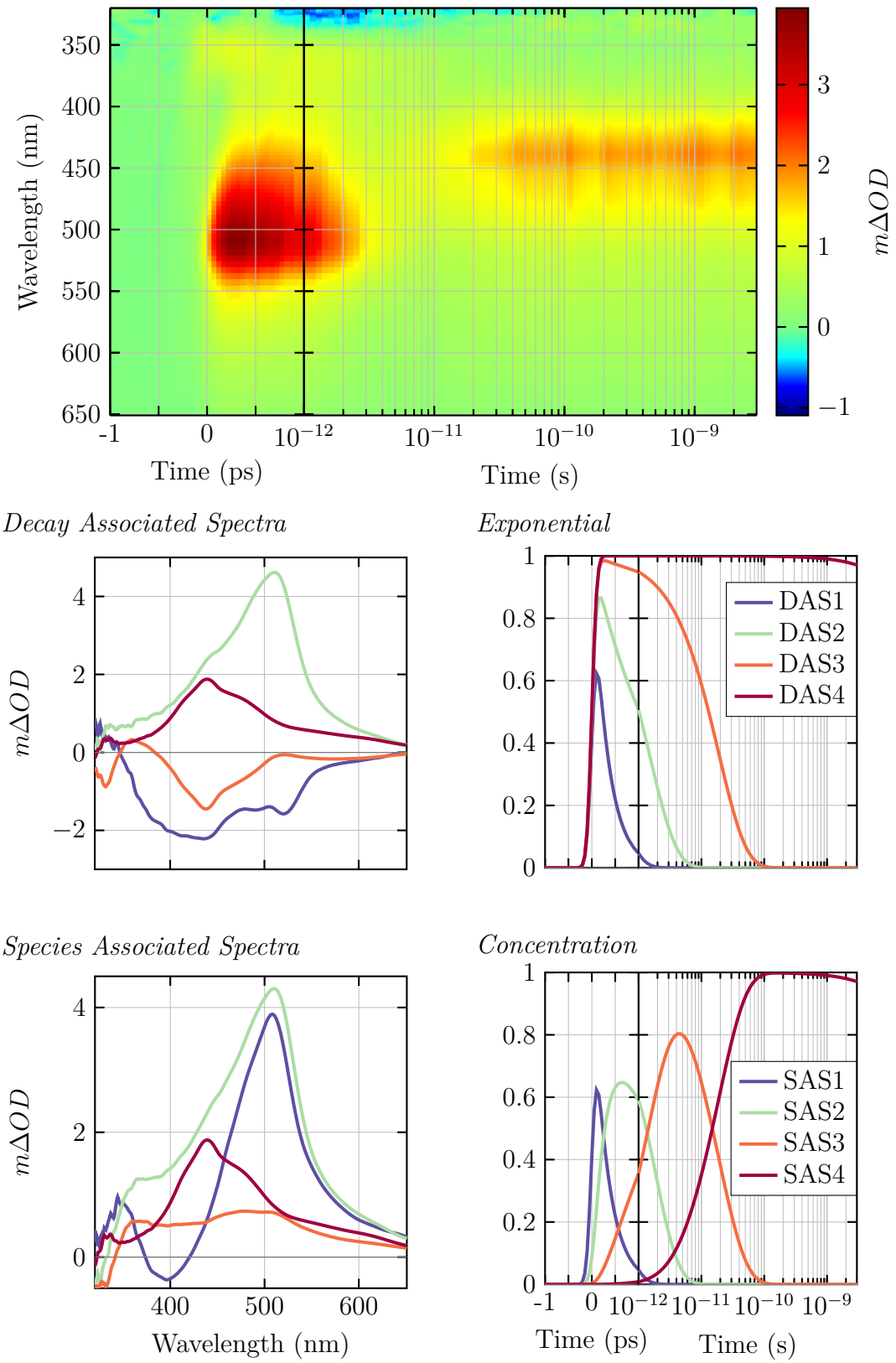


**Figure 2.25** Top is a TA surface of 1 $\mu M$ oxazine (OX) in acetonitrile with 300 nm excitation. This is then global fit to give the SAS, with the corresponding decay profiles on the right, the decays are single exponential. Below this is the SAS constructed from the DAS using an unbranched unidirectional model, to the right are the concentrations of each species under this model.

# Chapter 3

# Photo–isomerization of Azobenzene

## 3.1 Introduction

Azobenzene has been incorporated into a number of photo–active materials and molecules, due to its efficient and reversible photo–isomerization.[16,45,46] This photo–isomerization between two geometries; *cis*, and *trans* is shown in Figure 3.1. This isomerization leads to changes in both structural and optical properties.[16,46,47] The structural change of azobenzene that occurs with photo–isomerization is of interest as it is harnessed by the foldamer molecule which contains the azobenzene moiety discussed in Chapter 4. Azobenzene will be studied in the solvent systems needed to activate the foldamer (acetonitrile and tetrahydrofuran). This is done to differentiate the effects that are inherent in azobenzene from those that occur due to the foldamer.

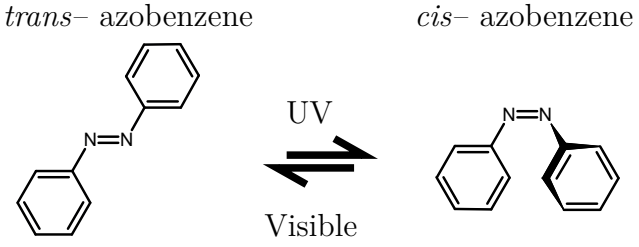


**Figure 3.1** Two conformations involved in the photo–isomerization of azobenzene. The *cis* form is reached after irradiation with ultra–violet light, and the *trans* form by visible light.

Measurements of azobenzene also provide a well known reference[13–17,46] with which to benchmark the improvements made to the transient absorption (TA) setup. These

measurements will confirm that the adjustments made to the TA setup provide the temporal and spectral resolution necessary for measurements of the azobenzene and the foldamer.

## 3.2 Photo–isomerization

Azobenzene has two optically active electronic transitions, see Figure 3.2. The symmetry forbidden $S_0 \rightarrow S_1$ ($n \rightarrow \pi^*$ ) transition has a much lower absorption coefficient ($\epsilon$) than the allowed $S_0 \rightarrow S_2$ ($\pi \rightarrow \pi^*$) transition. The $S_0 \rightarrow S_2$ transition occurs around 320 nm for the *trans* and 290 nm for the *cis* isomer. With the $S_0 \rightarrow S_1$ transition being around 450 nm for *trans* and 430 nm for the *cis* isomer.[46]

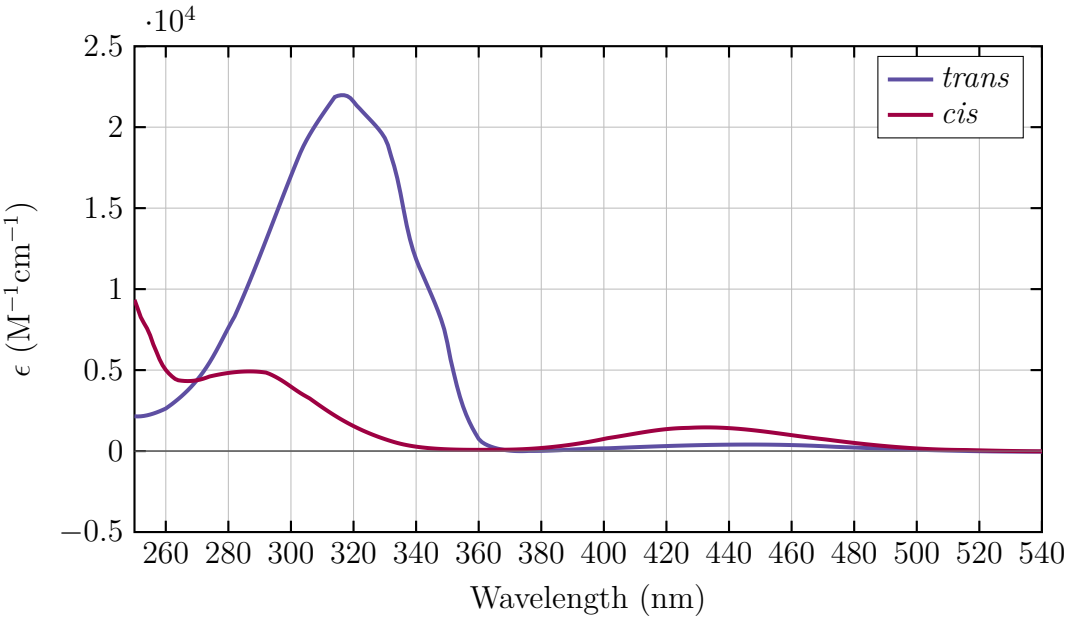


**Figure 3.2** The absorption spectra for *trans* (blue) and *cis* (red) azobenzene in ethanol.[46]

The absorption spectra of the *trans*– and *cis*– azobenzene isomers overlap and both conformations undergo photo–isomerization into the other isomer. Consequently, both species will always be present regardless of the wavelength of irradiation, as neither isomer can be selectively excited. The ratio of *trans*:*cis* under continuous irradiation of any source of light at a given wavelength ($\lambda$) is termed the photo–stationary state (PSS). It occurs at the ratio in which the *cis* to *trans* isomerization rate equals that of *trans* to *cis*. The PSS is determined by Equation 3.1,[48,49] with the absorption coefficient ($\epsilon$), quantum yield of isomerization ($\phi$) (which is dependent on both species and wavelength) and the rate of thermal relaxation factoring into the final ratio of *trans* to *cis*. Thermal relaxation is excluded as it normally occurs on a substantially longer timescale than photo–isomerization.

$$\left(\frac{[AB]_{trans}}{[AB]_{cis}}\right)_{\lambda_{ex}} = \frac{\phi_{cis}}{\phi_{trans}}\frac{\epsilon_{cis}}{\epsilon_{trans}} \tag{3.1}$$

The photo–isomerization quantum efficiency is higher for *cis* to *trans* isomerization than for the reverse *trans* to *cis* isomerization, from both the $S_1$ (0.46 *cis* to *trans*, 0.31 *trans* to *cis*) and the $S_2$ states (0.35 *cis* to *trans*, 0.15 *trans* to *cis*).[49,50] While the absolute value is solvent polarity and viscosity dependent, it is found that the *cis* isomer efficiency is always higher than the *trans* isomer.[50] The higher extinction coefficient for the $S_2$ transition of *trans* overcomes the lower yield meaning exposure to UV light results in mostly the *cis* isomer photo–stationary state (PSS) 1:9 (*trans*:*cis*). With irradiation of visible light, the higher extinction coefficient for the $S_1$ and the higher yield of the *cis* isomer gives a mostly *trans* isomer with a PSS 8:2 (*trans*:*cis*).

The generation of PSS enables light–control of azobenzene on the molecular scale. Exposure to UV light results in a *cis*–dominated PSS, and exposure to visible light gives a *trans*–dominated PSS.[46] The ability to generate different conformations gives rise to changes in properties between the *cis* and *trans* isomers that can be taken advantage of. One method of harnessing the photoisomerization uses molecular design to amplify the conformational changes, influencing the larger macro–structure of a molecule. The foldamer series of compounds described in Chapter 4 take advantage of azobenzene photo–isomerization in this manner to allow light–controlled capture and release of chloride ions.[12]

### 3.2.1 Mechanism

The pathway between *trans*– and *cis*– isomer may involve rotation of the phenyl groups in the molecular plane, which is referred to as inversion. Alternatively, it may occur by out of plane rotation, which is referred to as the rotation mechanism. These pathways, as well as a mixed inversion–rotation pathway, are illustrated in Figure 3.3.[51]

A number of studies have been completed to determine the most likely mechanism of isomerization; these include both experimental and computational studies.[13,14,25,52] The focus has been on the *trans* to *cis* isomerization, with excitation to both the $S_2$ and $S_1$ states, as well as solvent effects.[14,51] It shows the quantum efficiency for

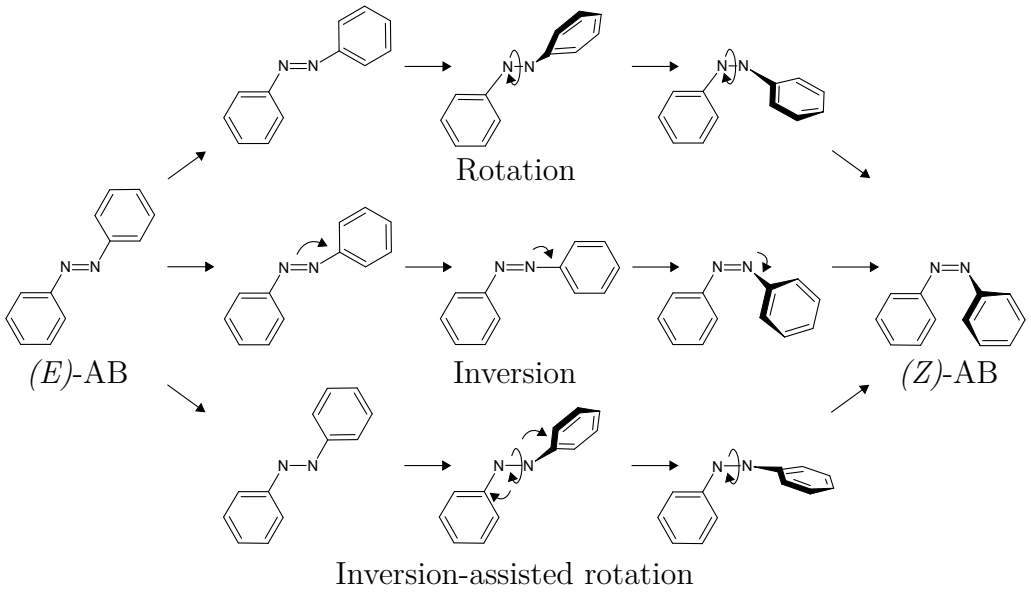


**Figure 3.3** The three possible isomerization pathways of azobenzene (AB); rotation about the nitrogen–nitrogen bond, inversion involving in plane motion of the phenyl group, and inversion assisted rotation with rotation around the nitrogen–nitrogen bond and in plane movement of the phenyl group.[51]

the relaxation from the $S_2$ to $S_1$ is almost unity, which suggests that isomerization occurs from the $S_1$ state.[14] There is evidence that the excitation wavelength has an impact on the isomerization dynamics,[13] with excitation to the $S_2$ state having a different yield than $S_1$ depending on the excitation energy.[52] This could lead to two possible relaxation pathways. One from a vibrationally excited $S_1$ state and the other from a vibrationally relaxed $S_1$ state.[53]

The influence of solvents and substituents on isomerization has also been investigated. Variation of solvent viscosity leads to the suppression of the rotation pathway and favoring of the inversion pathway.[25] Substituents also have an effect on isomerization with inversion becoming more favorable when bulky groups are attached to the phenyl rings.[25] The general outcome from previous studies is that a rotation mechanism is favored and there are contributions from inversion, with the observed pathway influenced by both solvent[13] and substituent effects.[51,52]

## 3.3 Thermal Isomerization

It is important to consider the rate of thermal isomerization for transient absorption (TA) measurements, as data collection can typically take 30 – 60 minutes, and the time between collection points is approximately 333 $\mu$s in the setup used. Over the collection period there can be no significant build–up of photo–product, to facilitate

this, any back reaction must occur in less than 333 $\mu$s.

The thermodynamic minimum configuration for azobenzene is *trans* isomer, this is 10 – 12 Kcal mol$^{-1}$ more stable than *cis*.[54] In the dark it will isomerize back to 99.9% *trans* isomer, with a half–life of about two days.[54,55] The rate of thermal isomerization is also affected by solvent[55] and pH.[25] For solvents it has been shown that an increase in polarity leads to faster isomerization. This can be rationalized in terms of the stabilization of the polar transition state.[46,56] Effects caused by pH are due to acidic conditions that favor the formation of an azobenzene ion. This is because a nitrogen atom is protonated, weakening the nitrogen–nitrogen double bond, increasing the isomerization rate.[57]

Due to build–up of the *cis* isomer it is important to minimize the change in species being studied by subsequent data collection points, meaning that the species present is the same after each 333 $\mu$s interval. Using solvent and pH changes to minimize this build up is not viable due to the effect it would have on the foldamers conformation or dynamics. The generation of a steady ratio was achieved by continuous illumination with 365 nm light from a high–power LED. Figure 3.4 shows the build up of the *cis* isomer over 30 minutes irradiation with the 300 nm laser light from the same source as that being used for TA measurements, and the the formation of the PSS once the sample was irradiated for 40 minutes with 365 nm light from the high–power LED. Figure 3.4 also shows the absorption spectra before and after a TA run of 60 minutes with constant illumination with the 365 nm high–powered LED set to 800 mA, it is shown that there is no noticeable change in the azobenzenes absorption spectra. The method of continuously irradiating the sample with 365 nm light is used to generate a *trans* dominated PSS for all TA measurements involving azobenzene (Sections 3.5 & 3.4) and the foldamer family of molecules (Chapter 4).

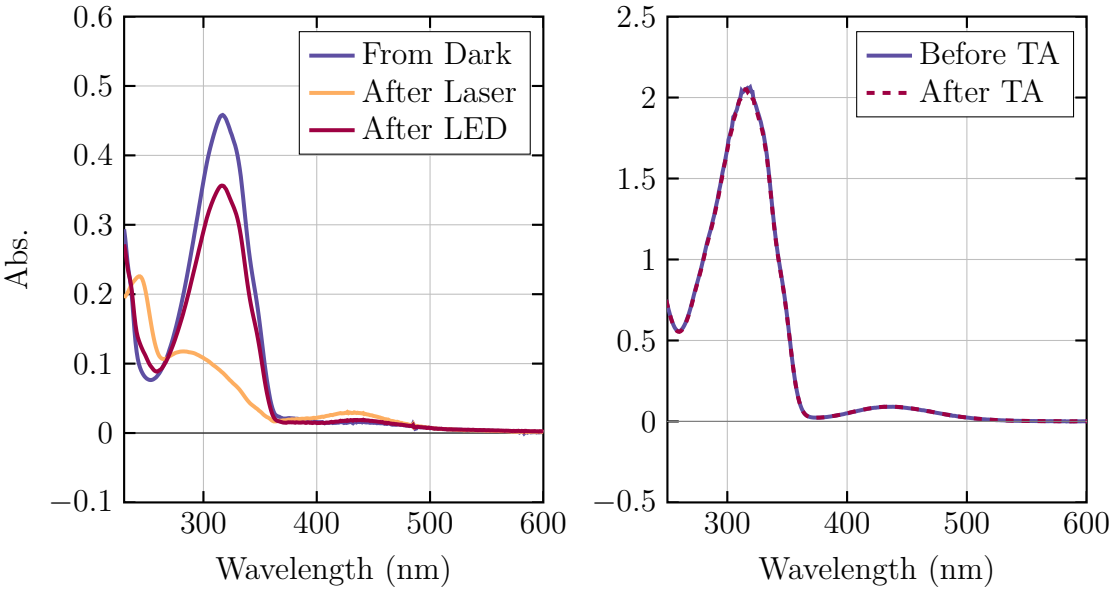


**Figure 3.4** *Left:* The effect of exposure to 300 nm laser excitation pulse (yellow) showing the build–up of the *cis* isomer. The formation of the PSS after irradiation at 365 nm using a high–powered LED (red). *Right:* Before and after a TA experiment when sample was under constant 365 nm illumination.

## 3.4 Benchmark and Validation of Transient Absorption Setup

Azobenzene was used as a reference compound to check the modifications made to the TA setup. This involved checking both the temporal resolution and spectral range via comparisons to literature studies of azobenzene.

Figure 3.5 shows a comparison between data collected by Satzger *et al.*[17] and that collected on the setup used in this work. It presents four spectral slices, 200 fs, 500 fs, 2 ps, and 5 ps. The spectra are compared by normalizing the peak intensity to the 500 fs trace for both sets of data. The 200 fs slice has the most variation, the peak at 390 nm has half the intensity compared to that of the reference trace. This can be attributed to the sensitivity of the early time signal (<200 fs) to changes in instrument response function (IRF) and the position of time–zero. In the early trace it is important to note the peak positions, a good match is observed between the two most prominent peaks at 390 nm and 460 nm. Later time traces match well with the 2 ps slice containing the shoulder at 400 nm. The 5 ps spectral slice has no noticeable features in the 380 – 650 nm range.

The trace at 5 ps in Figure 3.5 highlights the benefits of extending the UV spectral

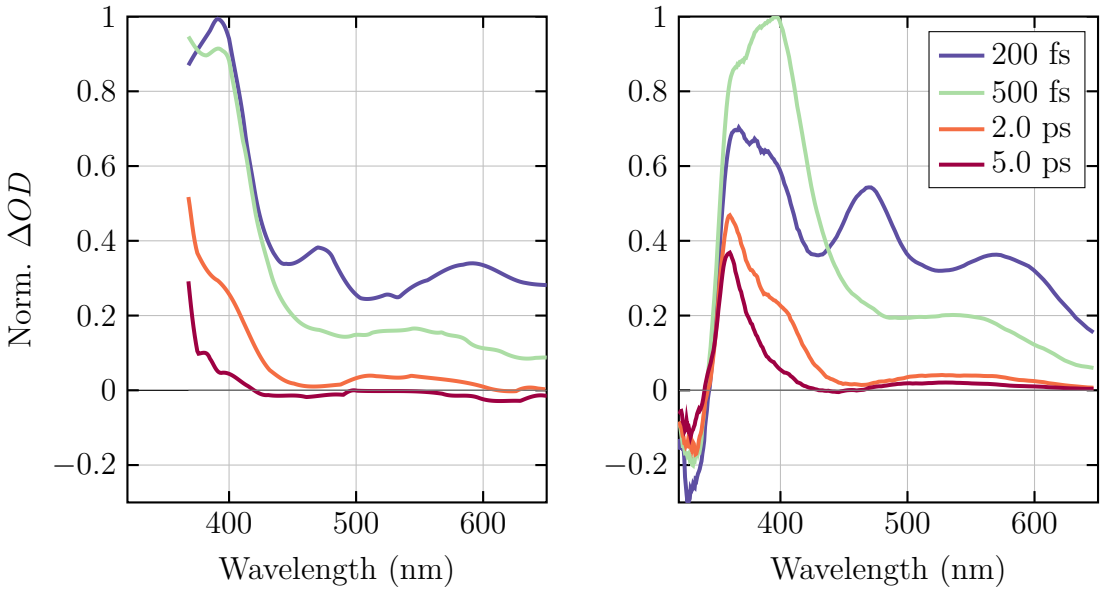


**Figure 3.5** Comparison of literature and collected azobenzene spectral slices. Left: 22 $mM$ azobenzene in ethanol with 340 nm excitation collected by Satzger *et al.*[17] Right 1 $\mu M$ azobenzene in acetonitrile with 300 nm excitation collected after improvement to TA setup implemented. Each data set is normalized by the 500 fs intensity.

range down to 310 nm. With the increased range a distinct peak at 360 nm is observed, whereas in the data published by Satzger *et al.*[17] only the band edge was observed. The decay of this could be different, or its presence could be mis–assigned to noise. The other benefit of our setup is in the resolution of the ground state bleach (GSB), which can be seen in the 350 – 310 nm region. Resolution of the GSB allows identification of the relaxation of the excited species to the ground state, including thermalization in the electronic ground state. This gives a baseline in which to look for photo–induced absorption (PIA) and stimulated emission (SE) spectral features.

## 3.5 Transient Absorption Results

Figure 3.6 shows the TA surface and kinetic traces of flash–photolysed azobenzene collected in acetonitrile. There are three PIA peaks present; 470 nm, 390 nm, and at ~360 nm with the GSB spectral feature observed in the 340 – 320 nm region.

The PIA at 470 nm decays in less than 200 fs, with the lifetime resolution limited by the IRF. The peak at 390 nm overlaps with the peak at 360 nm at early time but can be separated at later times (>3 ps). This is due to the differing lifetimes for each signal component, with global fitted decays giving lifetimes of 1 ps for the

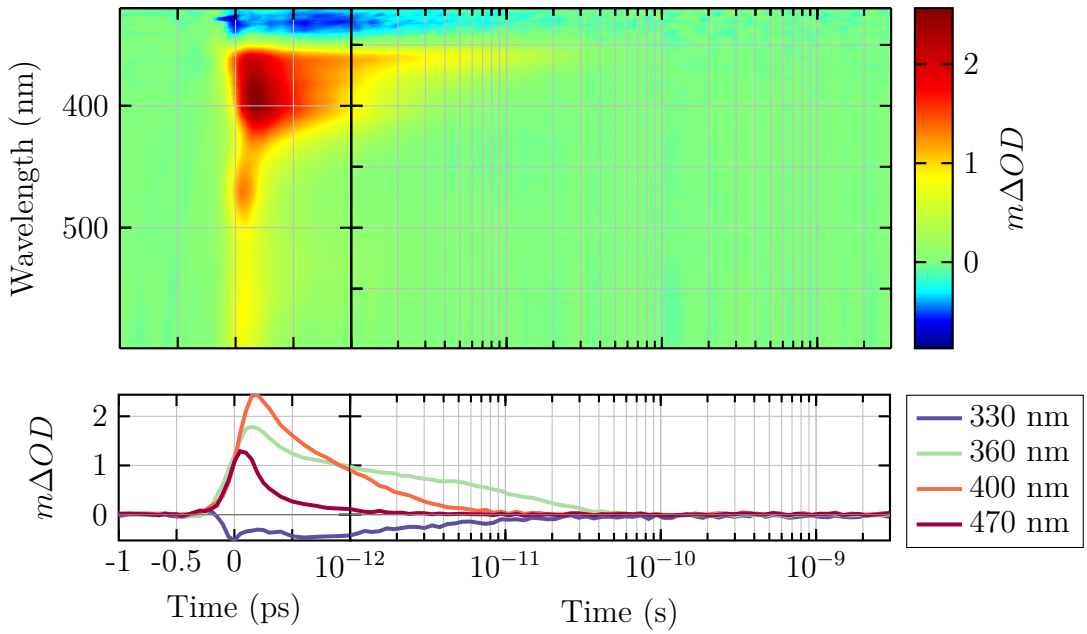


**Figure 3.6** TA surface for 1 $\mu M$ azobenzene in acetonitrile with 300 nm excitation. *Top:* TA surface. *Bottom:* Kinetic traces at various wavelengths.

390 nm feature and 10 ps for the ~360 nm PIA. This significant difference can be easily observed in the time domain, with the ~360 nm still being present after tens of picoseconds. The GSB decays with lifetimes relating to each of the PIA features. This is expected as the GSB is related to the depletion of ground state molecules as they have been excited.

The observed lifetimes fit well with literature. There are three quoted lifetimes, one on the order of 100's of femtoseconds, another at ~1 ps and the last between 10 and 20 ps.[15–17,58] They can each be attributed to the reaction coordinate surfaces as described in Figure 3.7.[17]

Excitation to the $S_2$ state relaxes to the $S_1$ in less than 200 fs. From here a conical intersection and branching occurs on the ~1 ps timescale. There have been two interpretations of this lifetime. First from the TA data, it is found to be the lifetime of the $S_1$ state. The second is from a recent femtosecond stimulated Raman result, where it is attributed to the formation of the *cis* photo–product.[59] This suggests that branching occurs somewhere on the $S_1$ surface.

The final lifetime corresponds to relaxation of the *trans* isomer to its thermal ground state, on the tens of picoseconds timescale.[60] Relaxation to the ground state is signified by a bathochromic shift in absorption, this appears in the TA signal as there is PIA feature overlapping with the GSB. Figure 3.8 illustrates the electronic transitions that are responsible for the bathochromic shift. The blue arrow indicates

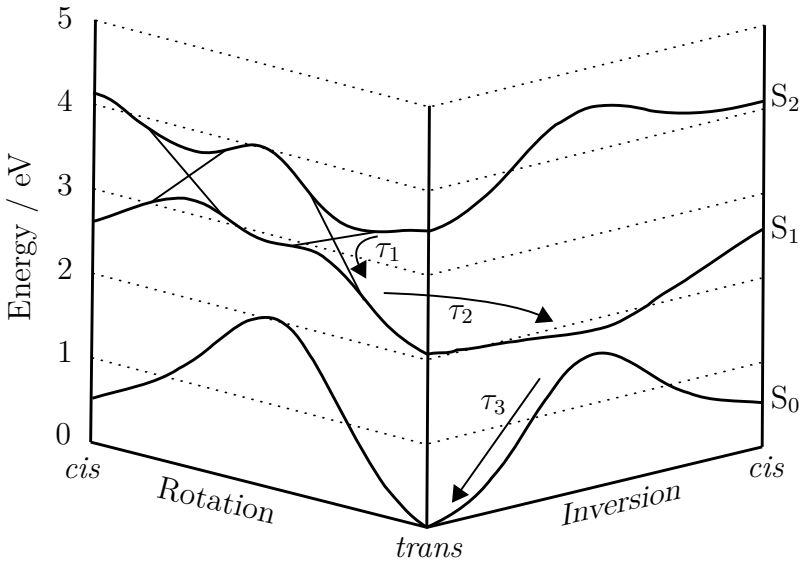


**Figure 3.7** Shows computational energy level for $S_1$, $S_2$, and ground state for isomerization via the rotation or inversion pathway. Arrows show the transition responsible for each lifetime; $\tau_1$ transition from $S_2$ to $S_1$, $\tau_2$ movement along the $S_1$ surface to conical intersection, $\tau_3$ relaxation to the thermal ground state.

the transition in the ground state, while red arrows show the transitions observed while thermal relaxation is occurring. This shows that during thermal relaxation lower energy transitions are observed, fitting with the PIA that overlaps with the GSB. The observation of this PIA that overlaps with the GSB and decays with the same lifetime, provides conclusive evidence that the longest lived decay is associated with the thermal relaxation on the ground state.

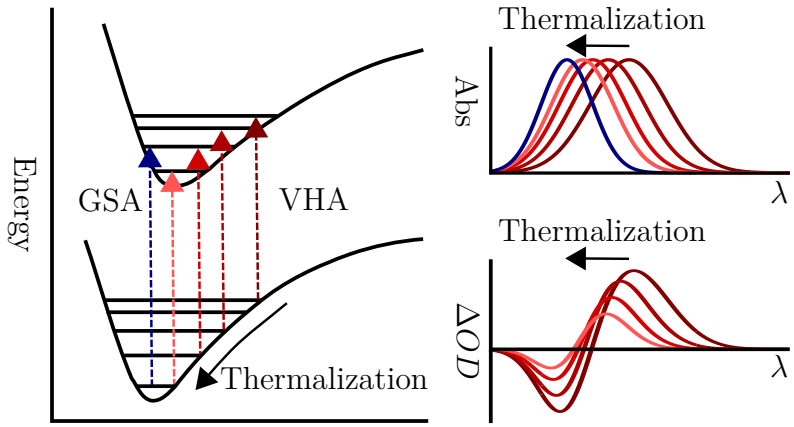


**Figure 3.8** Shows the electronic transitions associated with a molecule in its ground state (blue) (GSA) and while thermalization occurs (red), from vibronic hot states (VHA). This shows that as thermalization occurs a molecule will have additional absorption at lower energy than the ground state. This is shown on the right with absorption being assumed to be Gaussian shaped, the shift in the ground state leads to a transient signal that is positive at lower energy then the GSA.

The final feature that might be expected is a long lived PIA and GSB due to the generation of the *cis* isomer. This occurs due to the variation between the two

absorption spectra. The *trans* isomer has higher absorption between 270 – 350 nm and therefore photo–isomerization to the *cis* isomer results in a long lived GSB. The *cis* isomer has higher absorption between 400 – 570 nm resulting in a new PIA feature. These features are not observed in the data collected, due to the low molar extinction coefficient of both conformations between these wavelengths. Starting with the ideal 100% *trans*, excitation that generates a 10% *cis* species is calculated to give a $m\Delta OD$ signal of -0.2 $m\Delta OD$ at 320 nm and 0.01 $m\Delta OD$ at 430 nm. Even with these generous parameters the signal is below anything detectable, as the instrument background noise is 0.2 $m\Delta OD$ at 320 nm and 0.02 $m\Delta OD$ at 430 nm. This means that in spite of our instrument producing better quality data than other published results,[17] we are still unable to detect the long lived isomerization product for azobenzene.

### 3.5.1 Effect of Solvent

Figure 3.9 shows the TA surface and kinetic traces for azobenzene in tetrahydrofuran. The trace has the same features in acetonitrile, three PIA features and the GSB feature. The main difference is the contribution due to coherent artifacts at early time, resulting in a broad absorption with a lifetime of less than 200 fs. The other noticeable difference is the decrease in the intensity of the PIA at 470 nm, which becomes more of a shoulder rather that a distinct peak as seen in acetonitrile. This is obscured by the coherent artifact as it spreads over the 300 – 450 nm range.

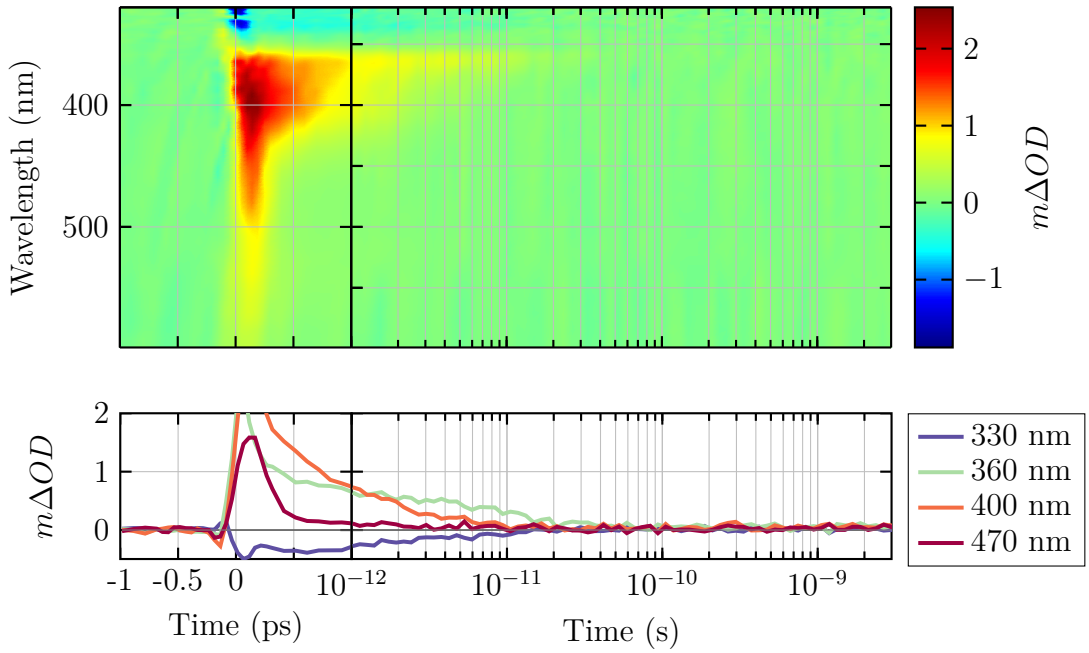


**Figure 3.9** TA surface for 1 $\mu M$ azobenzene in tetrahydrofuran with 300 nm excitation. *Top:* TA surface. *Bottom:* Kinetic traces at various wavelengths.

A comparison of the lifetimes can be seen in Table 3.1. They show little difference between acetonitrile and tetrahydrofuran. $\tau_2$ has a difference of 100 fs, showing relaxation of the $S_1$ surface is unchanged between the solvents. $\tau_3$ has a 4 ps difference with tetrahydrofuran occurring quicker. $\tau_3$ is attributed to the thermal relaxation of the *trans* species with branching having occurred earlier. The difference does not indicate a variation in yield or mechanisms between the two solvents.

**Table 3.1** Lifetimes for azobenzene in MeCN and THF

| **Solvent** | $\tau_1/ps$ | $\tau_2/ps$ | $\tau_3/ps$ |
|---|---|---|---|
| MeCN | >0.2 | 1.1 | 14 |
| THF | >0.2 | 1.0 | 10 |

This can also be seen by comparison of spectral slices in Figure 3.10, which are normalized by the earliest time slice. It can be seen that there is very little difference in decay kinetics between the solvents. In tetrahydrofuran a slightly higher and broader feature in each later time slice is observed, which is indicative of a slower decay. The slower decay is associated with $\tau_3$ while the 400 nm peak associated with $\tau_2$ has little difference between the 500 fs and 1.0 ps trace. This supports the small variation in $\tau_2$, 1.0 ps (MeCN), and 1.1 ps (THF).

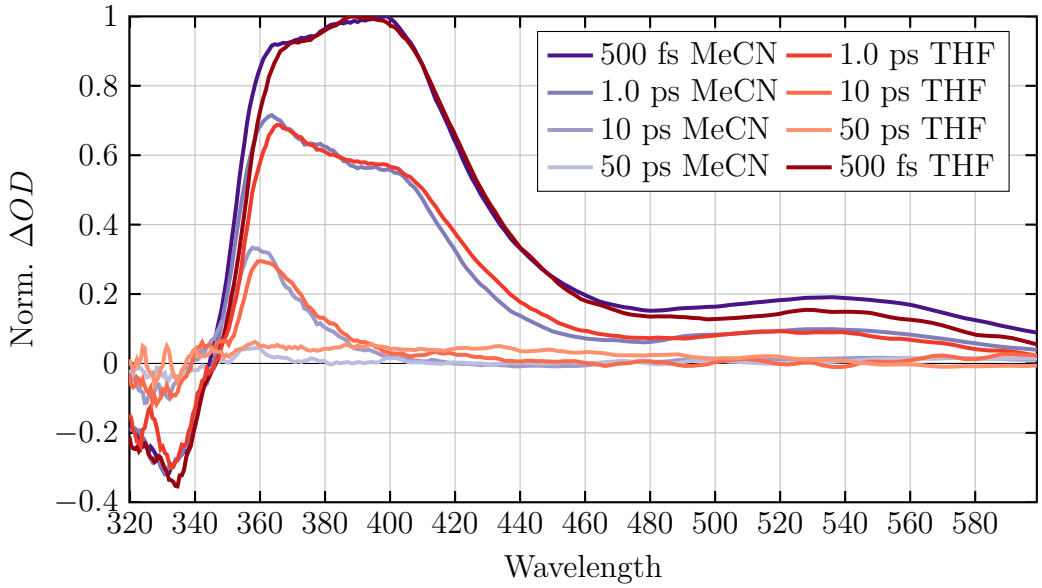


**Figure 3.10** Comparison between the spectral slices of 1 $\mu M$ azobenzene with 300 nm excitation in acetonitrile and tetrahydrofuran taken at 500 fs, 1.0 ps 10 ps and 50 ps.

## 3.6 Conclusion

Azobenzene is valuable in benchmarking and optimizing the TA setup. It contains femtosecond and picosecond dynamics with which to compare kinetics over a range

of timescales, and spectral features that span the 300 – 600 nm range with those reported in the literature.[17] We have been able to show that the detection window has been extended out to 320 nm, providing a clear picture of the decay of azobenzene after photo–excitation, including GSB.

The inclusion of UV wavelengths into the probe pulse and detection has allowed the GSB feature to be resolved and provides further support for the assignment of the final decay to thermalization in the ground state. It has allowed the observation of the final PIA overlapping with the GSB, which is characteristic of thermalization. Absorption from azobenzene in the vibrationally excited ground state has a bathochromic shift, leading to PIA that overlaps and extends to shorter wavelengths than the GSB.

The comparison between acetonitrile and tetrahydrofuran shows no noticeable change in the photophysics of isomerization between the two, with relaxation on the $S_1$ surface, 1.0 ps (acetonitrile) and 1.1 ps (tetrahydrofuran), occurring on a similar timescale. This provides a good reference for studies on the foldamer as changes induced can be attributed to the modifications made to the foldamer.

# Chapter 4

# Light–Controlled Capture and Release Foldamer Molecules

Light–controlled capture and release foldamer molecules are designed so that the release or capture of anions is controlled by irradiation of light. The absorption of light leads to a structural change inducing a change in affinity for a particular ion.[12] The term foldamer is derived from the nature of this change. Ion binding occurs via the folding, generally into a helix structure, around the ion.[12] While light control indicates how this change from random coil to helix is influenced (Figure 4.1).

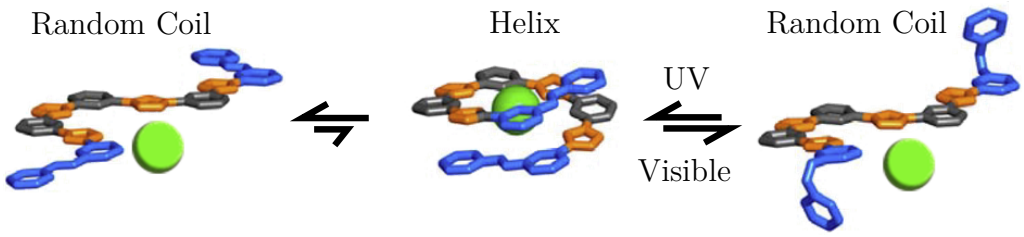


**Figure 4.1** Light–controlled binding is achieved by perturbing the random coil to helix equilibrium. This is achieved by controlling the geometry of the AB moiety making it either *cis* or *trans* isomer.[61]

The class of catch–and–release foldamers investigated were designed and synthesized by Dr. Amar Flood and co–workers, Figure 4.2.[12,61,62] The azobenzene (AB) moieties allows the foldamer to be light controlled. The conformation of the AB moiety effects the random coil to helix equilibrium.[12,63] As this is the crucial light control element, transient absorption (TA) spectroscopy was employed to explore the photophysics.

The light–induced dynamics of two related foldamers, termed foldamer 1 (F1) and foldamer 2 (F2), and the non–binding derivative of each, F1H and F2H, (Figure 4.2)

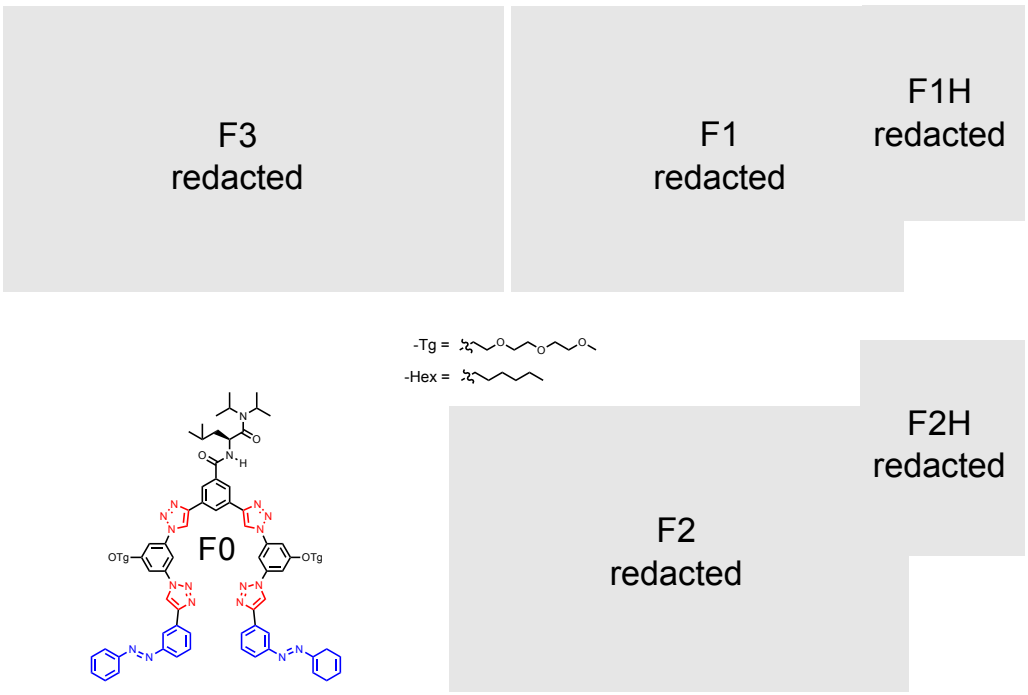


**Figure 4.2** Foldamer family designed and synthesized by Amar Flood and co–workers.[61]

were studied under conditions that affect the ability for photo–control of the capture and release of chloride ions.[61] Non–binding is achieved by removing one arm of the molecule, preventing folding and minimizing substituents change around the AB moiety.

It is possible to separate the effects of the AB photo–isomerization from the larger chloride capture and release rearrangement by comparing the effects that these conditions have on the photophysics (Section 4.3) and previously studied capture and release dynamics (Section 4.1). This allows greater understanding of how changing the AB moiety characteristics will influence the capture and release process.

## 4.1 Molecular Design

The foldamers were designed to incorporate triazole groups, $\pi$-conjugated system, hydrogen bonding capable units, and AB. The central design creates an electropositive pocket in the center with two arms controlled by AB.[61,63] The AB moiety allowed the foldamer to be used as a light–induced switch. When the AB under goes it's *trans* to *cis* isomerization it bringing the $\pi$-conjugated systems, and hydrogen bonding segments into closer proximity when in the *trans–trans* (*tt*) configuration, or separating these stabilizing interactions in the *cis–cis* (*cc*) or *trans–cis* (*tc*) conformations.[61,63,64]

Light controlled chloride capture and release is shown in Figure 4.3.[12,61,62] This shows the conductivity being modulated by light in the presence of the foldamers. As the chloride is bound by foldamer structure, there is a drop in conductivity. This also highlights how structural changes have a marked effect on the change in conductivity.[61]

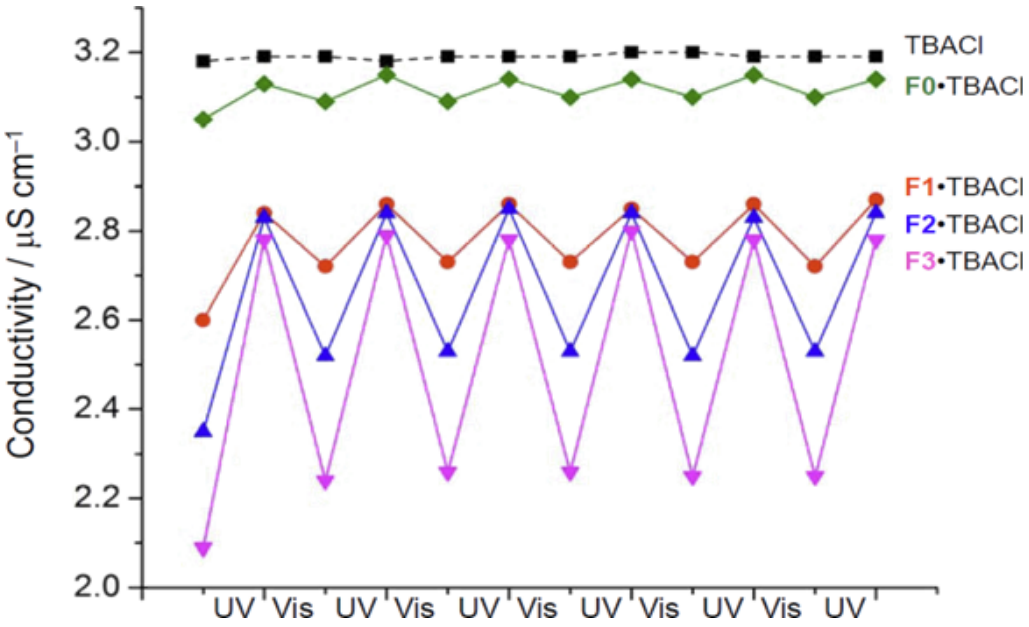


**Figure 4.3** Change in conductivity on exposure to UV and then visible light, indicating capture and release of chloride ions. Increased binding seen as we go up the foldamer numbering. Tetrabutylammonium chloride (TBACl) is the chloride ion source and is shown as a reference.[61]

The anion binding ability is incorporated through the use of triazole groups. These contain C–H $\cdots$ $Cl^-$ hydrogen bonding interactions, however it should be noted the C-H bond is not normally considered to have the potential to hydrogen bond. The incorporation of an $\alpha$–nitrogen and the $\beta$–$\pi$–system provides sufficient electron withdrawal to polarize the C–H bond.[65–69] To maximize the stabilizing effect the triazol groups are arranged to create an electropositive pocket, to stabilize the anionic charge.[61,62,64] The formation of this pocket is the favoured conformation for the capture of chlorine. By manipulating the pre–chloride conformation to be close to the ideal pocket the reorganization energy can be minimized. This reduction in reorganization energy encourages the binding of chloride.[61,64]

The *tt* form has favorable $\pi$–$\pi$ interactions in the helix conformation (Figure 4.1). The triazole C–H bonds are interior in the helix conformation creating an electropositive pocket similar to the favored conformation when chloride ion is bound. When AB is in its *cis* isomer there is a random conformation and the C–H of the triazole are pointing in random directions, requiring a greater conformational change to stabilize chloride ion.

The foldamer series has increasing chloride ion binding strength from F1 to F2 as seen in Figure 4.4. This is attributed to the stabilization of the helix which is the preferred conformation for chloride binding, thereby increasing the chloride binding constant.[61]

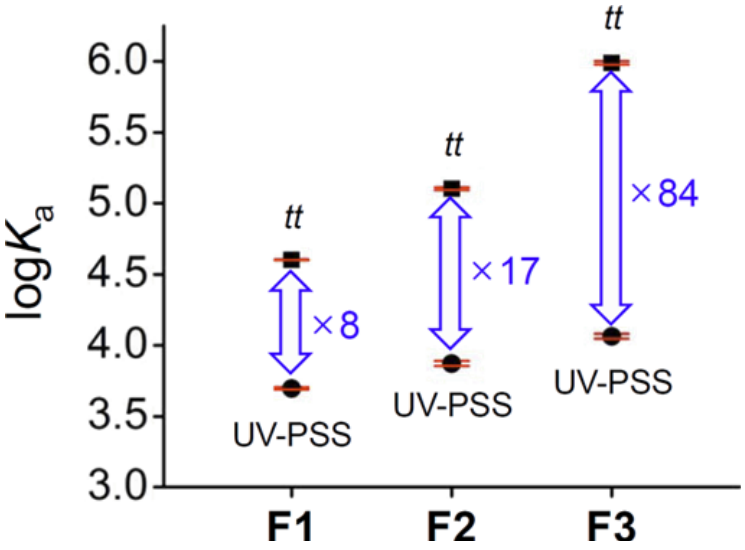


**Figure 4.4** By differing degrees of $\pi$–$\pi$ interactions and H–bonding the binding constant in both *tt* and UV–PSS (UV photostationary state) can be altered. The increase in $\pi$–$\pi$ interactions or H–bonding increases the contrast in binding constants between *tt* and UV–PSS.[61]

The increased affinity towards the helix conformation is due to an increase in favorable $\pi$–$\pi$ stacking, from two units to four units when going from F1 to F2. The increase from F2 to F3 is due to the incorporation of an amino acid moiety, which has the ability to form hydrogen bonds when in the folded conformation, stabilizing the helix structure and locking it in this form.[61]

## 4.2 Chloride Ion and Solvent Effect on Helicity

The conformation is not only affected by the *tt*, *cc*, and *tc* AB conformations, but by the presence of chloride ions in solution. NMR spectroscopy studies have shown broad peaks even after exposure to visible light (that produces the helix favoring conformation).[61] This suggests that there is still conformational flux even when AB moieties are mostly *tt*. Upon addition of chloride ions the broad resonances narrow, see Figure 4.5, indicating that the chloride ion stabilizes the foldamers' conformation.[61,63]

Solvophobicity is the driving force towards the helix conformation, as the helix maximizes favorable $\pi$–$\pi$ interactions, thus minimizing solvent–$\pi$ interaction.[61,63] The other important solvent effect on the system is the solvent affinity to the chloride

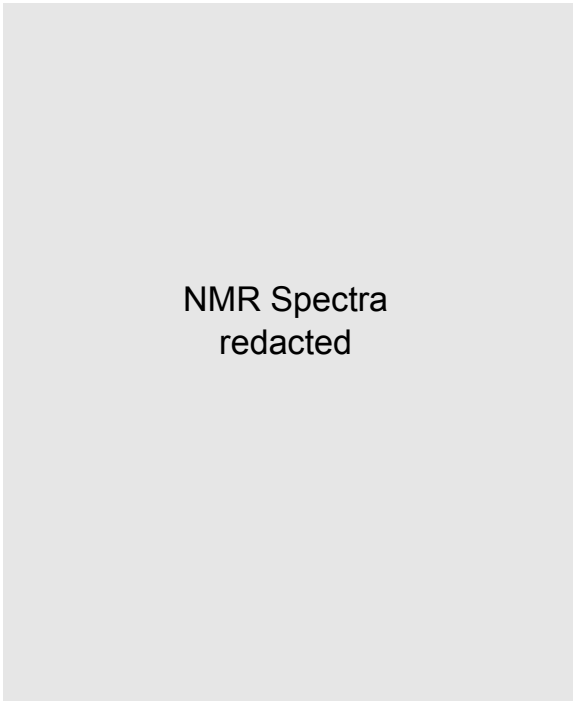


**Figure 4.5** Increasing peak sharpness as chloride addition favors the helix conformation. The peak sharpening results as there is less conformation flux once the foldamer is locked into its helical form.[61]

ion. In order to bind chloride ions the foldamer must have a higher affinity than the solvent. To produce a capture and release effect there must be a large change in binding affinity after exposure to UV or visible light. This allows the foldamer to capture the chlorine ions in the *tt* form, whilst allowing the release of chloride ions when in *cc* form.[12,64]

## 4.3 Transient Absorption Spectroscopy

To investigate the photophysics involved for the foldamer family F1, F2 and their halves (F1H and F2H) were provided by Flood *et al.* To separate the effects related to chloride ion binding and the formation of the fully folded structure, F1H and F2H were also studied (Figure 4.2). With the four foldamer compounds, together with AB, it is possible to see if the macro–structure of the foldamer affects the isomerization of AB. Furthermore, time–resolved studies may also provide information on the timescales which chloride ions are captured and released.

### 4.3.1 Structural Effects

Recalling from Chapter 3, the TA surface of AB comprises of three photo–induced absorption (PIA) features, corresponding to the relaxation on the $S_2$, $S_1$, and ground state potential energy surfaces (PES), and a ground state bleach (GSB). Figure 4.6 shows the TA surface, kinetic and spectral traces for F1. F1 has three PIA signatures and a GSB, the same number as AB. The GSB can be seen in the kinetic trace at 330 nm and decays with a lifetime similar to the longest lived PIA at 430 nm. The three PIA features are located at ~380 nm, 420 nm, and 550 nm. The absorption feature at ~380 nm overlaps with both the GSB and PIA at 420 nm, observable through the appearance of a shoulder at 400 fs and 1.0 ps, with it having a more prominent peak at 0 fs and 10 ps. The feature at 550 nm is broad, and has decayed within 10 ps. The sharp dip at 342 nm in the 0 fs trace can be attributed to stimulated Raman amplification, discussed previously.

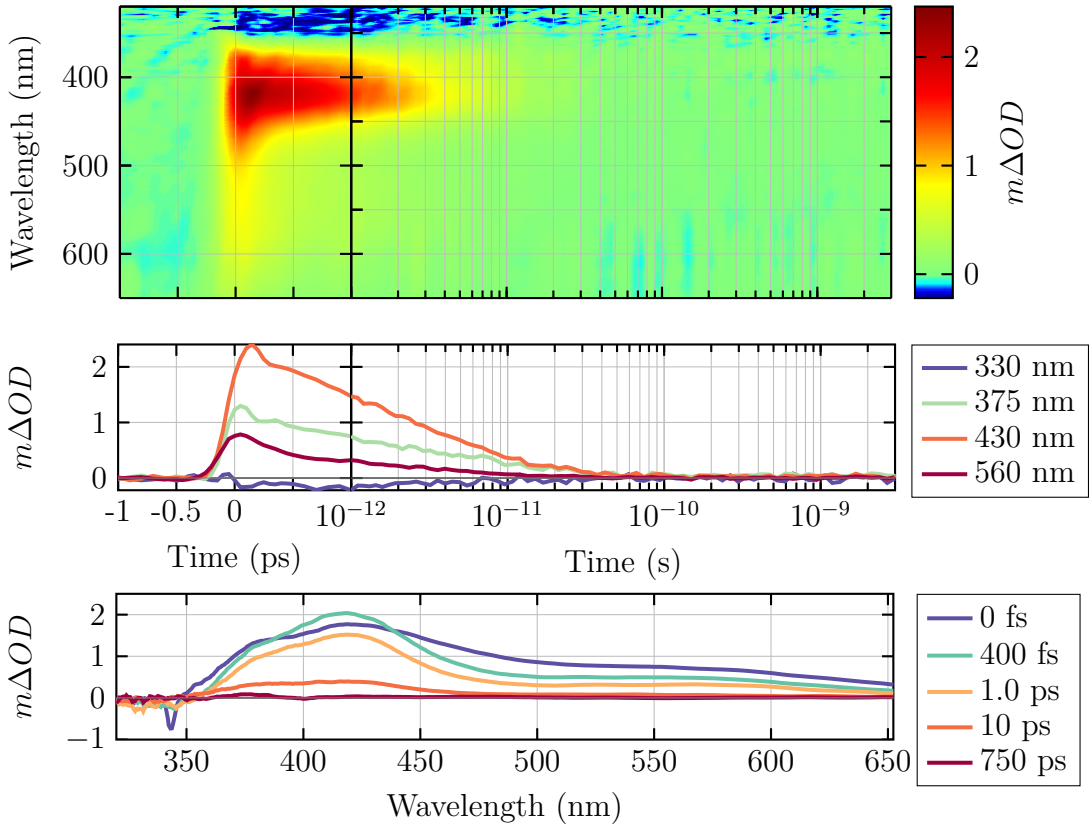


**Figure 4.6** TA data for F1 1 $\mu$M in acetonitrile (MeCN) with 300 nm excitation. *Top:* TA surface. *Middle:* Kinetic traces. *Bottom:* Spectral slices.

### F1 and Azobenzene

Comparing the TA surfaces of AB and F1, Figure 4.7 illustrates the difference between the two species. The central PIA at 420 nm has a lifetime similar to the PIA at ~380 nm for the F1, whereas in AB they are distinctly different. The other difference is the intensity of the GSB with AB being much stronger.

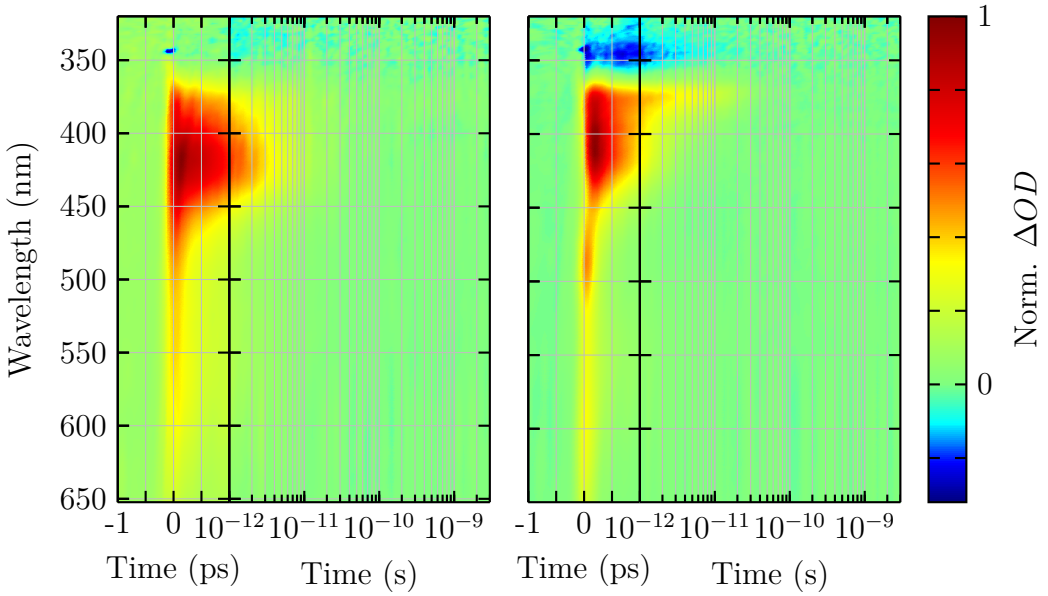


**Figure 4.7** *Left:* TA surface of F0.5 $\mu M$ F1 in MeCN with 300 nm excitation. *Right:* TA surface of 1 $\mu M$ AB collected in MeCN with 300 nm excitation. Comparison between the TA surface of AB and F1 showing the lengthening of decay rates with similar features.

Figure 4.8 also presents a closer look at the spectral shapes at various time delays; 250 fs, 400 fs, 1.0 ps, 50 ps, and 0.75 ns. Overall there is a bathochromic shift for the F1 peak at 420 nm, with the of the GSB being the same wavelength for both AB and F1. The broad absorption at longer wavelengths is present for both, but F1 is missing the PIA at 470 nm seen in the 250 fs AB trace. This peak was assigned to relaxation on the $S_2$ PES for AB. The absence of this could be caused by the broadening of both peaks as the F1 feature at 420 nm now has a broad shoulder at longer wavelengths. The relaxation of this red edge is slowed with F1 taking 1.0 ps for this band to decay, compared with 400 fs for AB. This slowing in decay is also seen when comparing the PIA at 420 nm, which is attributed to relaxation and branching on the $S_1$ PES, with absorption still being present after 1.0 ps. The feature overlapping with the GSB, has a decreased relative amplitude when compared with the 420 nm peak, this feature is assigned to vibrational cooling to the ground state.[17,59] This decreased amplitude suggests there is a lower yield to vibrationally excited electronic ground states, with the greater time spent on the $S_1$ PES resulting in a conformation that closely resembles the *trans* isomer's ground state.

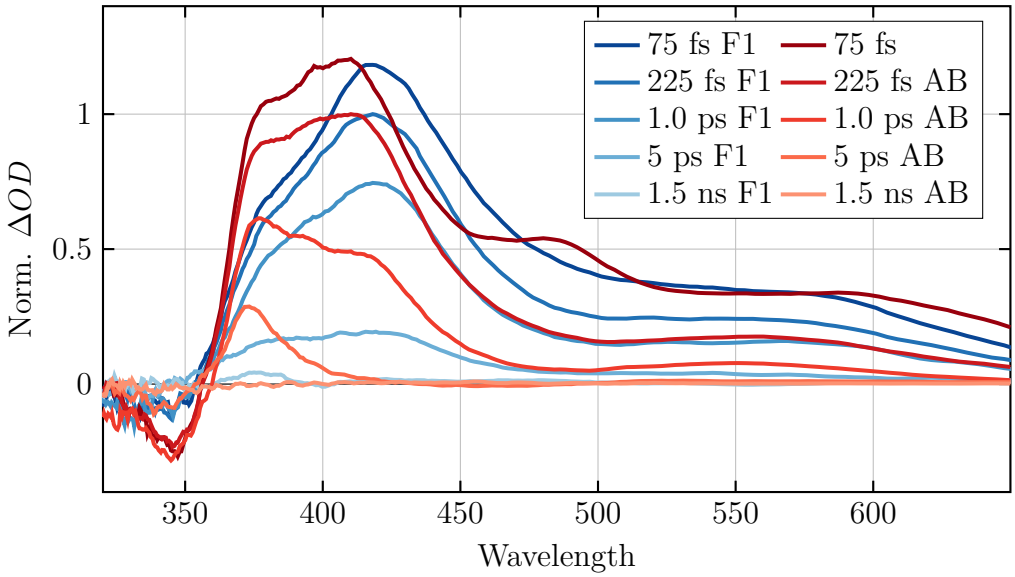


**Figure 4.8** Comparison of spectral slices for 0.5 $\mu M$ F1 and 1 $\mu M$ AB both collected in MeCN with 300 nm excitation. Darker traces indicate earlier times.

Global fitting was used to determine the underlying lifetimes, discussed in Section 2.3.4. It was found that four lifetimes were needed for an adequate fit, which are compared with those for AB in Table 4.1. The initial lifetime is within the instrument response function (IRF), and so any difference from AB are not resolved. $\tau_2$ is associated with relaxation on the $S_1$ PES and has increased for F1, from 1.1 ps in AB to 1.7 ps. This is expected from inspection of the TA surface. $\tau_3$ corresponds to the thermalization into the electronic ground state and is similar for both F1 (15 ps) and AB (14 ps). There is an additional lifetime needed for F1 and the rest of the foldamer family, with the decay time being outside the time domain of these measurements. Assignment of this additional state was not possible with the current work, and is being followed up.

**Table 4.1** Fitted lifetimes for F1 and azobenzene

| **Compound** | $\tau_1$ / ps | $\tau_2$ / ps | $\tau_3$ / ps | $\tau_4$ / ns |
|---|---|---|---|---|
| F1 | >0.2 | 1.7 | 15 | < 3 |
| AB | >0.2 | 1.1 | 14 | |

The main difference for F1 when compared with AB is the increase in the $\tau_2$ lifetime and the appearance of a new decay component. The DAS for AB and F1 can also be compared. In this case a model to transform the DAS to SAS adds unnecessary complications and assumptions. This is due to the effect that branching on the $S_1$ PES will have on the re–weighting of the DAS, as both AB and F1 will decay via similar pathways the direct comparison of the DAS is appropriate.

Figure 4.9 shows the DAS for both F1 and AB. DAS1 contains the peak associated

with the relaxation from $S_2$ to $S_1$. This component was not observed on the TA surface for F1, and was only resolved using global fitting. DAS2 looks similar for both compounds, with the notable exception of a positive shoulder spanning from 500 nm to 600 nm, observed for F1. There is a peak at ~420 nm for both AB and F1, supporting the assignment of this $\tau_2$ to relaxation and branching on the $S_1$ PES. DAS3 was associated with the thermalization to the electronic ground state for AB, and the similarity of lifetimes supports the same assignment for F1. The spectral shape observed does not conflict with this assignment, because a broader shape for F1 then could represent the greater number of vibrational modes available to the larger F1 molecule.

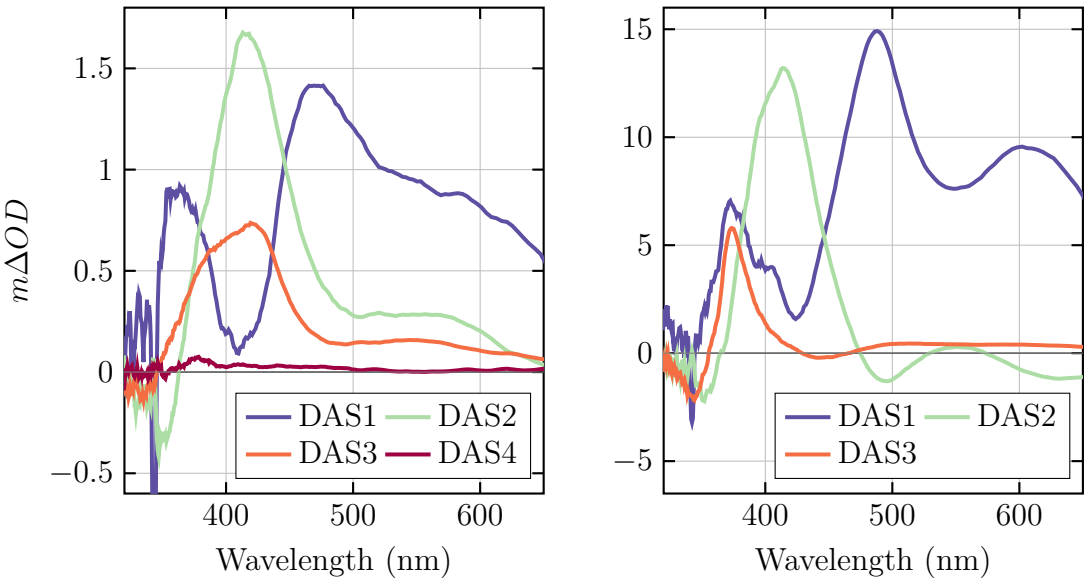


**Figure 4.9** Comparison of the DAS of F1 (*left*) and AB (*right*).

The comparison of F1 with AB in figure Figure 4.9 shows that the only significant difference is the in the lifetime attributed to relaxation and branching on the $S_1$ PES, and the additional nanosecond lifetime. The relaxation from $S_2$ to $S_1$ was observed via global fitting with the lifetime within the IRF. With evidence for thermalization on a time scale of tens of picoseconds as seen in AB.

### F1 and F1H

AB is not the ideal reference compound in a study of the photoisomerization of these foldamers because the substituents on F1 could have an electronic effect in addition to steric effects. To confirm that the behaviour seen is due to the AB moiety, F1H is compared with F1. F1H contains one AB moiety, which is attached to one–half of the overall F1 molecule. This gives a molecule that has similar electronic

effects on the AB moiety in F1 without as much steric bulk. Figure 4.10 contains spectral slices from F1 overlaid with those from F1H. The same features as in F1 are observed; a GSB and three PIA spectral features signatures. The PIA at ~380 nm overlapping with GSB and the PIA at 420 nm, can be attributed to thermalization in the electronic ground state. This PIA has a greater amplitude in F1H than F1, making F1H more similar to AB in this regard. The PIA at 420 nm corresponds to relaxation and branching on the $S_1$ PES and the broad absorption edge is associated with the $S_2$ to $S_1$ transition.

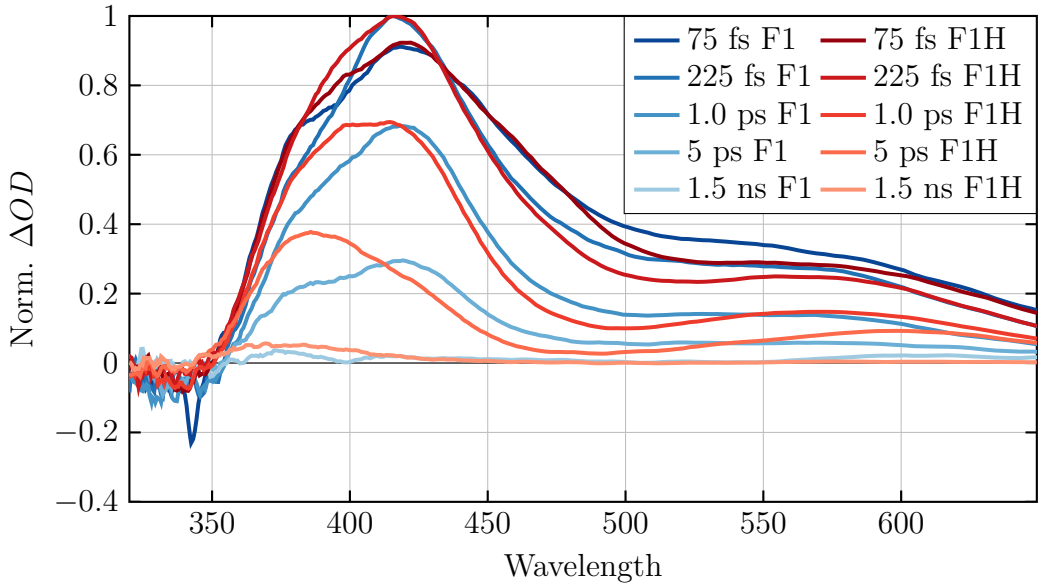


**Figure 4.10** Comparison of spectral slices for 0.5 $\mu M$ F1 and 1 $\mu M$ F1H both collected in MeCN with 300 nm excitation. Darker traces indicate earlier times.

The assignment of these states is supported by global fitting using four lifetimes, with the DAS (Figure 4.11) matching well with the features seen in the F1 DAS. Differences are apparent in the shape profiles of DAS3 corresponding to thermalization in the electronic ground state. For F1H, DAS3 is located next to the GSB, this is similar to AB thereby supporting the assignment of F1H DAS3 to thermalization. This is in contrast to F1 DAS3, which is much broader and contains a peak that is the same as DAS2.

The difference can be explained in terms of the relaxation on the $S_1$ PES and the rate of thermalization. Figure 4.12 shows the observed relaxations and order in which they occur on an illustrative PES. The $S_1$ PES has two sequential decays observed; branching, and relaxation. If we consider $\tau_3$ (relaxation) to occur faster than $\tau_2$ (branching) then the spectral feature attributed to $S_1$ will appear to decay as a single exponential, as there is no growth of the $\tau_3$ state. This would make DAS2 look like the $S_1$ state signature, as is the case with AB, F1 and F1H, and DAS3 resembles the thermalization signature as is seen for AB and F1H. For the case with

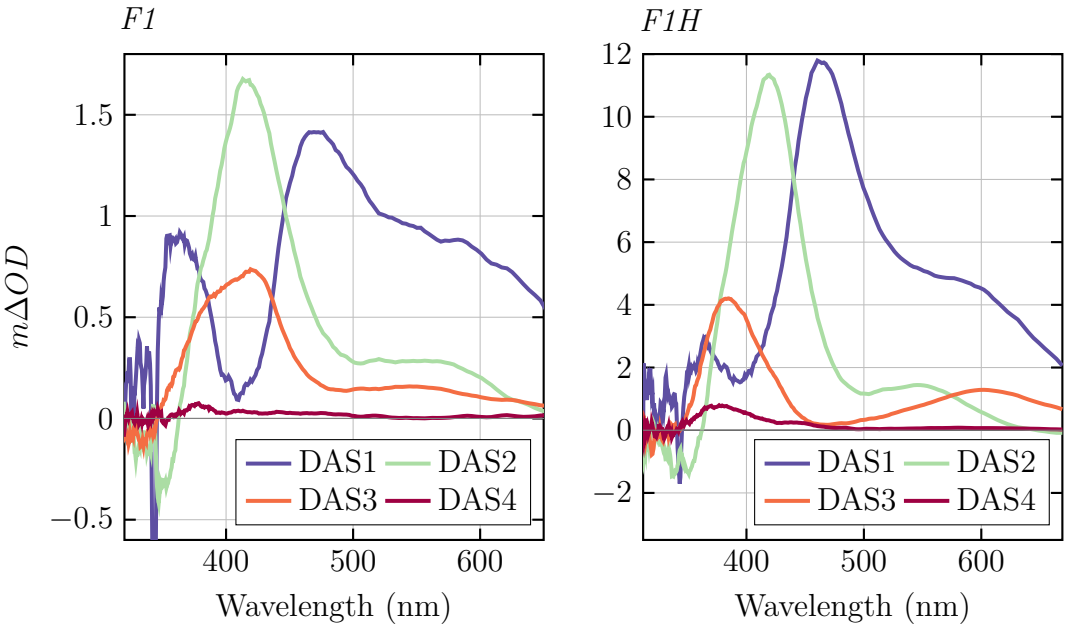


**Figure 4.11** Comparison of the DAS of F1 (*left*) and F1H (*right*).

F1, DAS3 is the sum of $S_1$ and thermalization spectral signatures and indicates that $\tau_3$ (relaxation) and $\tau_4$ (thermalization) are on similar timescales and so there is a build up in the relaxation state making $S_1$ signature decay bi–exponentially. The last case, observed for F2 and F2H, is when $\tau_3$ (relaxation) is longer that $\tau_4$ (thermalization).In this case DAS2 and DAS3 will closely resemble each other as there is overlap of $S_1$ and thermalization signatures in DAS3. This is because there is no population build up in the vibrational hot electronic ground state.

The difference in shape of DAS2 and DAS3 the result of the addition of the $S_1$ decay and thermalization to the ground state spectral features, this gives the branching lifetime of 1.7 ps and a relaxation of 14.8 ps for F1. In contrast F1H branching and relaxation occurs on a similar timescale, and can be well fitted to a single exponential decay of 2.5 ps.

### F1 and F2

Figure 4.13 shows spectral slices for F1 and F2. It can be seen that the features are similar between the two, with a GSB at wavelengths less than 350 nm, and a PIA at 420 nm, and a broad shoulder at 500 nm. There are two differences between F1 and F2. The absence of a shoulder for the PIA at 420 nm, which has been assigned to thermalization in AB for F1, and the difference in lifetime of the PIA at 420 nm, 25 ps in F2 and 15 ps in F1.

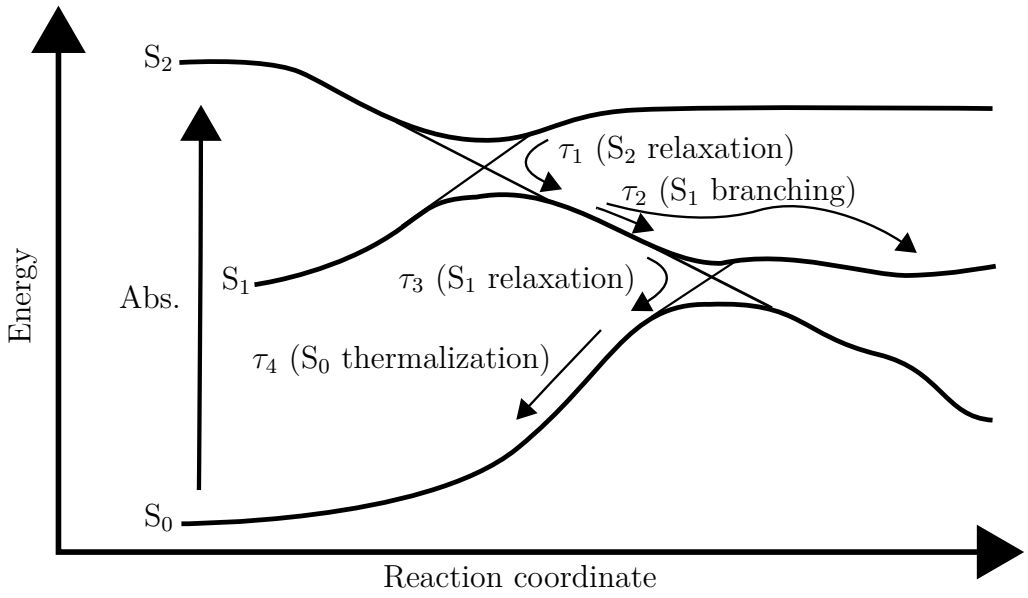


**Figure 4.12** An illustrative potential energy surface, showing the order of each decay. Relaxation of the $S_2$ then branching on the $S_1$ with the observable branch continuing to the $S_1$ to $S_2$ conical intersection, with relaxation lifetime given as $\tau_3$, finally thermalization to the electronic ground state

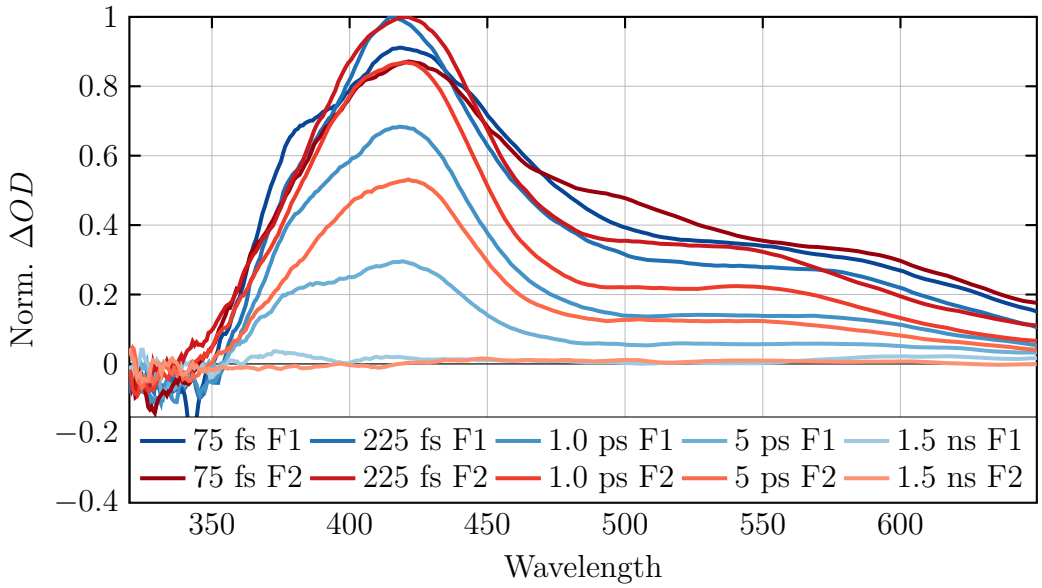


**Figure 4.13** Comparison of spectral slices for 0.5 $\mu M$ F1 and 0.5 $\mu M$ F2 both collected in MeCN with 300 nm excitation. Darker traces indicate earlier times.

Whilst the differences noted from visual interpretation of F1 and F2 are important, the DAS provides evidence for the assignment of each state. Figure 4.14 is a comparison of the DAS for F1 and F2. DAS2 and DAS3 do not show any differences between F1 and F2, however the spectral shape of DAS3 is important. The shape of DAS3 resembles DAS2, indicating that the lifetimes relate to the same species. The bi–exponential decay of the $S_1$ state is due to *cis–trans* branching and relaxation. This peak does not have a shoulder as seen in F1, as it is not convoluted

with thermalization. This gives the lifetime of branching on the $S_1$ PES (4.5 ps), and relaxation from $S_1$ to $S_2$ (25 ps).

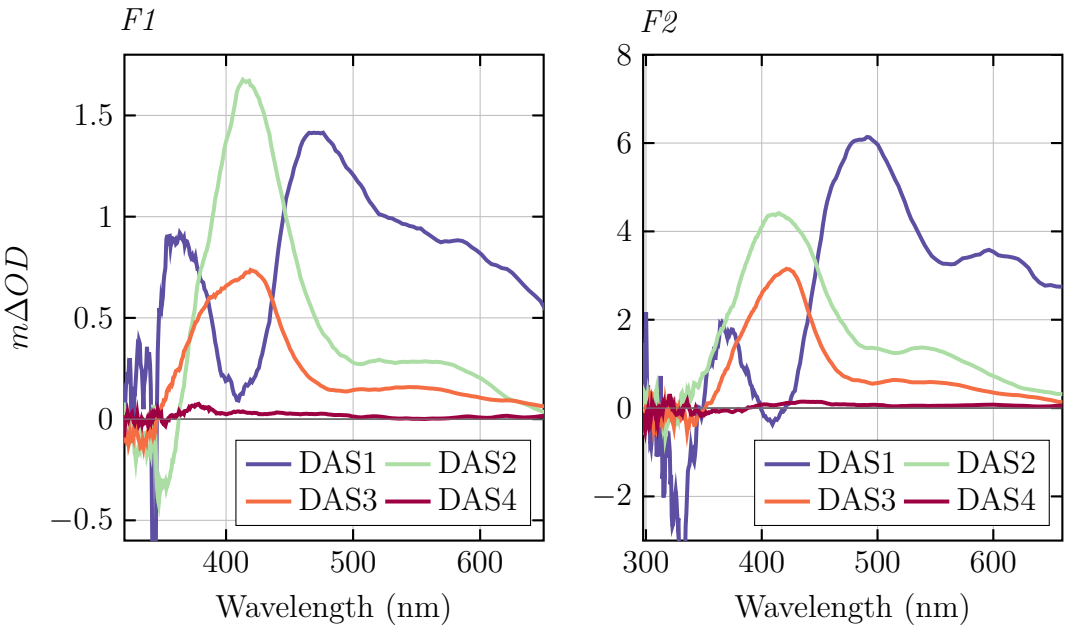


**Figure 4.14** Comparison of the DAS of F1 (*left*) and F2 (*right*).

### F2 and F2H

Figure 4.15 shows that there is no substantial difference in the spectral shape for F2 and F2H. However, differences are apparent in the lifetimes of the decay, with F2H having a shorter lifetime than F2. The lifetime of $\tau_1$ is within the IRF (<200 fs), consistent with the other members in the family of compounds. Branching of the $S_1$ state given by $\tau_2$ is 2.6 ps compared with 4.2 ps for F2, relaxation of the $S_1$ ($\tau_3$) happens in 18 ps in F2H and 25 ps in F2. These changes in lifetimes are reflected in the spectra with F2H having lower intensity but similar shape to F2.

The DAS shown in Figure 4.16 are consistent with the spectral slices (Figure 4.15). DAS1 and DAS2 for F2H are similar to the rest of the foldamer family. With DAS3 resembling the shape of DAS2, this shows that the decay on the $S_1$ PES occurs with two rates as in F2, branching on 2.6 ps and relaxation on 18 ps. As with F2, F2H DAS3 does not have shoulder that is associated with thermalization on the electronic ground state, suggesting that this occurs at a rate less that 18 ps.

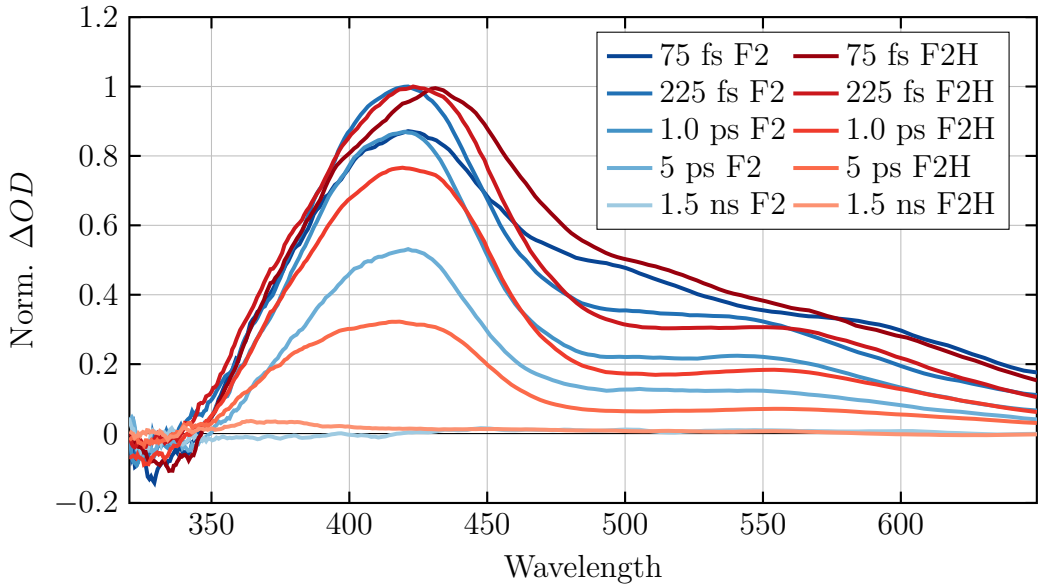


**Figure 4.15** Comparison of spectral slices for 0.5 $\mu M$ F2 and 1 $\mu M$ F2H both collected in MeCN with 300 nm excitation. Darker traces indicate earlier times.

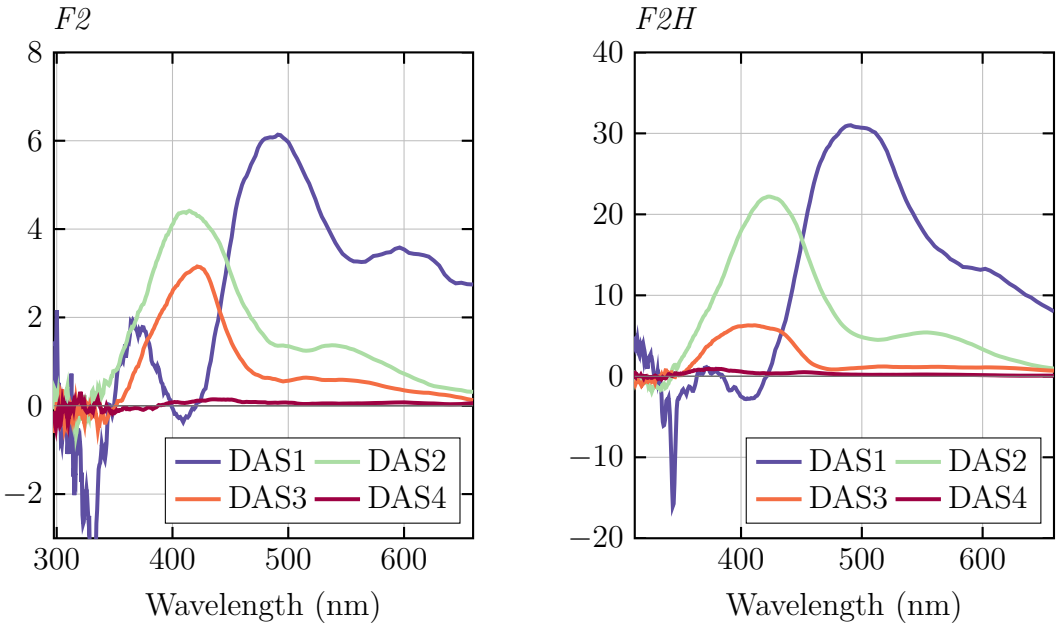


**Figure 4.16** Comparison of the DAS of F2 (*left*) and F2H (*right*).

### Summary of Structural Effects

The comparison of different structures in the foldamer family has identified the major difference between the foldamer and AB being the relaxation and branching times on the $S_1$ surface. Figure 4.17 has a comparison of the DAS2 and DAS3. DAS2 corresponds to the faster lifetime associated with the $S_1$ surface. For AB, this has been assigned to both the branching on the $S_1$ PES to give *cis* and *trans* isomers, and the relaxation of the $S_1$ to $S_0$. This has the same spectral shape for all members of the foldamer family and AB, supporting the assignment of this lifetime to a pathway on the $S_1$ state for all foldamers. When looking at DAS3 (the ~15 ps component) we can see a progression of DAS shapes from that seen in AB to one that looks very similar to DAS2. For the species where DAS3 and DAS2 look the same they can be assigned to the same surface, in this case the $S_1$. DAS3 is caused by thermalization in the electronic ground state as in AB, the relaxation on the $S_1$ PES through the $S_1$ to $S_0$ conical intersection, or a mixture of the two.

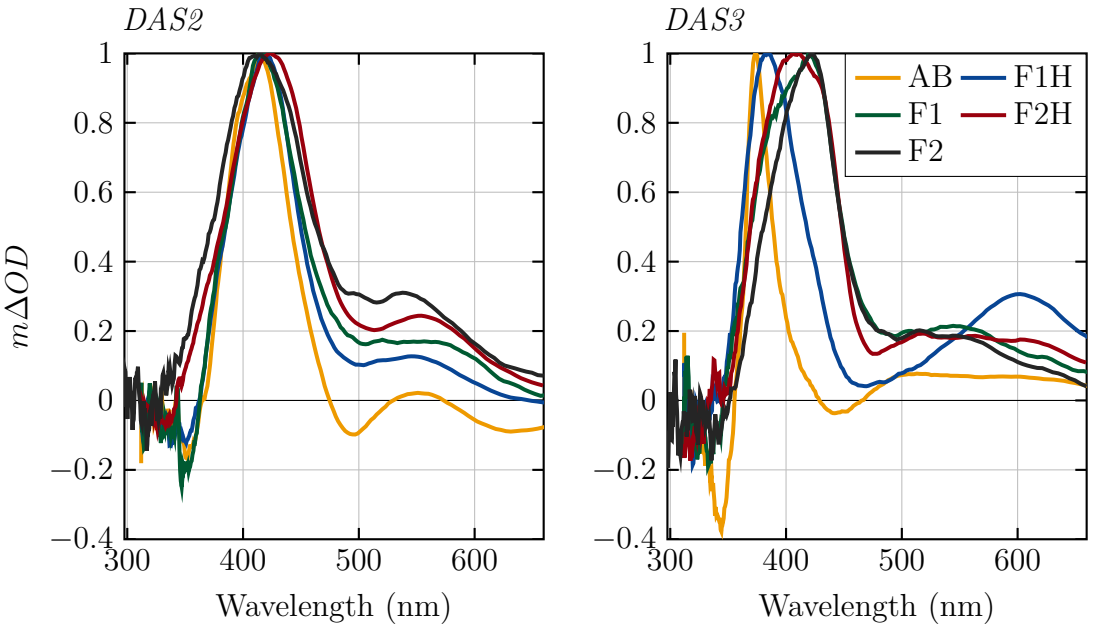


**Figure 4.17** The DAS2 (left) and DAS3 (right) for each member of the foldamer family studied. DAS2 overlaps well across the family while there is a bathochromic shift observed in DAS3.

For the foldamer family, Table 4.2 shows the rates and decay pathways that have been attributed to the DAS. This shows that through the progression from AB → F1H → F1 → F2H → F2H, i.e. increasing substitution of the AB moiety, there is an increasing of $S_1$ branching and relaxation lifetime.

**Table 4.2** Foldamer lifetimes associated with decay steps

| **Solvent** | $S_2 \rightarrow S_1$ / ps | $S_1$ branch / ps | $S_1$ relax / ps | vib. cool/ ps |
|---|---|---|---|---|
| AB | >0.2 | 1.1 | (>1.1) | 14 |
| F1H | >0.2 | 2.7 | (>2.7) | 31 |
| F1 | >0.2 | 1.7 | 15 | (<15) |
| F2H | >0.2 | 2.6 | 18 | (<18) |
| F2 | >0.2 | 4.2 | 25 | |

### 4.3.2 Solvent Effects

As the chloride ions binding affinity is dependent on solvent; it has been shown that by increasing the polarity of the solvent mixture favors the formation of the helical form of the foldamer.[61] The TA features were investigated by varying the mole fraction of the between MeCN and tetrahydrofuran (THF) solvent mixture. This showed the lifetimes identified were unaffected by changes in the propensity towards the helix conformation for F1, but some dependance is observed for F2.

#### F1

The comparison of F1 in MeCN and THF shows no discernible differences. Figure 4.18 shows spectra slices overlaid for the two species at different times. The variation is at 225 fs, and is attributed due to the presence of two photon absorption (TPA) in THF and not MeCN.

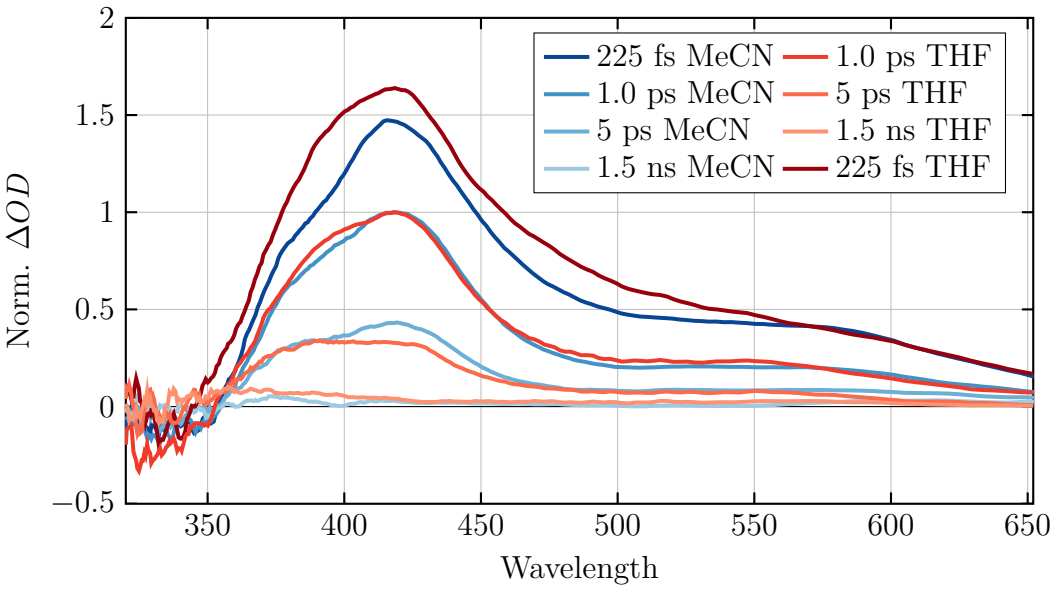


**Figure 4.18** Comparison of spectral slices of 0.5 $\mu M$ F1 with 300 nm excitation in both MeCN and THF. Darker traces indicate earlier times.

The small variation in spectral shape is supported through global fitting which also showed small variations in lifetimes. In THF $\tau_2$ is 2.1 ps and in MeCN it is 1.7 ps, $\tau_3$ is 12 ps for THF and 15 ps for MeCN, this shows a increase in THF for $\tau_2$ but a decrease for $\tau_3$. To investigate if this effect is due to helix formation, a comparison is made to F1H in Table 4.3. This shows the same trend is observed across both F1 and F1H, which indicates solvent effects rather than tertiary structural helical effects of the foldamer are being observed.

**Table 4.3** Comparison of F1 and F1H lifetimes

| **Solvent** | $\tau_2$ F1 / ps | $\tau_2$ F1H / ps | $\tau_3$ F1 / ps | $\tau_3$ F1H / ps |
|---|---|---|---|---|
| MeCN | 1.7 | 2.7 | 15 | 39 |
| 50:50 | 1.5 | 1.9 | 8.7 | 31 |
| THF | 2.2 | 3.1 | 12 | 24 |

**F2**

The solvent effect for F2 is more pronounced than F1, illustrated in Figure 4.19, whereby a difference in spectral features at 5 ps and MeCN and THF is observed. For THF there is the appearance of a side band at 380 nm and a lowering of the peak intensity at 420 nm when compared with MeCN. In a 1:1 mixture of MeCN:THF (Figure 4.19) there is a good match between spectral features for MeCN and the 1:1 mixture.

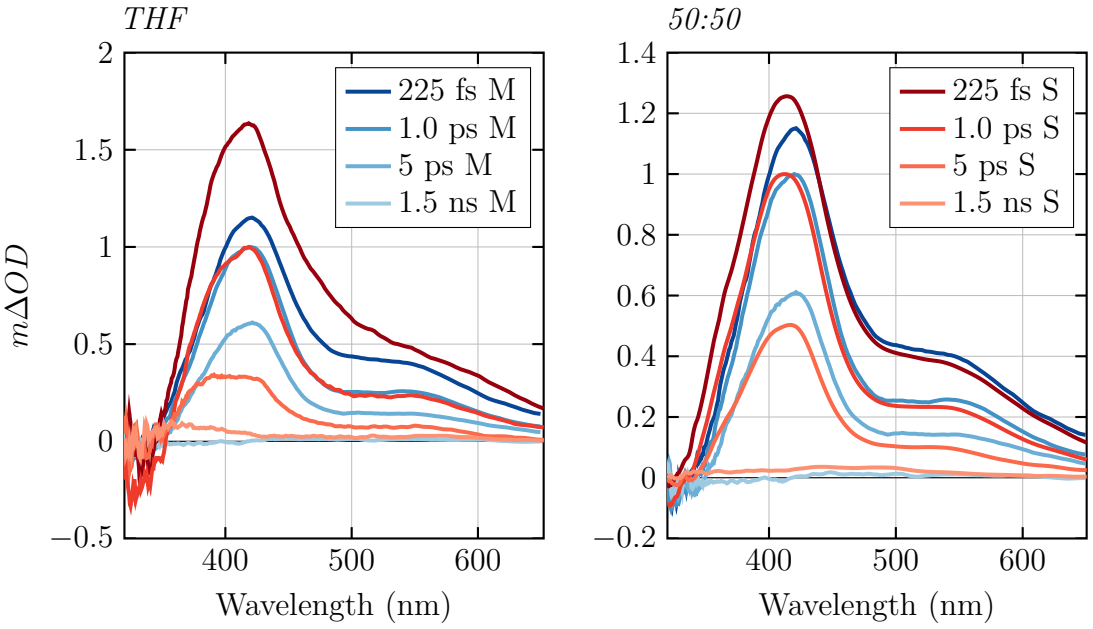


**Figure 4.19** Comparison of F1 in; MeCN, THF, and 1:1 MeCN:THF. Darker traces indicate earlier times. *Left:* Has MeCN compared with THF. *Right:* has MeCN compared with 1:1 mixture. $M(blue) = MeCN$, $S(red) = other\ solvent$.

This additional PIA signature can be seen in Figure 4.20, it resembles the thermal

relaxation seen in AB and F1H appearing on the edge of the GSB. The PIA signature at 380 nm is lacking in F2H (Figure 4.20) indicating it is the result of either helical formation or larger structure. As helical formation is favored in MeCN (compared to THF), the observed difference is attributed to a structural change. The larger structure is well solvated in THF leading to a random–coil arrangement. Due to the close proximity of the intramolecular $\pi$–conjugated groups and the structural flexibility it is expected that there will be interaction between the two $\pi$–conjugated systems. This results in more structural hindrance and a longer thermalization period. This is not observed for F2H or F1 due to the molecular design of each compound. F2H lacks the additional $\pi$–conjugated group on the other arm, and F1 lacks the extended conjugation when compared to F2. This effect is also lacking in MeCN as the polar solvent will favor the more structured helical form which exhibits no thermalization signature in any of the helix forming foldamers studied (F1 and F2).

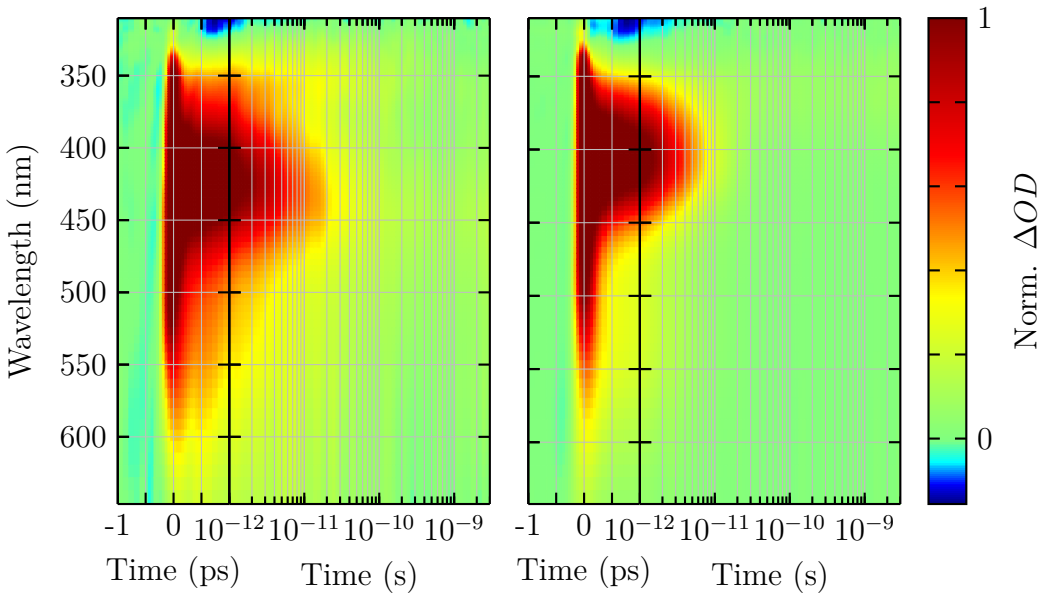


**Figure 4.20** *Left:* TA surface of 0.5 $\mu M$ F2 collected in THF with 300 nm excitation. *Right:* TA surface of 1 $\mu M$ F2H collected in THF with 300 nm excitation. The comparison highlights the additional decay in F2 located at ~360 nm.

### 4.3.3 Chloride Ion Effects

It has been shown by Amar Flood *et al.* that the addition of chloride ions to the system will favour the formation of the helical conformation.[61] The triazole groups prefer to be orientated with the C–H bond towards the chloride. A 1:1 MeCN:THF mixture was used as the solvent system, this was chosen as there is supporting data to show that capture and release of chloride ions occurs in this solvent mixture.[61]

Figure 4.21 shows the spectral slices of F1 with no chloride ions present and ten equivalents of chloride ions. The earliest time slice (darkest shade on figure) for F1 without chloride ions has an TPA artifact from THF which accounts for the observed different between F1 with and without chloride. The other spectral traces overlap well, showing there is no difference with or without chloride ions added.

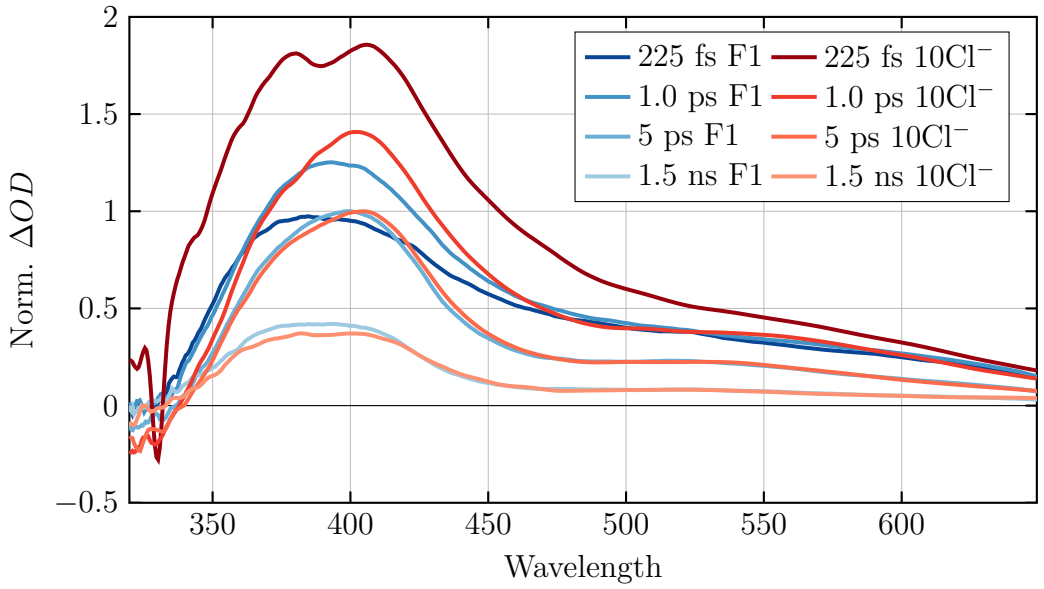


**Figure 4.21** Comparison of spectral slices for 1 $\mu M$ F1 in MeCN with 300nm excitation with and without ten equivalents of chloride. Darker traces indicate earlier times.

Figure 4.22 shows spectral slices for F2 without chloride ions and with ten equivalents of chloride ions added. Similarly to F1 the F2 traces overlap well, suggesting there is little change upon addition of chloride ions.

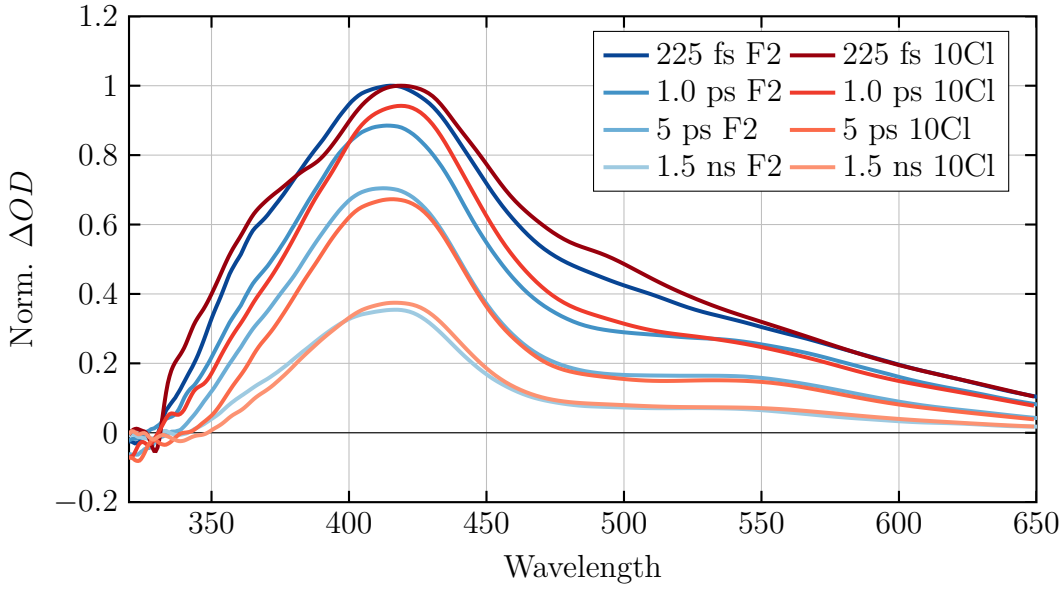


**Figure 4.22** Comparison of spectral slices for 1 $\mu M$ F2 in MeCN with 300nm excitation with and without ten equivalents of chloride. Darker traces indicate earlier times. Darker traces indicate earlier times.

These results show that the TA surface for both F1 and F2 are not influenced by the addition of chloride ions. This is in conflict with the known variation in binding efficiency caused by photoisomerization. The chloride binding could occur on a timescale longer than that measured here, or the change in the concentration of the helical conformation may be below the detection limits of the experimental setup used in this work.

## 4.4 Conclusion

Excited state relaxation of the foldamer family of molecules is similar to AB with no evidence of a different pathway being taken. There is a lengthening in the $S_1$ state branching lifetime from 1.1 ps in AB to 1.7 ps for F1 and 4.2 ps for F2 half, which corresponds to the increasing substitution of AB moiety of the molecule. The separation of branching and relaxation dynamics through the $S_1$ to electronic ground state intersection is consistent with the observations. It was found that the $S_1$ relaxation becomes longer with increased steric bulk of the AB substituents. This was supported by the progressive decrease in signal associated with the thermalization as the $S_1$ relaxation time became longer than thermalization in the electronic ground state.

The solvent effects showed little difference for all members of the foldamer family tested, except for F2. This little variation suggests that the dynamics of the AB moiety are not affected by the larger macro structure of the foldamer. The lack of variation in signal prevents any conclusions being made about the timescale or yield of folding. It could be that this occurs on a longer timescale than that measured, or there is not an absorption associated with the folding. The variation in F2 does provide one avenue in which folding could be studied with a solvent–dependent signature that corresponds to the random–coil structure.

# Chapter 5

# Oxazine - Light Activated Switch

## 5.1 Introduction and Background

Oxazine (OX) is a photochromic compound that undergoes a change in its absorption spectrum upon photoexcitation. The absorption spectrum of oxazine exhibits a peak at 310 nm, and upon photoexcitation a new peak appears at 440 nm.[70] The visible absorption band disappears on the nanosecond timescale due to relaxation back to the ground state.[71] This photochromic nature, with a relatively short lifetime, makes OX suitable for a number of applications. These include optical logic gates, where the fast thermal relaxation is related to processing speed;[72] and fluorescent imaging where induction of absorption changes can aid in resolution.[73]

OX was designed and first synthesized by Raymon et al[70,74] and is based on the well known spyropyran/spyroxazine (SP) group of photo–active compounds.[26,74] For both OX and SP the breaking of the carbon–oxygen bond results in the formation of the *(*p)–nitrophenolate chromophore, with the difference being the involvement of a *cis* to *trans* isomerization step for SP (Figure 5.1).[75,76] This change results in the thermal relaxation from the photo–produce back to the original state to be reduced from taking millisecond in SP to nanoseconds in OX. The bond breakage for SP has been inferred to be on the picosecond timescale,[26,77,78] while that for OX had not not been determined, prior to the work presented in this chapter.

Upon excitation of OX a strong absorption band appears at 440 nm. This is due to carbon–oxygen bond cleavage, which results in the formation of the *p*–nitrophenolate chromophore. Figure 5.2[79] shows the spectra of OX and *p*–nitroanisole (orange)overlapping, while the *p*–nitrophenolate (green) absorption spectrum overlaps well with that of

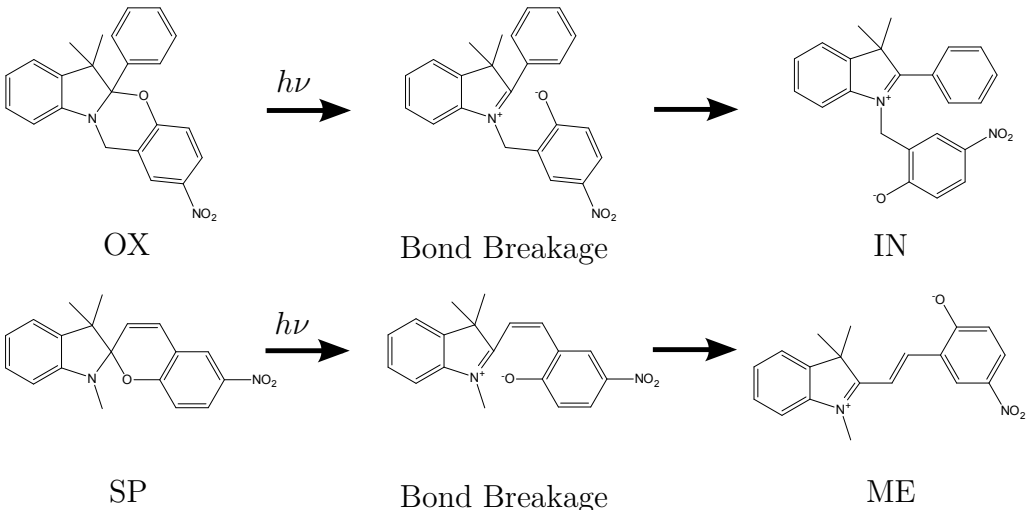


**Figure 5.1** Comparison between the formation of the relaxation of the initially C-O bond cleavage to the final photoproduct. Top: OX final photoproduct forms after rotation. Bottom: SP requires cis-trans isomerization to give the relaxed photoproduct.[70]

the chemically prepared ring–open hemiaminal form (HE). This assigns the initial spectrum to the *p*–nitroanisole fragment, and the photoproduct to *p*–nitrophenolate fragment. Computational studies reported in the literature further support this assignment.[76] A bathochromic shift of the UV absorption is expected as the ring opening extends the conjugation through the formation of a $\pi$–conjugated phenyl ring being incorporated into the original chromophore.[75]

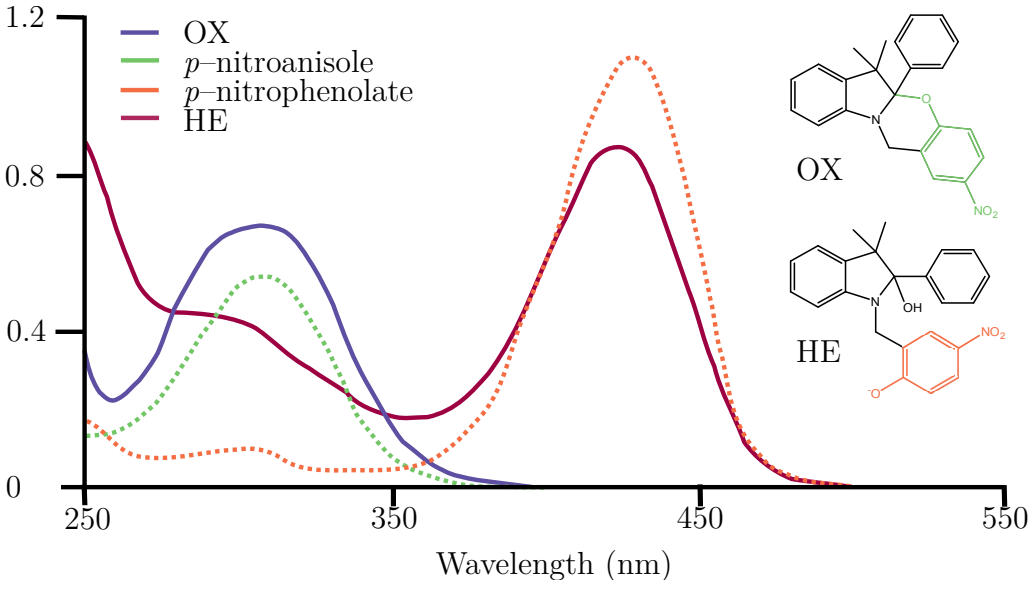


**Figure 5.2** Comparison between chromophore fragments, *p*–nitroanisole (green), *p*–nitrophenolate (orange) and the spectra of OX (purple) and the ring open HE (red)[70]

The thermal relaxation after photoexcitation has been studied using nanosecond transient absorption (TA) spectroscopy techniques.[70] However, such experiments were unable to provide information about the the initial carbon–oxygen bond cleavage, or the opening timescales and mechanism. This highlights the need to resolve

sub–nanosecond dynamics and is the area of interest for this research. Elucidation of the processes will provide insight which will be valuable to the future application of OX in photo–active materials.

The photoisomerization process will be studied using TA spectroscopy, by looking at three different compounds, OX, difluoro–oxazine (OXF), and difluoro–indole (INF), shown in Figure 5.3. OXF has fluorine substituted for the methyl groups at the six position. This influences the zwitterionic ring–open state as the fluorine atoms have a strong electron withdrawing effect. The effect of this is to increased the partial positive charge at the carbon center where bond cleavage occurs. INF is a structural fragment of OXF, but differs by not possessing the second chromophoric unit. The absence of stabilizing effects of the phenol group are no longer present, will impede isomerization. This reveals the excited state dynamics of the initially excited *p*–nitroanisole chromophore when relaxation via isomerization is not possible.

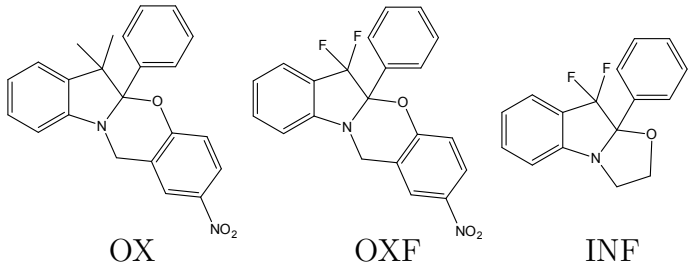


OX OXF INF

**Figure 5.3** Chemical structure of oxazine and derivatives.

To elucidate the mechanistic steps, the solvent polarity will be altered. This will affect the stability of the zwitterionic ring open form and give an indication of when this state is formed. This will be investigated for both the OX and OXF derivative, as the increased charge at the carbon center could lead to varying solvent effects.

## 5.2 Transient Absorption Spectroscopy

Acetonitrile was chosen to investigate first, as it is reported that isomerization and thermal relaxation of OX occur in this solvent.[70] Figure 5.4 shows a TA surface of a solution of OX excited at 300 nm, and shows three sequential time–dependent states. The initial state consists of two photo induced absorption (PIA) signatures one at 500 nm and another that overlaps with the ground state bleach (GSB) at wavelengths lower than 350 nm. The decay to a 'dark' state (with no optical absorption over the studied wavelength range) in the early picosecond regime is indicated by the recovery of the GSB without a corresponding PIA. There is the growth of a PIA feature at 440 nm, which is attributed to absorption of the ring–open form (Figure 5.2).

A minimum of three transient states are needed to adequately describe the PES, which precludes the pathway of direct isomerization from the initial excited state. The transition from the excited state directly to isomerized form will not result in the observed 'dark' state, as there would be population in at least one of the photo–active states over the entire time period followed.

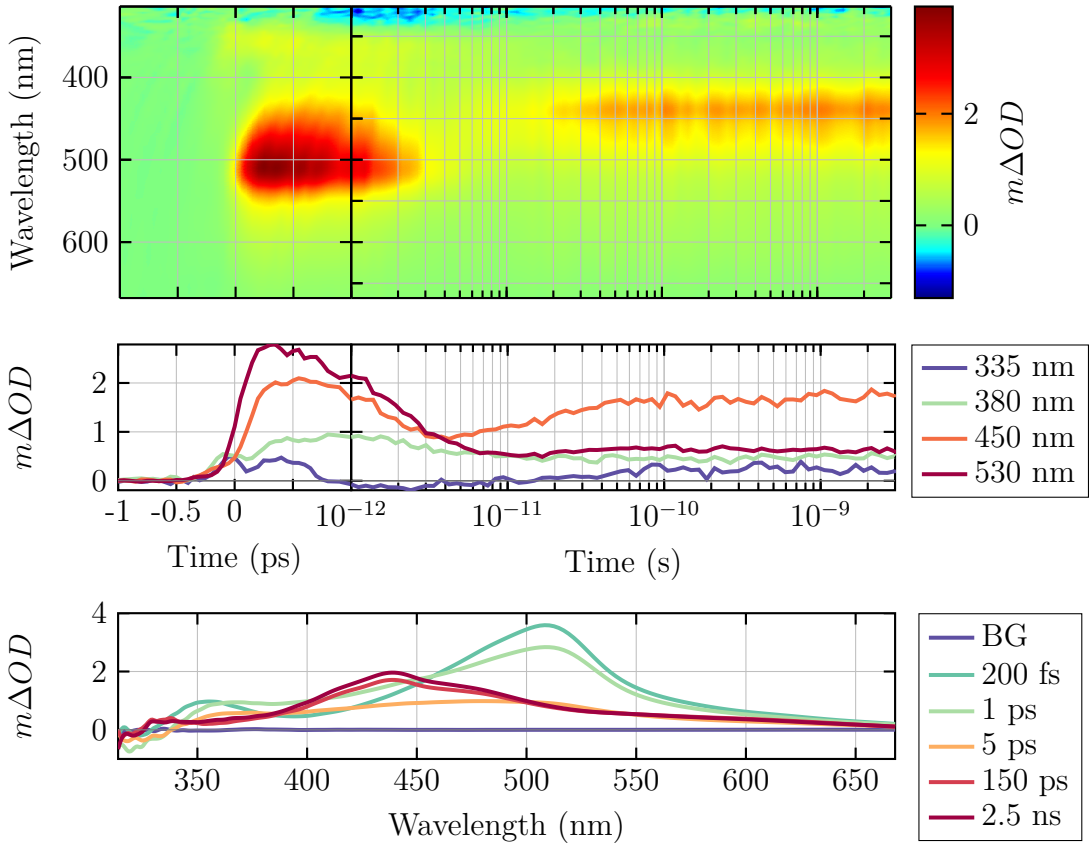


**Figure 5.4** TA data for OX ~0.5 $\mu$M in acetonitrile with 300 nm excitation. *Top:* TA surface. *Middle:* Kinetic traces. *Bottom:* Spectral slices.

Assignment of the transient absorption to the ring–open isomer was confirmed by a study of the structural fragment INF (Figure 5.3). This molecule is the initially excited chromophore without a secondary ring that stabilizes the ring–opening. This provides a good probe of how the initial excited chromophore decays, and any distinct features. Figure 5.5 shows the TA surface of INF which comprises a PIA peak at 540 nm and another in the UV spectral region. There is no evidence for a transition into a 'dark' state as seen in OX. The appearance of PIA at 440 nm is absent, confirming that this feature can be attributed to the isomerization photoproduct of OX.

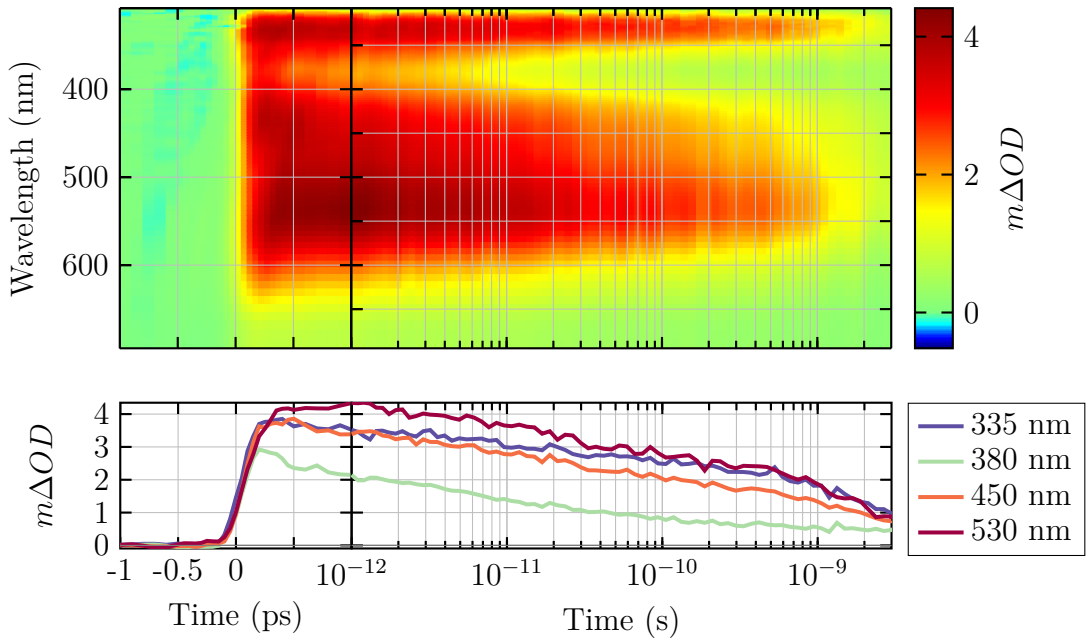


**Figure 5.5** TA data for INF 1 $\mu M$ in acetonitrile with 300 nm excitation. Top TA surface, Bottom Kinetic traces.

### Global Fitting

Global fitting of the OX surface shows that four lifetimes are required to adequately fit the data. The species–associated–spectrum (SAS) are shown in Figure 5.6. The first SAS (SAS1) decays with a lifetime of 1.9 ps, and has an absorption spectrum consisting of two PIA features, one centered at 520 nm and another that overlaps with the GSB, associated with the sharp transition at 330 nm.. SAS2 has a lifetime of 13.8 ps, and shows the recovery of the GSB with a plateau throughout the visible region. SAS3 contains an absorption feature at 440 nm, corresponding to the absorption of the ring–open form. It also has a PIA at 350 nm that is attributed to the increased $\pi$–conjugation from the planar phenol ring in this state. The lifetime of the relaxed ring open state was found to be 22 ns (Figure 5.7), using a TA setup with an electronically controlled pump pulse. This relaxed ring–open lifetime is in agrement with previous reports in the literature.[70]

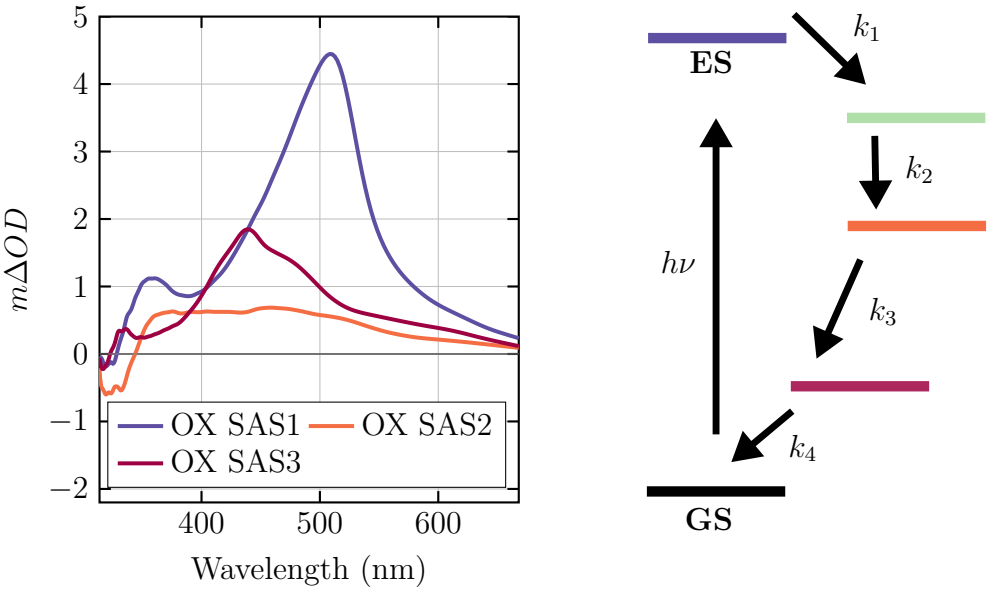


**Figure 5.6** SAS of oxazine determined by global fitting (left) determined by using a first order sequential decay (right). If $k_2$ is $< k_1$ the green state will not be observed.

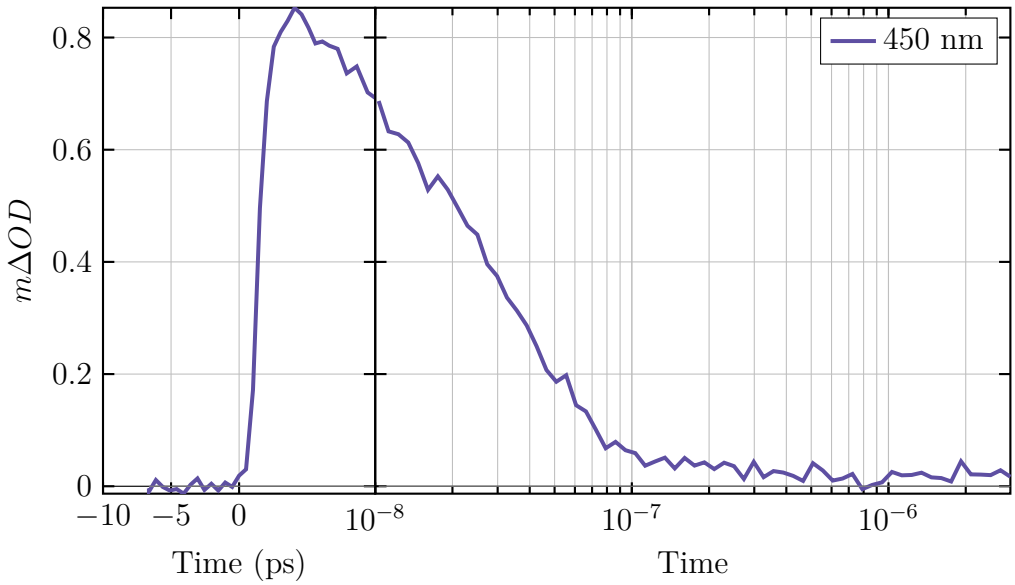


**Figure 5.7** Kinetic trace of the nanosecond decay component of 0.5 $\mu M$ oxazine in MeCN with 300 nm excitation.

### 5.2.1 Isomerization Mechanism

The isomerization of oxazine can be broken down into two conceptual steps shown in Figure 5.8; ring opening and rotation to give the final photo–product. Ring opening is indicated by the formation of the new chromophore, whilst rotation is indicated by a hypsochromic spectral shift of the initial chromophore due to extended $\pi$–conjugation. Both of these appear as PIA features at nanosecond timescales on the TA surface. To assign the conceptual states, as well as any intermediates to those observed during TA, both polarization anisotropy and solvent polarity effects were studied.

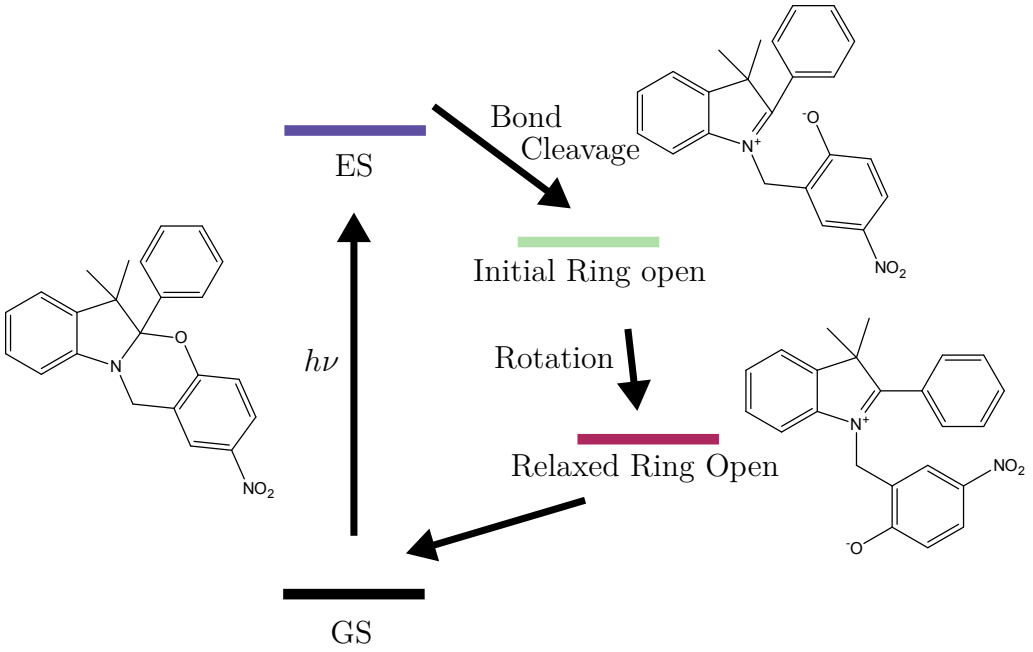


**Figure 5.8** The steps needed to give the final ground–state ring open structure of oxazine. This proceeds via carbon–oxygen bond cleavage, and then rotation.

#### Polarization Anisotropy

Anisotropy (r) is defined by Equation 5.1,[80] as the difference between signal intensity when the probe pulse is oriented parallel ($\parallel$) and perpendicular ($\perp$) to that of the pump pulse. This is then normalized by total signal intensity to give the final anisotropy value. The maximum anisotropy attainable when polarized light is used is 0.4 due to photo–selection rules that result in a distribution of ground state molecule orientations being excited.[80] Decay from the 0.4 maximum value occur due to processes that result in the reorientation of dipole moments. This can be from rotation of the excited chromophore, or due to tumbling effects in the solvent. Tumbling timescales depend on the size of molecule and viscosity of solvent, but are generally on the order of tens of picoseconds.

$$r = \frac{\Delta OD_{\parallel} - \Delta OD_{\perp}}{\Delta OD_{\parallel} + 2\Delta OD_{\perp}} \tag{5.1}$$

To determine if the dark state can be attributed to the rotation of the chromophore out of the plane of probing light, polarization anisotropy was examined. The polarization might have an effect as the new chromophore has an orientational distribution of dipole moments determined by the polarized state of the pump pulse. Upon rotation the dipole moment of the newly formed chromophore rotates so that the polarized probe pulse may have a lower interaction, hence a transition to a dark state could be observed. Following this, PIA recovery would be expected as tumbling leads to a redistribution of the orientation of dipoles to one with a more favorable interaction with the probe pulse (Figure 5.9).

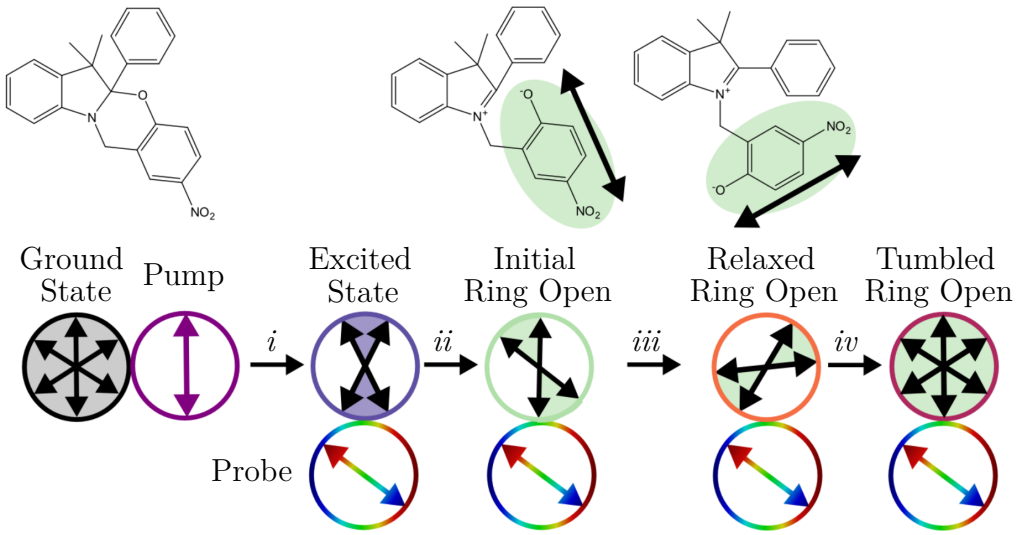


**Figure 5.9** Polarization dependence on the dipole moment of oxazine. Arrows indicate polarization state of dipole, or laser pulse. Pump pulse narrows the distribution of dipole moments of excited state (ES). *i* Excitation, *ii* Bond cleavage, *iii* Rotation, *iv* Tumbling.

Figure 5.10 shows time dependent anisotropy at two wavelengths; 440 nm corresponding to the relaxed ring–open PIA, and 530 nm being the initial excited state PIA. The anisotropy signal within 300 fs is affected by coherent artifacts. This decreases the value in the spectral region where there is a PIA, as the signal due to coherent artifacts has the opposite sign to the PIA. The decay at 450 nm and 530 nm are similar, showing no difference in anisotropy decay for these two features. The 5 – 10 ps region is where the dark state is observed, which if this was due to rotation of the chromophores a decrease in anisotropy is expected as this rotation occurred.

The polarization anisotropy decay obtained instead exhibits a decay on the tens

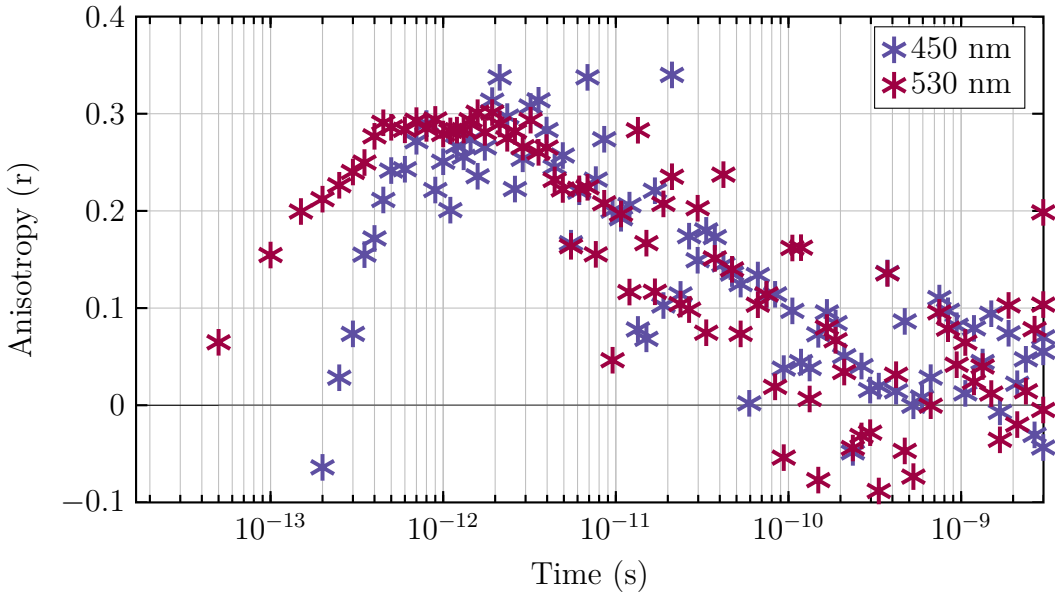


**Figure 5.10** Anisotropy of TA signal of 1 $\mu M$ oxazine in MeCN with 300 nm excitation. 440 nm trace is at wavelength of new chromophore, while 530 nm traces is initial PIA.

to hundreds of picosecond, this is what is expected for tumbling of a molecule of this size under these solvent conditions.[81,82] From this we can conclude that the dark intermediate state formed on the picosecond timescale does in fact have a low absorption coefficient, and is not an artifact of polarization. The next section well include further details on the investigation of the dark state.

### Solvent Dependance

Due to the zwitterionic nature of the ring–open form, solvent polarity will influence the formation of; and lifetime of the relaxed ring–open form. To investigate these effects, TA was carried out in solvents of different polarities (ethanol, acetonitrile, dimethyl sulfoxide, dimethylformamide, dichloromethane, chloroform, tetrahydrofuran, and hexane). To confirm if the observed changes are due to zwitterionic effects, OXF with more electron withdrawing groups was examined in the same solvent environments.

Four decay sequences are observed across the solvents studied, which are illustrated in Figure 5.11. They each feature the initial excited state with varying decay rates. Each of these will be described below. In particular, there are four different features to take note of. The initial PIA occurs at ~500 nm, which is characteristic of the first excited state. The relaxed ring–open state with a PIA at ~440 nm. This is differentiated from the initial ring–open state by the GSB, which is not present in

the relaxed ring–open state. Finally, we can identify a dark intermediate, which is indicated by an absence of PIA features across the spectrum, but retention of a GSB at wavelengths below ~350 nm. This could possibly be associated with a triplet state, which has been suggested as a pathway in other photo–isomerizing compounds. The normally forbidden transition between singlet and triplet state becomes allowed by the ring–rotation conserving angular momentum.[83–86] The triplet state being involved in the overall isomerization pathway has been supported by a computational study in the literature, with transfer to a triplet state being the lower energy pathway.[76] The evidence provided by TA will be followed up at a later date using density functional theory (DFT) calculations, to confirm the optical signature a triplet state intermediate.

The sequences are described and numbered in order of decreasing solvent polarity. Sequence one, (top left Figure 5.11) is the same as that observed in acetonitrile. It consists of the initial excited state that decays to the dark state within a few picoseconds, with the growth of the final PIA feature in tens of picoseconds, corresponding to the relaxed ring–open state. This sequence shows clear indication of isomerization, with the formation of the relaxed ring–open form observed.

Sequence two, (top right Figure 5.11) shows the initial PIA feature shifts to one that corresponds to the absorption of the ring open photo–product within 1 ps. This subsequently decays to a dark state in tens of picoseconds, with the recovery of the relaxed ring–open PIA feature within hundreds of picoseconds. The difference between sequence two and sequence one is the shift of the initial PIA before decay to the dark state. The shift is associated with the breaking of the carbon–oxygen bond, to form the ring open isomer, this is due to the shift in PIA feature to ~440 nm corresponding to the new chromophore. Evidence for this can be seen when comparing the normalized spectral traces (Figure 5.12) at 250 fs, 3 ps and 2.5 ns of sequence two. These show that at 3 ps and 2.5 ns there is a similar feature at 450 nm, with the difference being in the peak broadness. A shift from the initial PIA at 250 fs can be seen in both longer timescale spectral slices. The PIA at 2.5 ns and 3.0 ps are distinguished by the increase in intensity at wavelengths lower than than 340 nm for the 2.5 ns trace. This differentiates the relaxed ring–open form (2.5 ns), from the initial ring–open form (3 ps), as the rotation of phenol ground leads to increased absorption at lower wavelengths. While sequence one reflects concerted bond breakage and rotation to form the relaxed ring–open state via a dark intermediate, whereas sequence two reflects a more hindered process. In sequence 2 rotation via a dark state is preceded by distinct intermediate, where only the bond has broken (Figure 5.14). Slower rotation can be accounted for in a less polar solvent due to the coulombic attraction of the zwitterionic state.

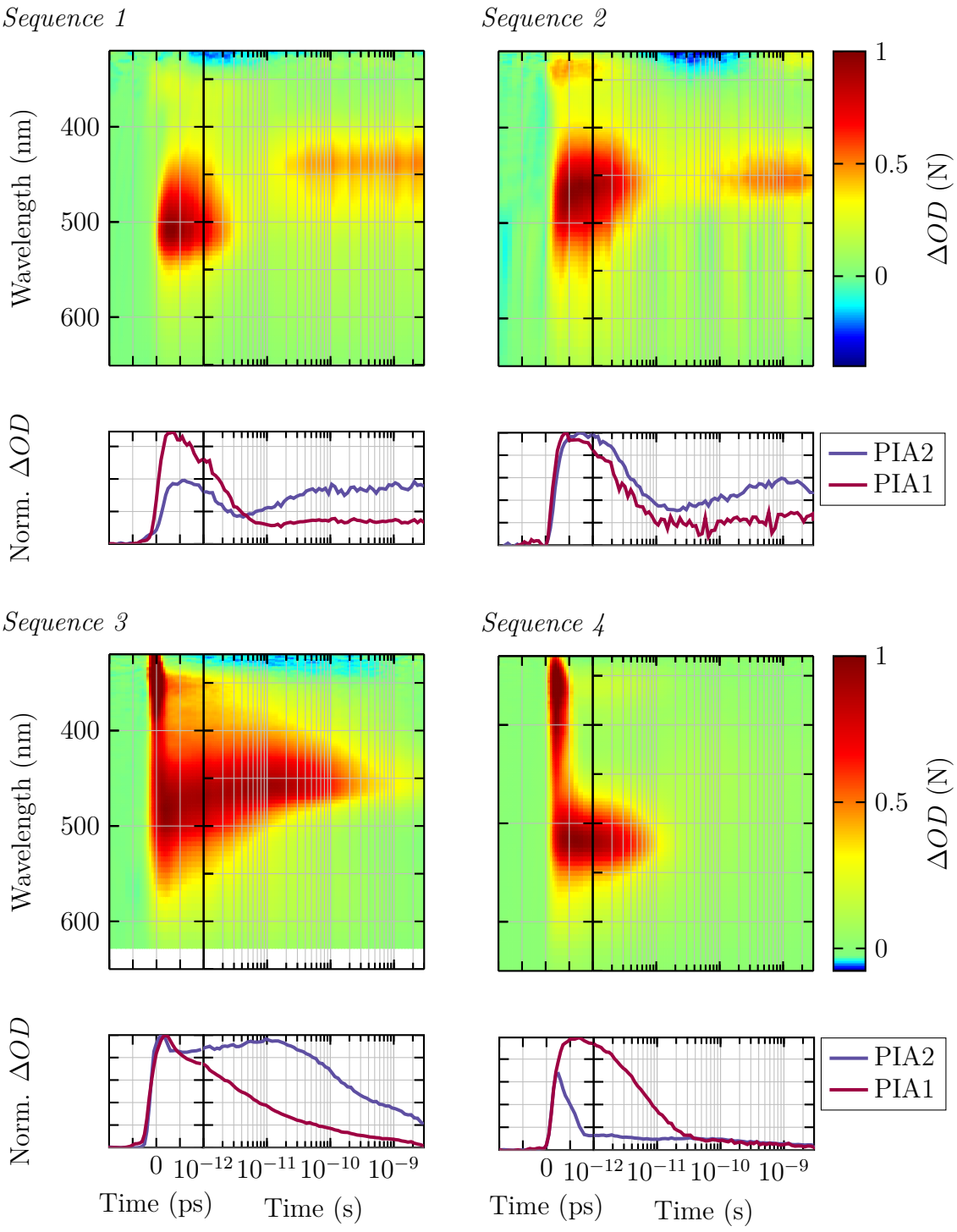


**Figure 5.11** TA surfaces for the various decay behaviors observed for OX and OXF in different solvents (concentration is 0.5 $\mu M$ with 300 nm excitation for both OX and OXF). Kinetic traces for each TA surface are below, they include a trace that corresponds to the initial PIA (red) and a second that follows the photoproduct peak (purple) Top Left: Sequence One, OX in acetonitrile. Top Right: Sequence Two, OXF in acetonitrile. Bottom Left: Sequence Three, OXF in chloroform. Bottom Right: Sequence four, OX in tetrahydrofuran.

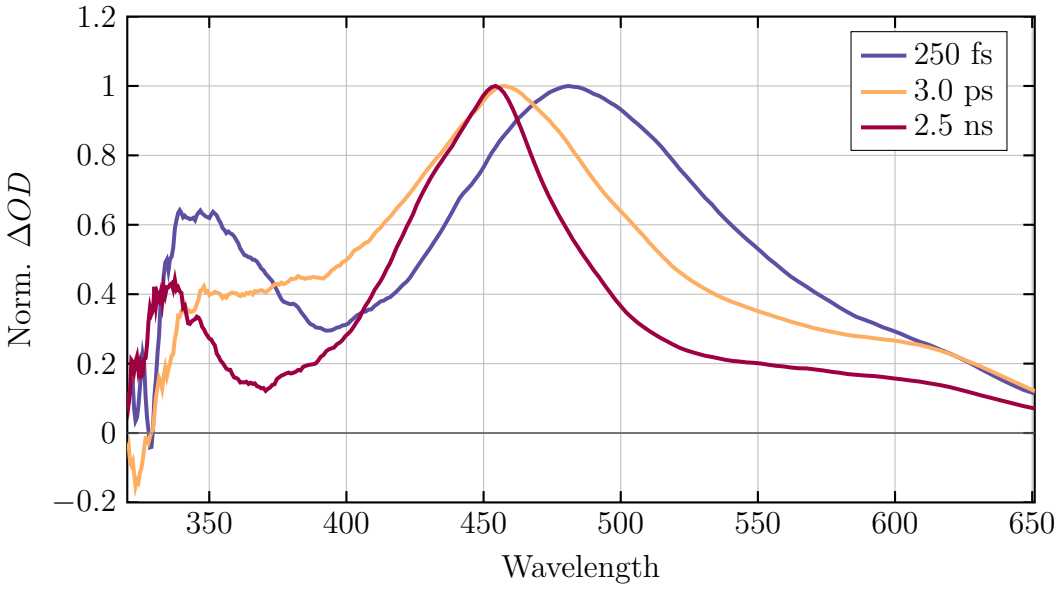


**Figure 5.12** Normalized spectra slices of 0.5 $\mu M$ OXF in MeCN with 300 nm excitation decaying via sequence two. A hypsochromic shift is observed between 250 fs and 3.0 ps, and a narrowing observed by 2.5 ns.

Sequence three, (bottom left Figure 5.11) contains two excited state decays. The initial excited state decays to a new PIA feature at ~440 nm, occurring on the picosecond scale. It appears on the surface like a hypsochromic spectral shift, but the two states can be distinguished due to the decay of the PIA at 350 nm being replaced by a GSB. This new PIA decays on a time scale of hundreds of picoseconds, to leave a low signal at the edge of the time window used in this study. When compared to the two previous sequences there is no nanosecond component or dark state. The absence of a long lived component, along with the presence of GSB, excludes the formation of the ring–open rotated species being formed. The other difference is the timescale that the second PIA lives for. The second PIA extends over hundreds of picoseconds which is much longer then sequence two. Figure 5.13 shows a comparison between long time spectra shapes for both sequence two (OXF in acetonitrile and ethanol) and sequence three (OXF in chloroform and hexane). The feature at ~440 nm is similar for both sequences, which supports the assignment in sequence two that the first intermediate arises from the initial ring–open form. The lower polarity solvent screens the electrostatic attraction between the zwitterionic charges less, giving a greater coulombic attraction thereby increasing the timescale of rotation. In this case the suppression of the rotation pathway is significant enough that non–isomerizing decay pathways are favored such that there is no distinguishable formation of the relaxed ring–open photo–product. Moreover, no dark intermediate is observed in sequence three suggesting that the dark intermediate observed in sequence one and two is only allowed with rotation to the relaxed ring–open form. Although further investigation is required these results suggest that the dark state involves a triplet

state.

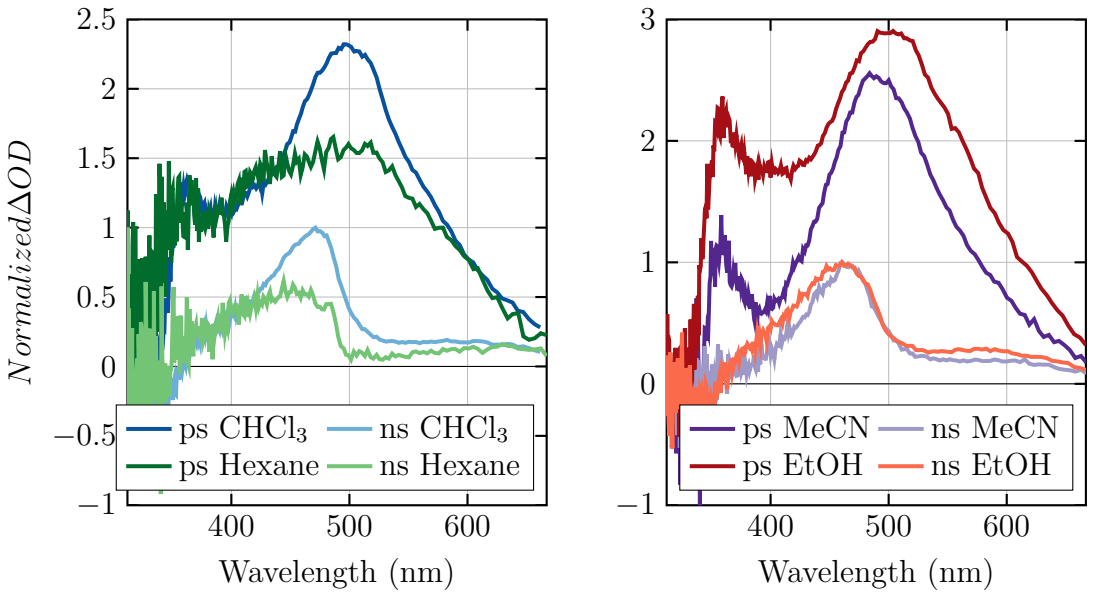


**Figure 5.13** Comparison of the early (dark) and late (light) time spectral slices in different solvents. Left side consists of lower polarity solvents, right has more polarity solvents.

Sequence four, (bottom right Figure 5.11) was only seen in highly polar dimethlysulfoxide. It consists of the initial excited state decaying in a few picoseconds, without the formation of a latter state. This rapid decay without isomerization suggest that dimethlysulfoxide suppresses the ring opening step of isomerization. This is an outlier to other observations as the polarity is 45.1 measured on the ET-30 solvent polarity scale, which is similar to that of acetonitrile (45.6) [87,88] , and in these conditions it undergoes isomerization. Dimethyl sulfoxide is frequently observed to exhibit behaviour counter to expectations when considering bulk polarity effects. This is often attributed to specific solvent–solute interactions like hydrogen bonding. The nature of this rapid deactivation observed warrants further investigation but is beyond of the scope of this work.

Figure 5.14 summarizes the decay pathway observed in the various sequences. After initial excitation decay occurs via breaking of the carbon–oxygen bond, only in dimethlysulfoxide is this not observed. In less polar solvents, decay to the ground state is seen over hundreds of picoseconds, whereas for more polar solvents rotation of the carbon linkage joining the two chromophores occurs via a dark state in a timescale of ones to tens of picoseconds. This is found to be dependent on solvent polarity and the presence of electron withdrawing groups. This gives rise to the relaxed ring–open photo–product, and recovery of the original oxazine species occurs in the nanosecond regime.

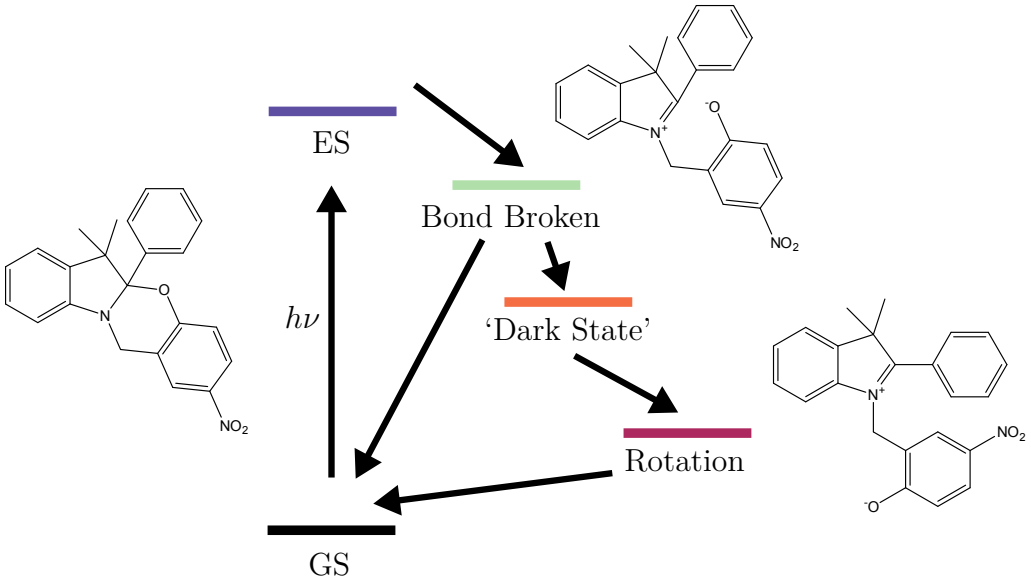


**Figure 5.14** Proposed model that fits observed data. Carbon–oxygen bond cleavage occurs in all solvents. Branching then occurs with more polar solvents photo–isomerizing via the dark state, and less polar decaying to the ground state.

Table 5.1 summarizes the behavior of OX, and OXF in different solvents. They are attributed to the different models based on the observed time dependent features with the lifetimes determined by global fitting. The solvent polarity has an effect of the sequence seen for both OX and OXF. OX decays via sequence one in the more polar solvents (acetonitrile and ethanol), whilst a reduction in polarity (chloroform and dicholoromethane) results in decay via sequence two. Non–polar solvents (tetrahydrofuran and hexane) result in decay via sequence three.

**Table 5.1** Fitted rates for OX and OXF and the corresponding models assignment

| **Solvent** | **Comp** | **Sequ** | **Et-30** | $\tau_1$/ps | $\tau_2$/ps | $\tau_3$/ps | $\tau_4$/ps |
|---|---|---|---|---|---|---|---|
| EtOH | OX | 1 | 51.9 | 4.4 | (>4.4) | 10.8 | <8000 |
| MeCN | OX | 1 | 45.6 | 1.9 | (>1.9) | 13.8 | 22000 |
| DCM | OX | 2 | 40.7 | 5.8 | 140 | 7400 | <8000 |
| Chloroform | OX | 2 | 39.1 | 17 | 100 | 4600 | <8000 |
| THF | OX | 3 | 37.4 | 4.2 | 2700 | | |
| Hexane | OX | 3 | 31.0 | 1.8 | 850 | | |
| DMSO* | OX | 4 | 45.1 | 12.7 | | | |
| EtOH | OXF | 2 | 51.1 | 1.8 | 21 | 1900 | <8000 |
| MeCN | OXF | 2 | 46.6 | >0.2 | 4.1 | 930 | <8000 |
| DCM | OXF | 3 | 40.7 | 3.2 | 67 | | |
| Chloroform | OXF | 3 | 39.1 | 3.8 | 98 | | |
| THF | OXF | 3 | 37.4 | 5.6 | 930 | | |
| Hexane | OXF | 3 | 31.0 | 8.5 | 620 | | |
| DMSO* | OXF | 4 | 45.1 | 230 | | | |

Electron withdrawing substitution at the six position behaves in a manner consistent with the proposed interaction for each state. Sequence one is not observed, this is

due to the large electrostatic attraction slowing rotation after ring opening. When comparing OX and OXF, there is a general shift in the sequence observed with majority of OXF decaying via sequence three, and only polar solvents (acetonitrile and ethanol) decaying via sequence two.

## 5.3 Conclusion

Transient absorption spectroscopy was used to probe the ring opening and rotation timescales of the photoisomerization of oxazine. By studying the photoisomerization using solvents with a range of polarities it has been established that the isomerization happens through three states, bond breakage, transfer to a dark state and the final photo–isomer. This was confirmed through the investigation of electron withdrawing fluorine groups on the photoisomerization process.

Carbon–oxygen bond cleavage occurs on the picosecond timescale, with solvent dependent rotation occurring in the hundreds of picoseconds. This was determined by comparing the solvent effects for both OX and OXF. OXF shows a strong solvent dependence with rotation suppressed in all but the most polar of solvents.

# Chapter 6

# Future Work

Looking to the future, improvements in transient absorption (TA) spectroscopy should be considered. Two areas of improvement would have a high impact when considering resolving photoisomerization dynamics. The first would be to increase the signal to noise ratio over the UV spectral region of the probe pulse. This could be achieved by increasing the intensity on the photodiode array (PDA) such that background noise from the PDA is minimized, and also implementing shot–to–shot referencing to correct for intensity fluctuations in the probe pulses. The second area of importance is the temporal resolution, which is currently limited by the pump pulse full width half maximum (FWHM). It is possible, through the use of optics to compress this further allowing for better temporal resolution in the sub picosecond regime.

Further detail needs to be looked into about the long lived state of the foldamer. Nanosecond transient absorption spectroscopy, and other time–resolved vibrational spectroscopy techniques should be employed to get a better understanding of what this long lived state corresponds to. On the shorter timescale, femtosecond Raman promises to be able to resolve structural details on the femtosecond timescales. This could be used to investigate the timescale of folding providing structural data to complement the electronic data already presented. The initial conformation of azobenzene in these studies is dominated by the *trans* isomer, the application of a high–powered LED in the visible region would allow the comparison to this *cis* isomer a starting point that favors the random coil conformation of the foldamer.

Oxazine studies have given insight into the pathway of isomerization and this needs to be followed up by computational studies to investigate the viability of this mechanism for both oxazine and its fluorinated derivative. In particular, emphasis needs to

be placed on investigating the absorption spectral–temporal signature expected for any triplet intermediate. Computational studies can also be used to investigate the effect that the fluorination of oxazine has on the energy barriers involved in isomerization and if these match with what has been observed. Other electron withdrawing or donating groups could be substituted for fluorine to investigate the validity of the conclusion made. With this approach care must be taken to understand the influence of steric barriers to ring–opening and rotation to the relaxed ring–open form. Finally the rapid decay of the excited state observed in dimethlysulfoxide deserve further investigation.

# Chapter 7

# Experimental

## General Methods

All chemicals were purchased from Sigma-Aldrich (St. Louis, MO) and used as received, unless otherwise stated. 6,6-dimethyl-2-nitro-5a-phenyl-6,12-dihydro-5aH-benzo[5,6][1,3]oxazino[3,2-a]indole (oxazine), 6,6-difluoro-2-nitro-5a-phenyl-6,12-dihydro-5aH-benzo[5,6][1,3]oxazino[3,2-a]indole (fluorinated oxazine), and 9,9-difluoro-9a-phenyl-2,3,9,9a-tetrahydrooxazolo[3,2-a]indole (fluorinated indole) were received from Brendan Burkett and co–workers and used as received. Foldamer 1, half foldamer 1, foldamer 2, and half foldamer 2 were received from Amar Flood and co–workers and used as received. All solutions were prepared by making a stock solution of 20 $\mu$M in dichloromethane. Aliquots were then taken and allowed to evaporate in air to give a 1 $\mu$M solution for; azobenzene, half foldamer 1, and half foldamer 2; and 0.5 $\mu$M solutions for; oxazine, fluorinated oxazine, foldamer 1, and foldamer 2.

## Transient Absorption Spectroscopy Measurements

Transient absorption spectroscopy (TA) was performed over a spectral range ~320 – ~650 nm with a temporal range of -15 ps to 2.9 ns using a quartz cuvette with 0.1 mm pathlength. A Ti–sapphire amplifier (Spitfire, Spectra–physics) with pulse duration 100 fs, fundamental 800 nm, operation at 3 kHz was used as the femtosecond laser pulse. Other details of transient absorption setup can be found in Chapter 2. Pump power was 0.11 to 0.13 $\mu$J per pulse, with a pump pulse cross section at the sample having a full width half maximum of 0.3 to 0.5 mm, and collection time averaged

30 minutes per sample. All samples had a volume sufficient to fill the front face of the cuvette, 0.4 mL, at the concentrations noted above (Section General Methods). Azobenzene and all foldamer compounds were illuminated with a 365 nm high power LED set at a power of 800 mA for the duration of collection, to maintain a *trans* isomer dominated photo–stationary state.

## Optical Absorption Spectroscopy Measurements

Absorptions spectroscopy (UV-Vis) was performed over a spectral range of 220 – 1100 nm using a quartz cuvette with 0.1 mm pathlength using an Agilent 8453 UV-Visible spectrophotometer. All samples had a volume sufficient to fill the front face of the cuvette, 0.4 mL and concentrations are as noted above (Section General Methods). All spectra were baseline corrected by subtracting a linear fit to wavelengths from 700 to 800 nm.

# Appendix - Transient absorption surfaces

This appendix contains the transient absorption surfaces for all species and solvents collected. The data is presented on a linear (-1 ps to 1 ps) and log (1 ps to ~3 ns) plot. Background subtraction, chirp correction, and wavelength calibration has been applied.

## Azobenzene

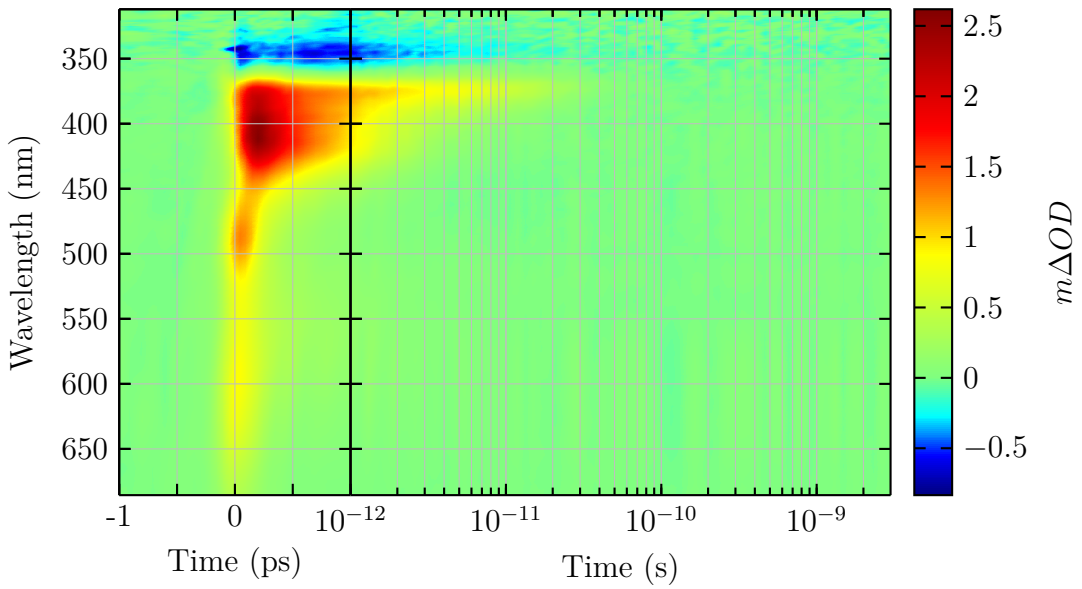


**Figure 7.1** Azobenzene, collected in acetonitrile with 300 nm pump and 470 nm LED exposure.

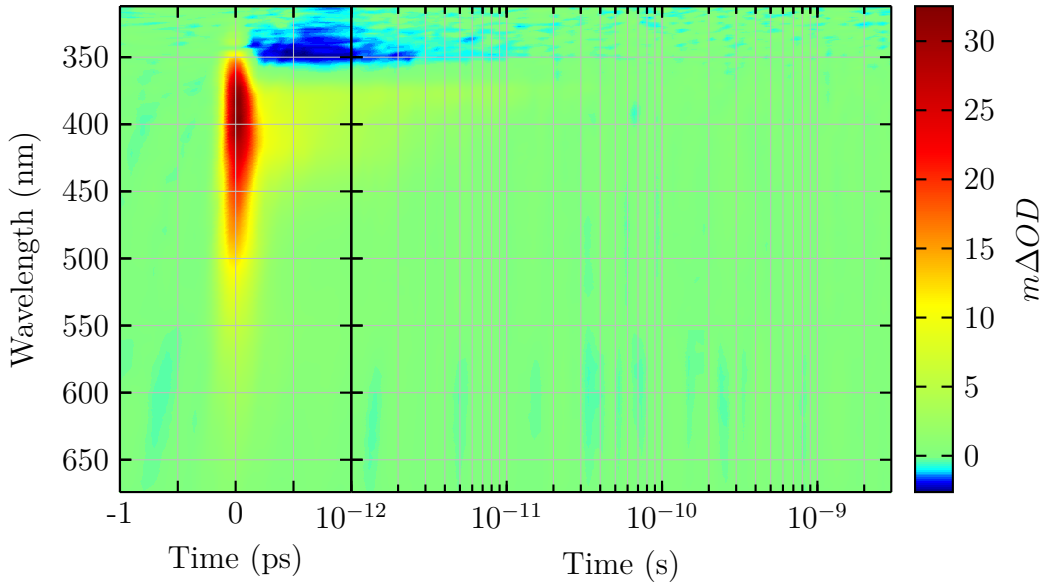


**Figure 7.2** Azobenzene, collected in tetrahydrofuran with 300 nm pump and 470 nm LED exposure.

# Half foldamer 1

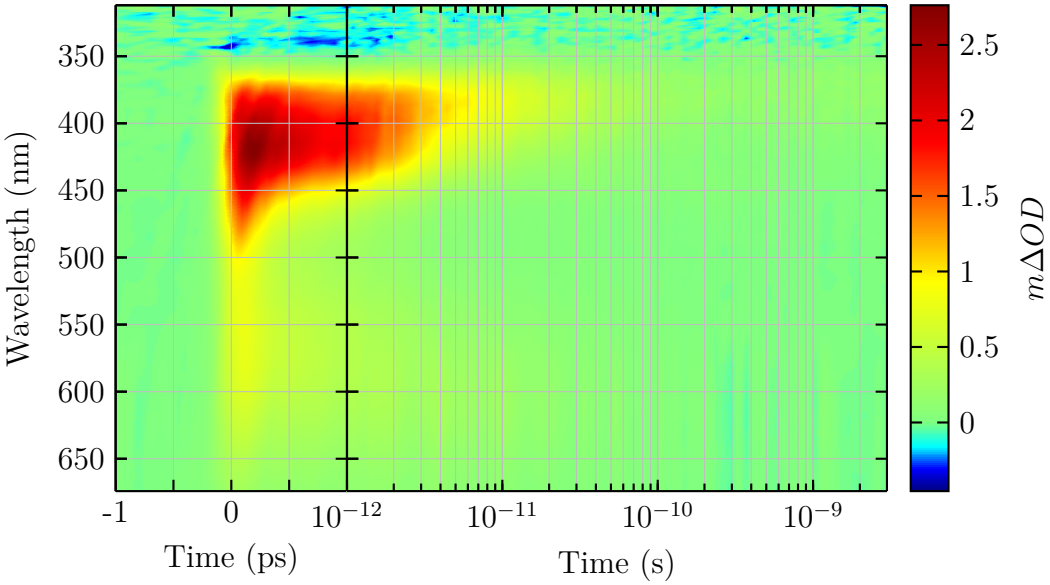


**Figure 7.3** Half foldamer 1, collected in acetonitrile with 300 nm pump and 470 nm LED exposure.

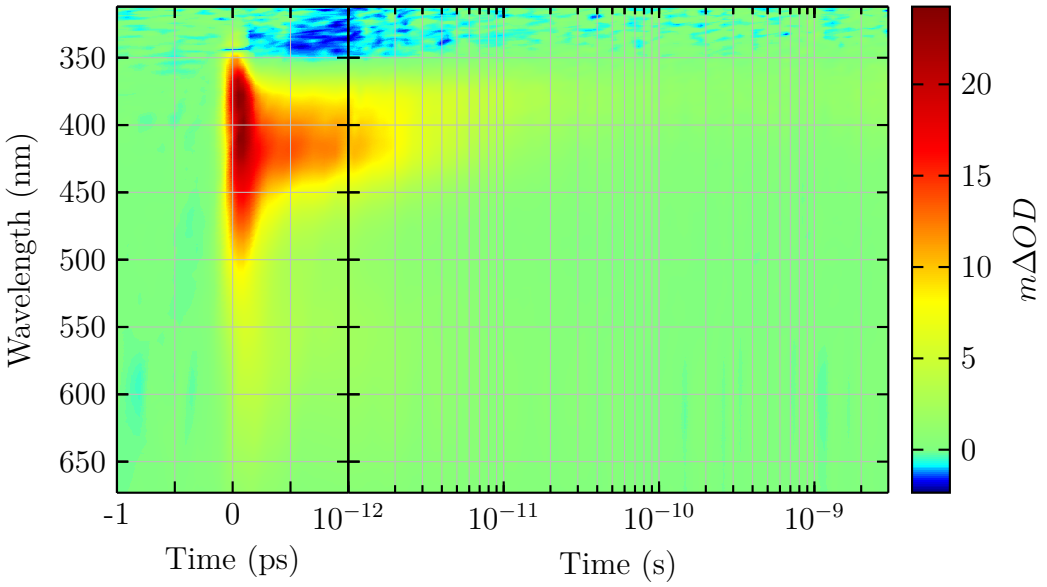


**Figure 7.4** Half foldamer 1, collected in 1:1 acetonitrile:tetrahydrofuran with 300 nm pump and 470 nm LED exposure.

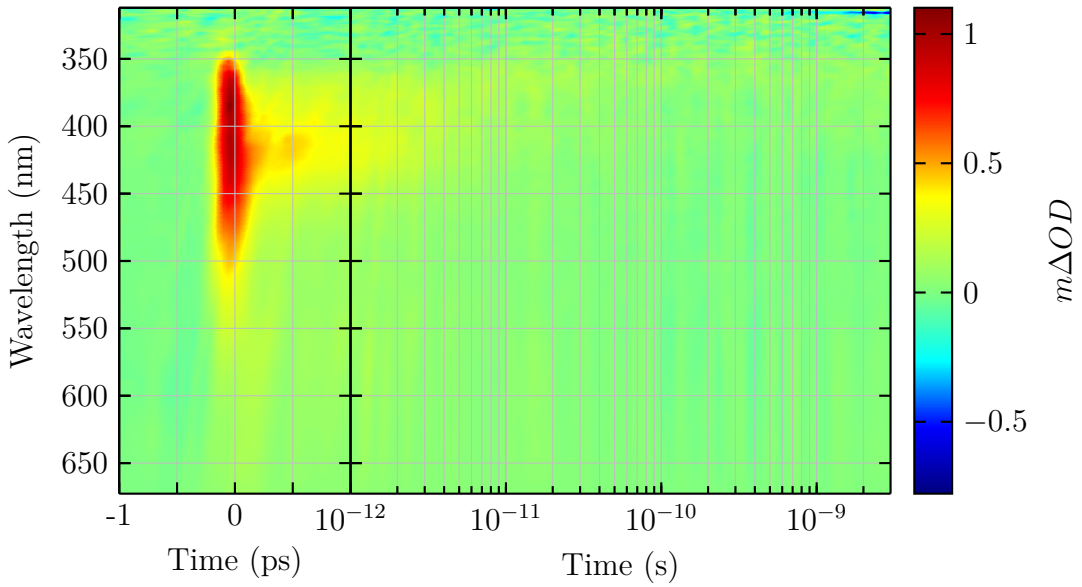


**Figure 7.5** Half foldamer 1, collected in tetrahydrofuran with 300 nm pump and 470 nm LED exposure.

# Foldamer 1

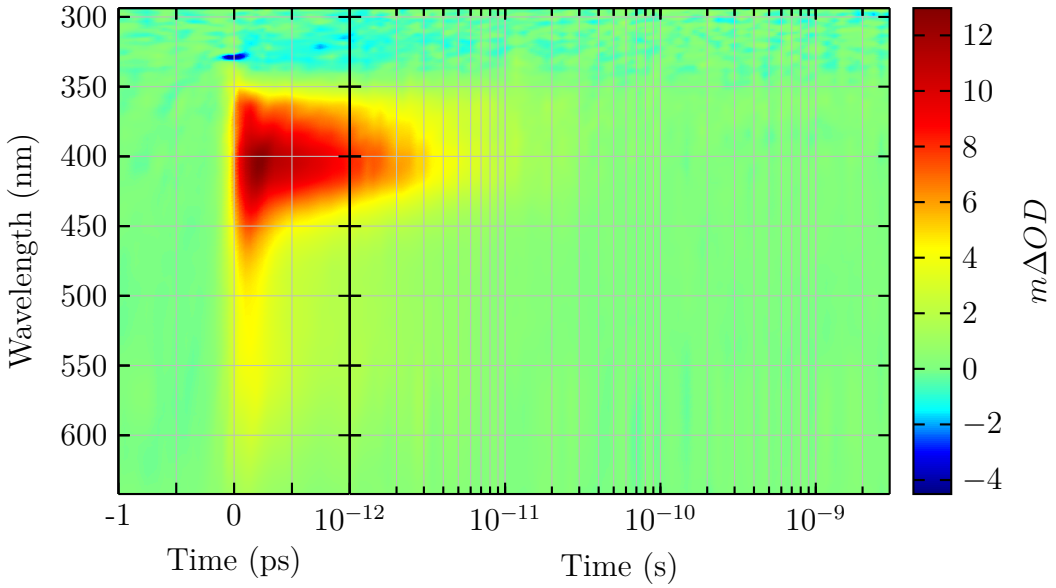


**Figure 7.6** Foldamer 1, collected in acetonitrile with 300 nm pump and 470 nm LED exposure.

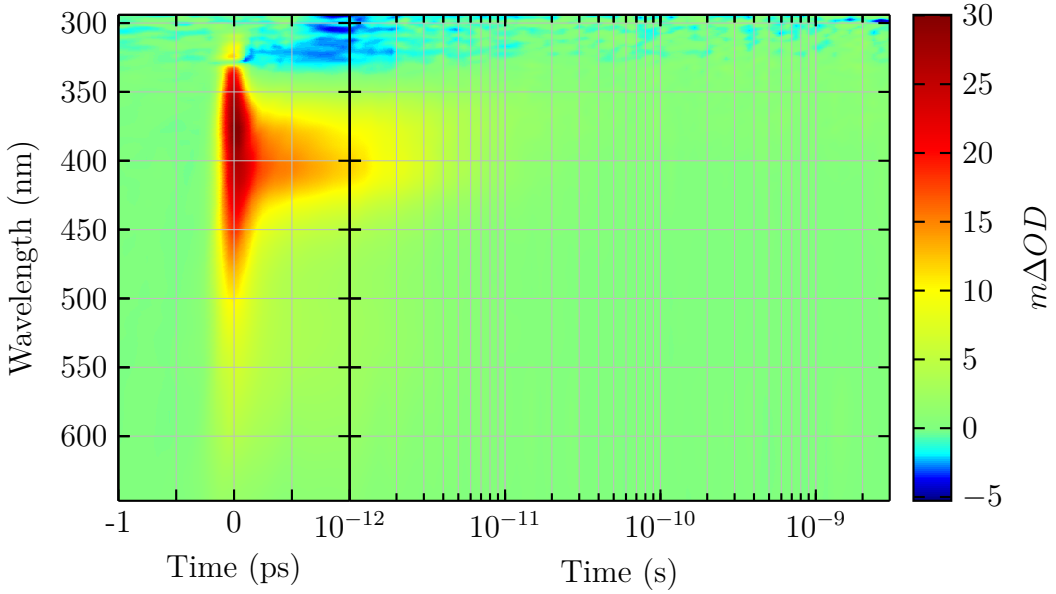


**Figure 7.7** Foldamer 1, collected in 1:1 acetonitrile:tetrahydrofuran with 300 nm pump and 470 nm LED exposure.

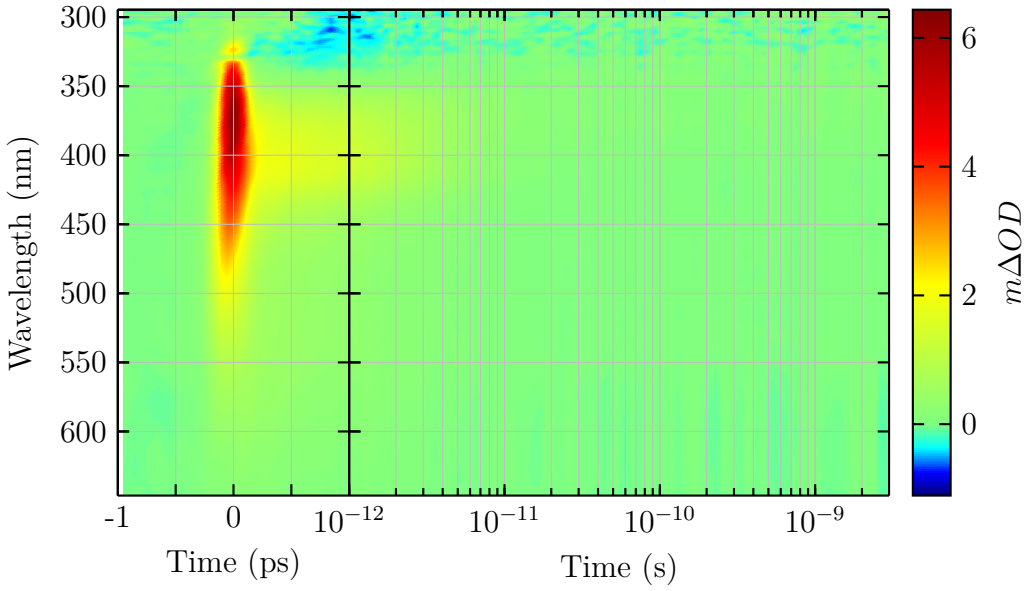


**Figure 7.8** Foldamer 1, collected in tetrahydrofuran with 300 nm pump and 470 nm LED exposure.

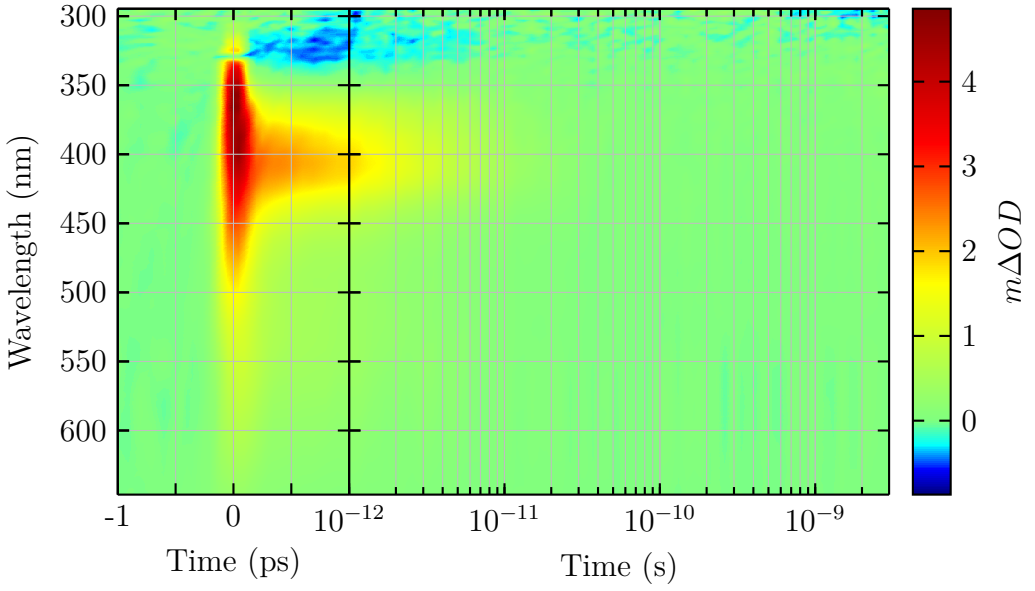


**Figure 7.9** Foldamer 1, with 10 eq of chloride collected in 1:1 acetonitrile:tetrahydrofuran with 300 nm pump and 470 nm LED exposure.

# Half foldamer 2

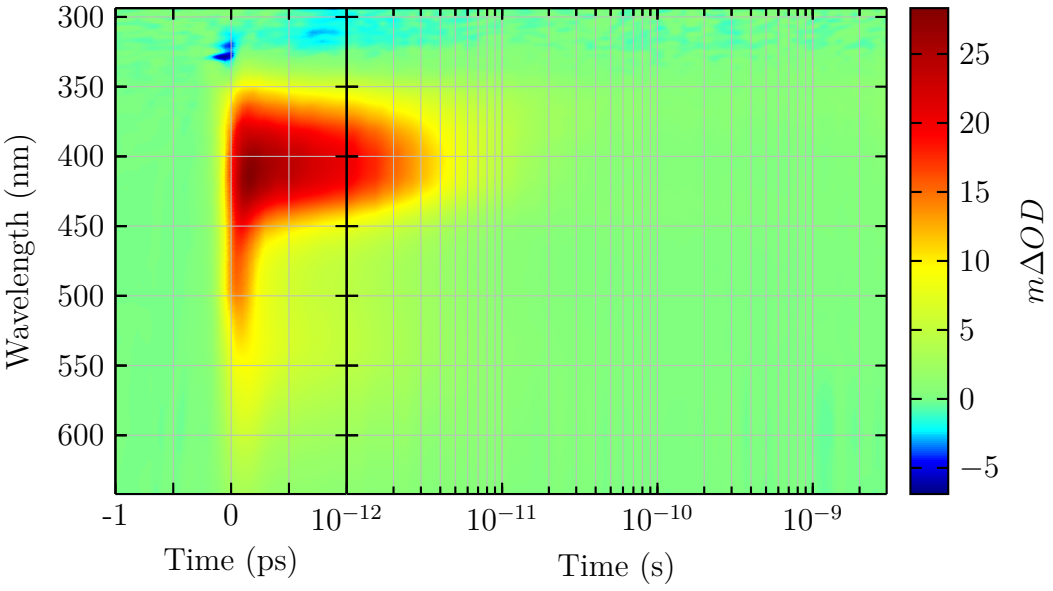


**Figure 7.10** Half foldamer 2, collected in acetonitrile with 300 nm pump and 470 nm LED exposure.

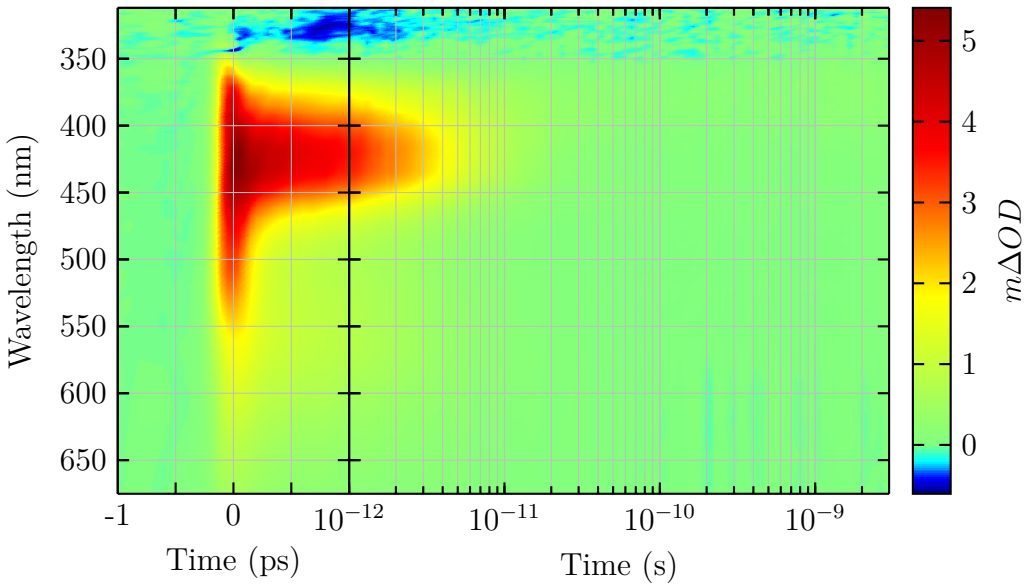


**Figure 7.11** Half foldamer 2, collected in 1:1 acetonitrile:tetrahydrofuran with 300 nm pump and 470 nm LED exposure.

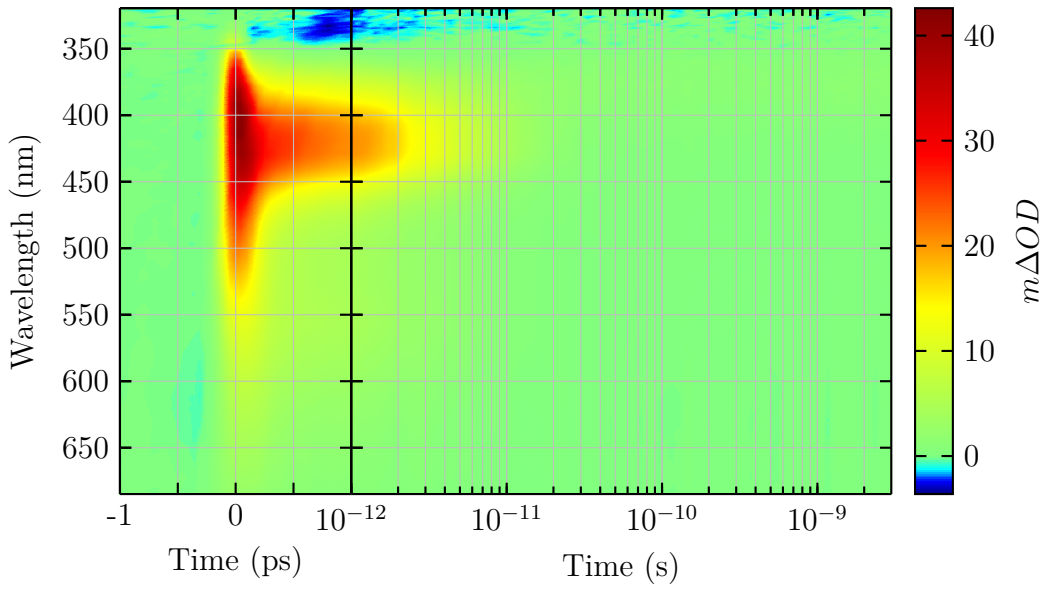


**Figure 7.12** Half foldamer 2, collected in tetrahydrofuran with 300 nm pump and 470 nm LED exposure.

# Foldamer 2

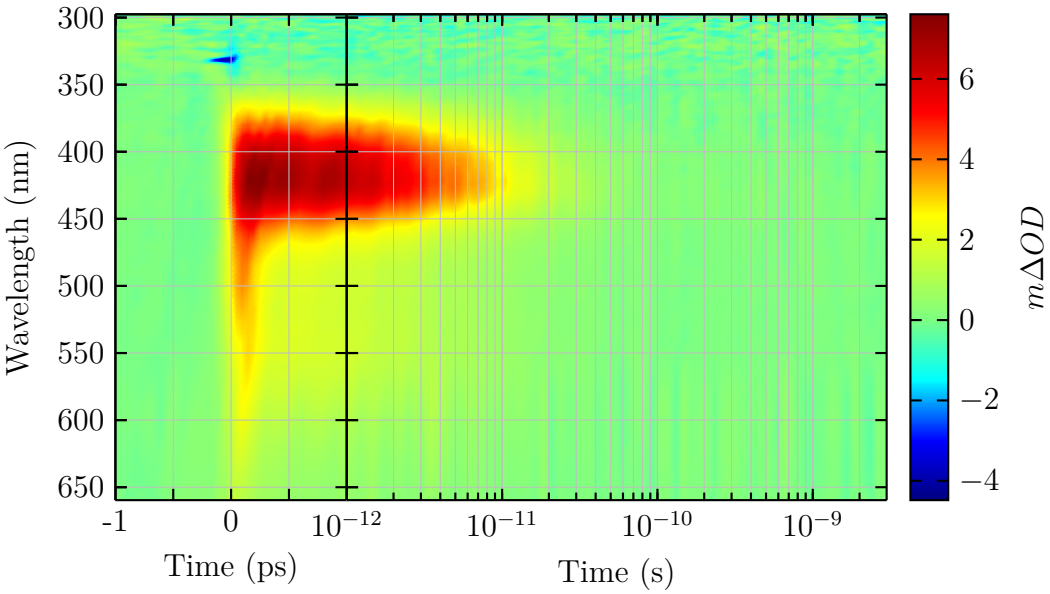


**Figure 7.13** Foldamer 2, collected in acetonitrile with 300 nm pump and 470 nm LED exposure.

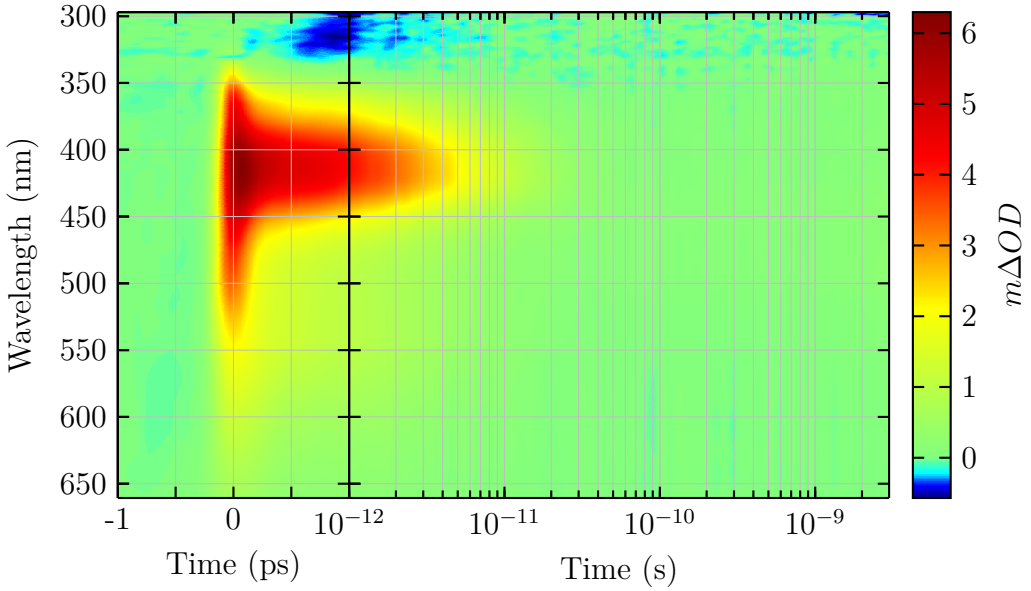


**Figure 7.14** Foldamer 2, collected in 1:1 acetonitrile:tetrahydrofuran with 300 nm pump and 470 nm LED exposure.

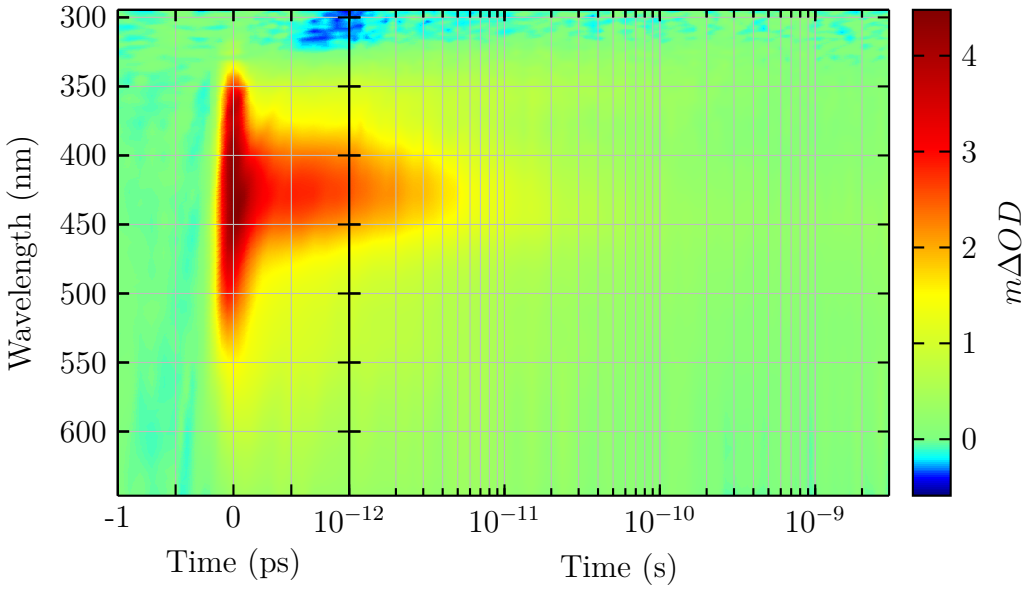


**Figure 7.15** Foldamer 2, collected in tetrahydrofuran with 300 nm pump and 470 nm LED exposure.

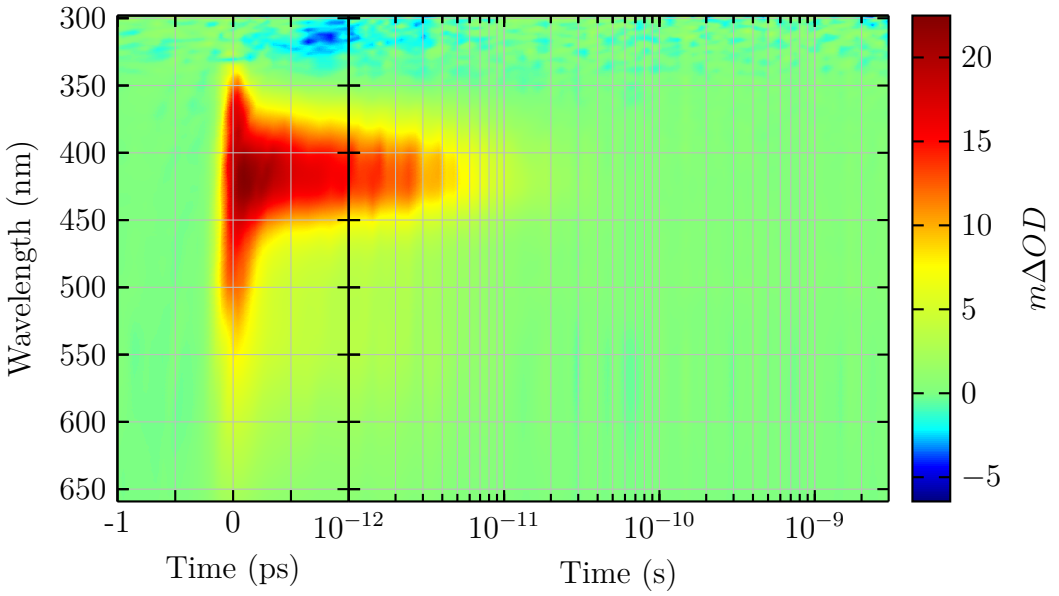


**Figure 7.16** Foldamer 2, with 10 eq of chloride collected in 1:1 acetonitrile:tetrahydrofuran with 300 nm pump and 470 nm LED exposure.

## Oxazine

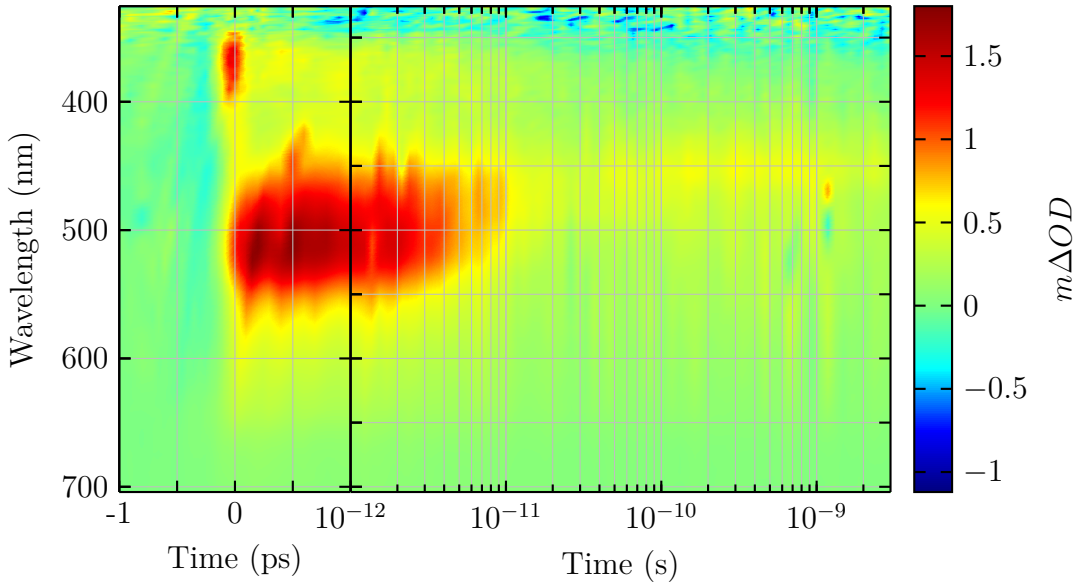


**Figure 7.17** Oxazine, collected in ethanol with 300 nm pump.

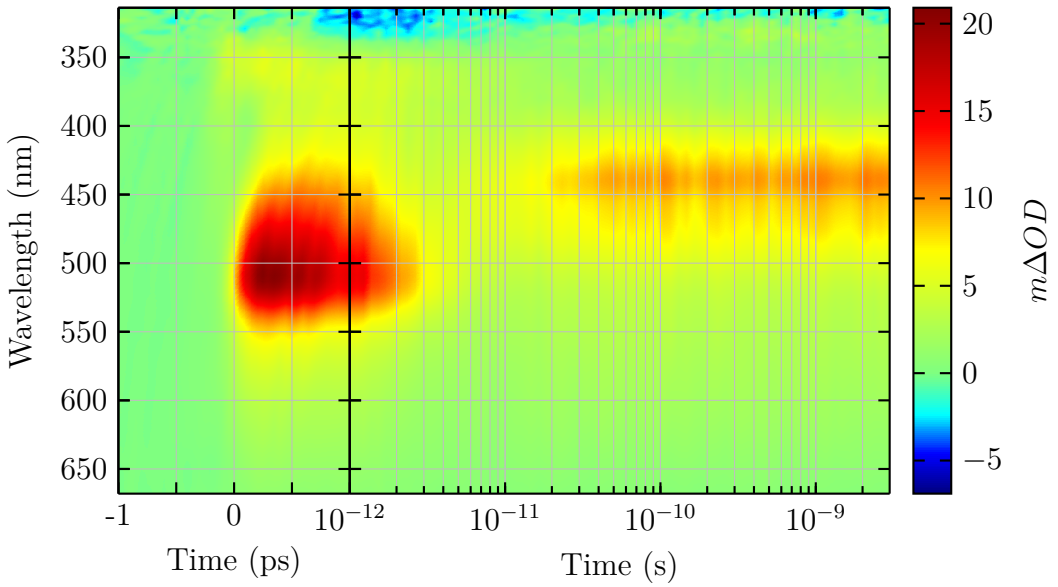


**Figure 7.18** Oxazine, collected in acetonitrile with 300 nm pump.

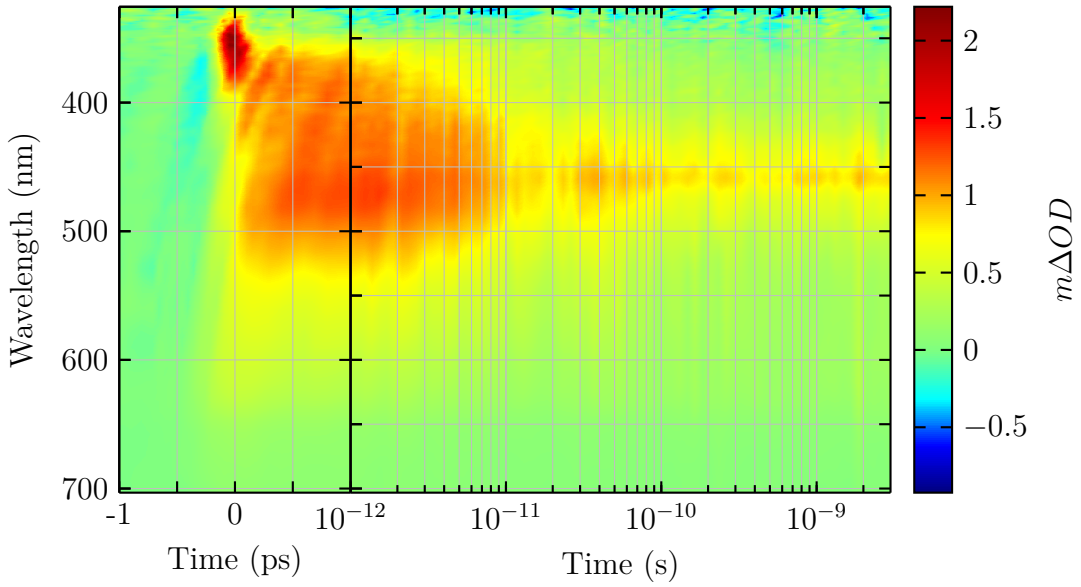


**Figure 7.19** Oxazine, collected in dichloromethane with 300 nm pump.

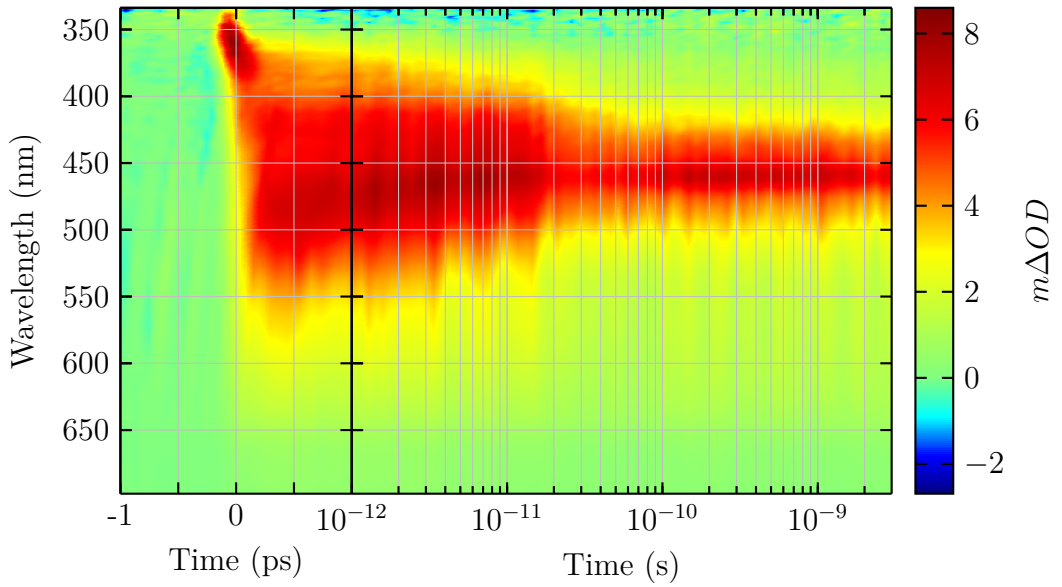


**Figure 7.20** Oxazine, collected in chloroform with 300 nm pump.

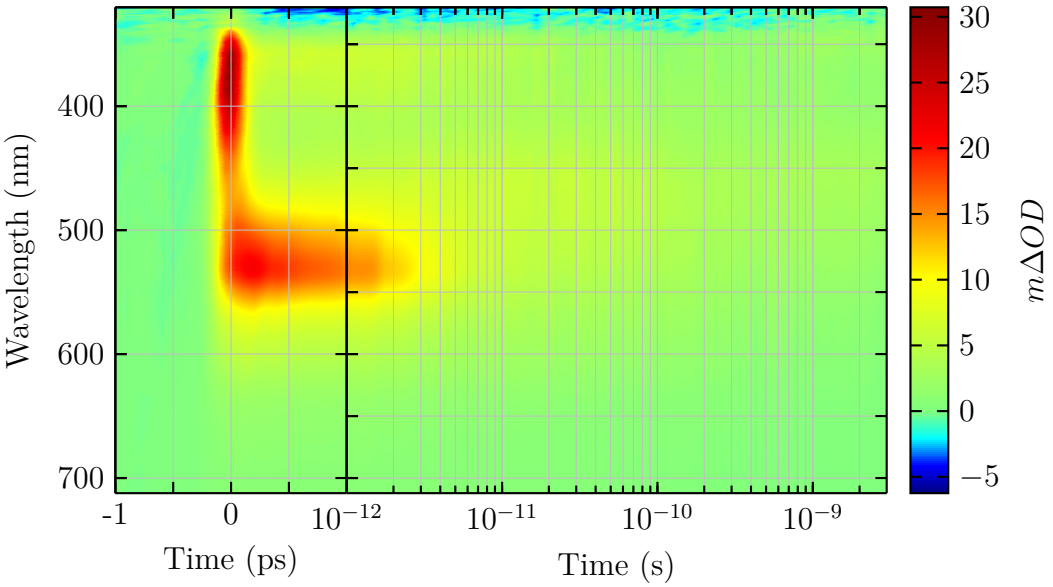


**Figure 7.21** Oxazine, collected in tetrahydrofuran with 300 nm pump.

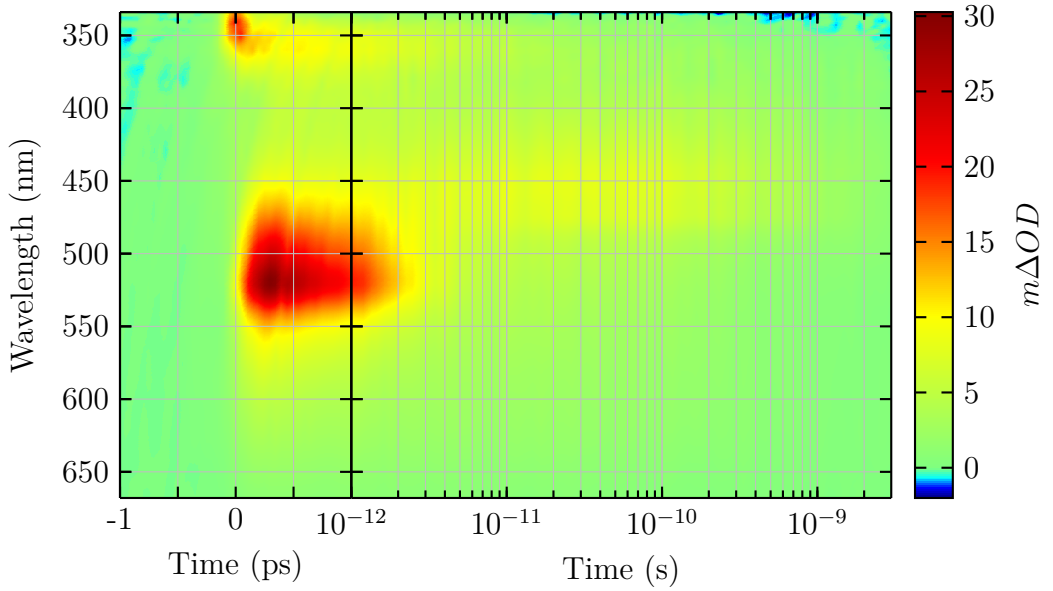


**Figure 7.22** Oxazine, collected in hexane with 300 nm pump.

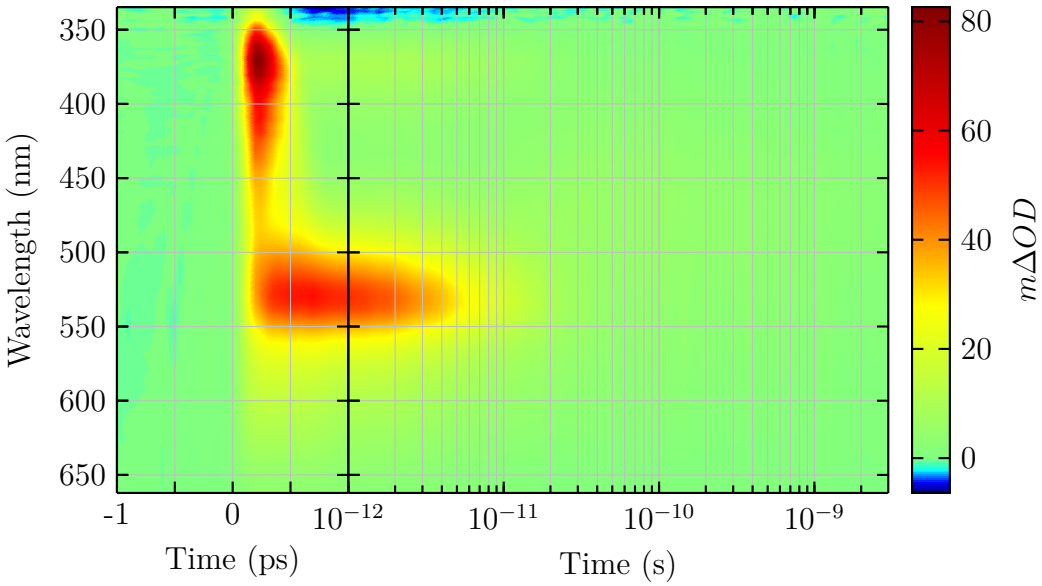


**Figure 7.23** Oxazine, collected in dimethlysuphoxide with 300 nm pump.

## Difluoro–oxazine

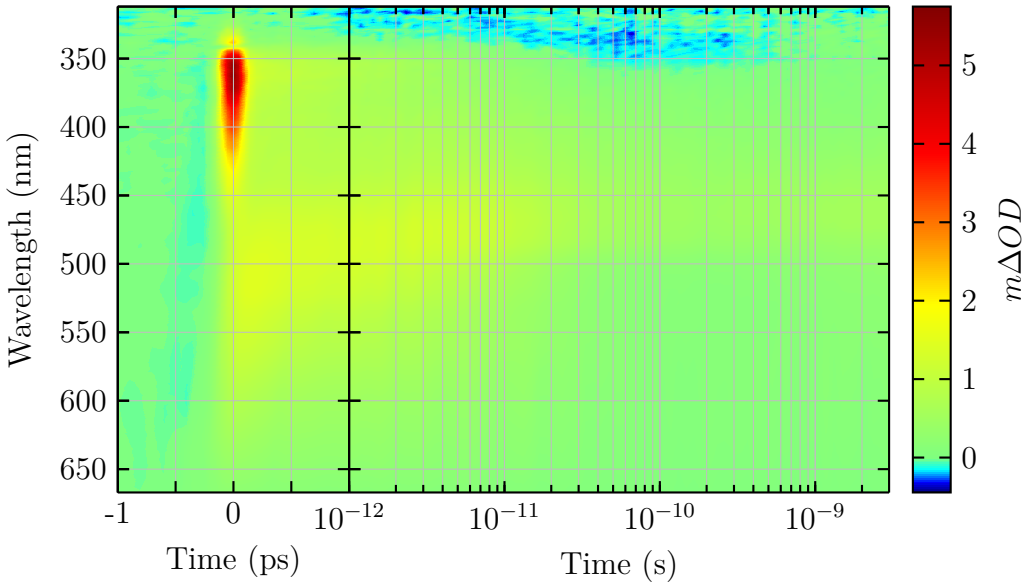


**Figure 7.24** Difluoro–oxazine, collected in ethanol with 300 nm pump.

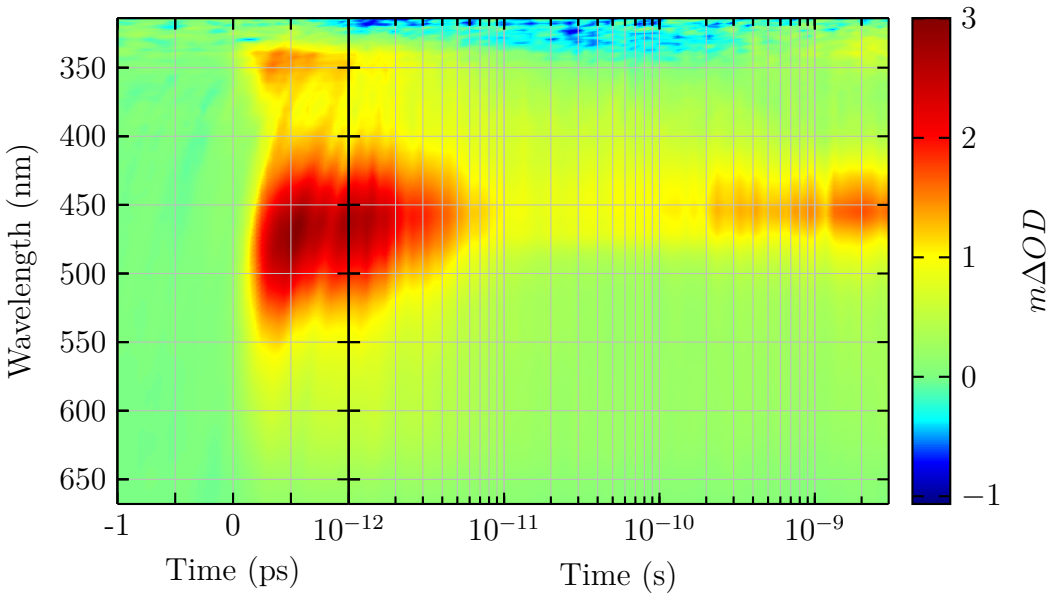


**Figure 7.25** Difluoro–oxazine, collected in acetonitrile with 300 nm pump.

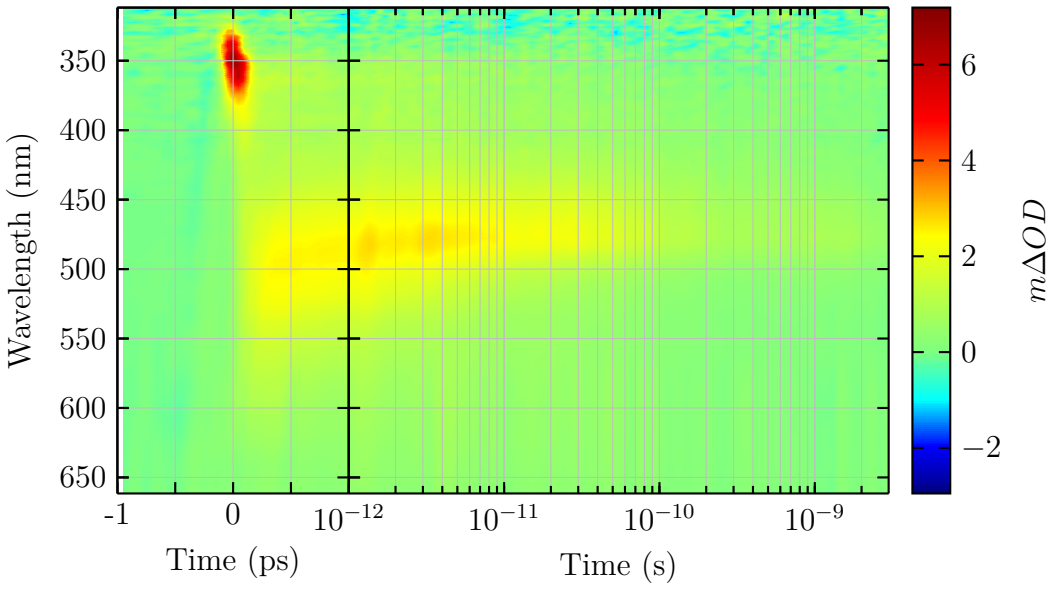


**Figure 7.26** Difluoro–oxazine, collected in dichloromethane with 300 nm pump.

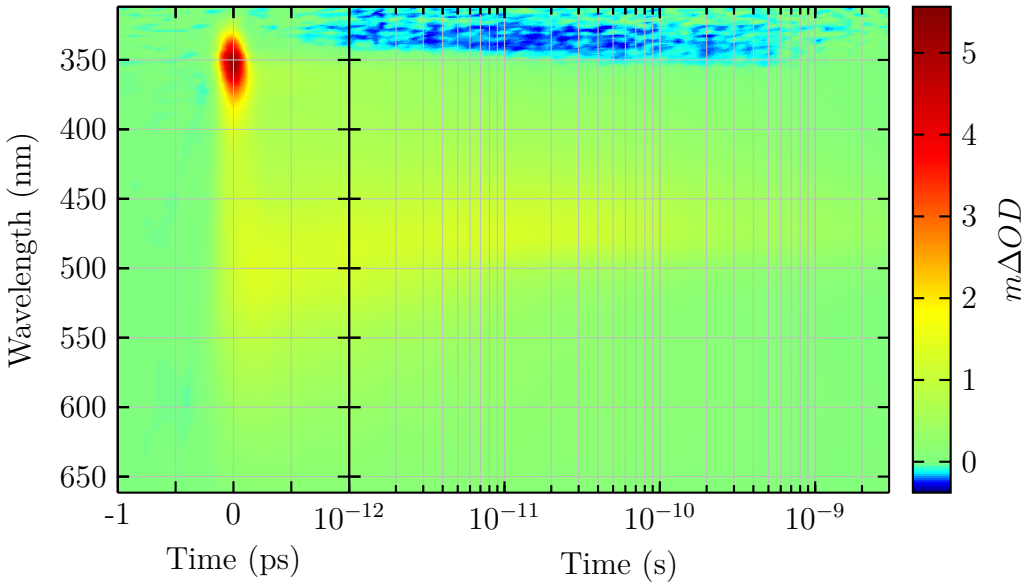


**Figure 7.27** Difluoro–oxazine, collected in chloroform with 300 nm pump.

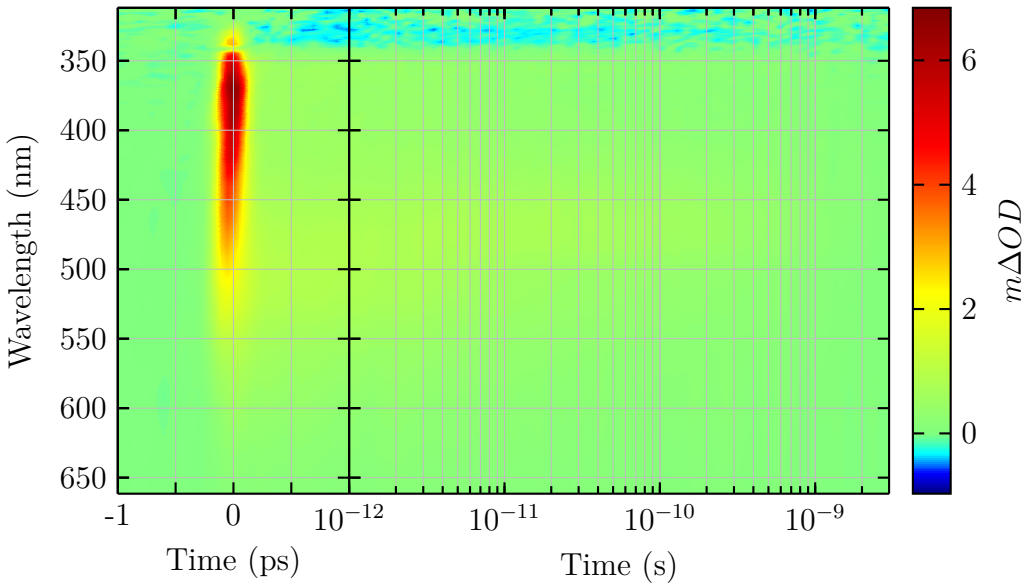


**Figure 7.28** Difluoro–oxazine, collected in tetrahydrofuran with 300 nm pump.

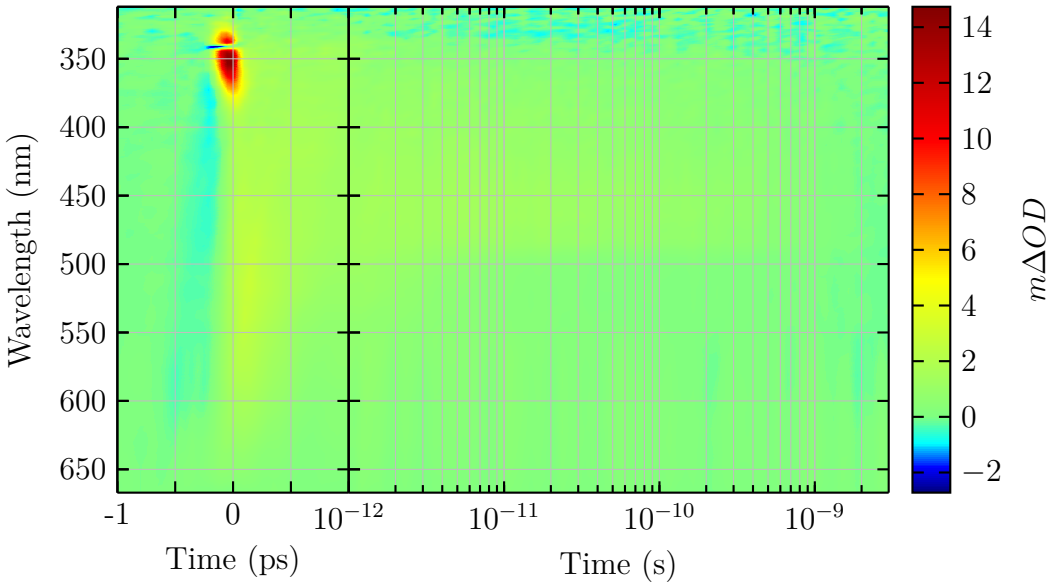


**Figure 7.29** Difluoro–oxazine, collected in hexane with 300 nm pump.

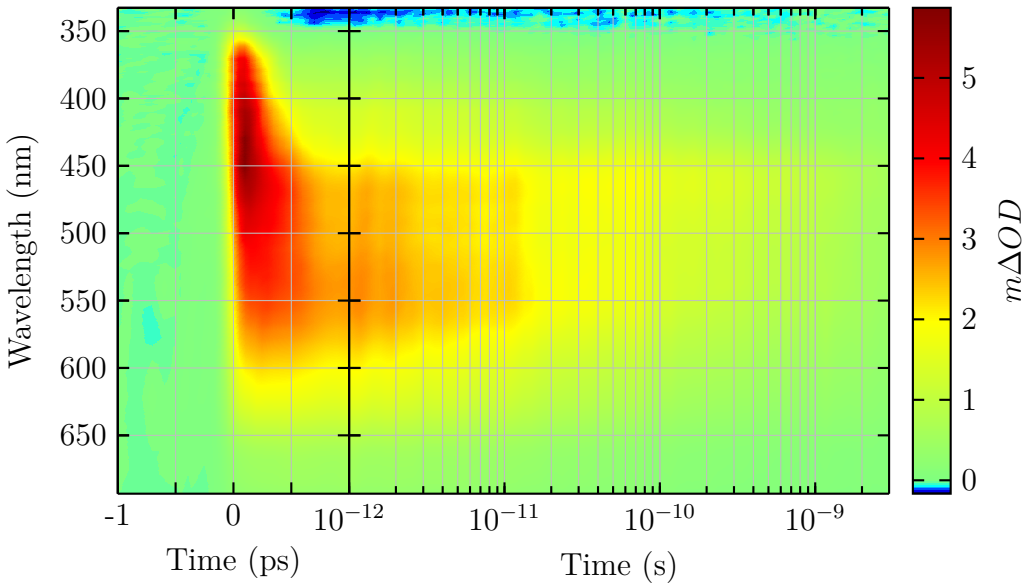


**Figure 7.30** Difluoro–oxazine, collected in dimethlysuphoxide with 300 nm pump.

# References


1. Klok, M.; Boyle, N.; Pryce, M. T.; Meetsma, A.; Browne, W. R. et al. *J. Am. Chem. Soc.* **2008**, *130*, 10484–5.
2. Murakami, H.; Kawabuchi, A.; Matsumoto, R.; Ido, T.; Nakashima, N. *J. Am. Chem. Soc.* **2005**, *127*, 15891–9.
3. Dawson, R. E.; Lincoln, S. F.; Easton, C. J. *Chem. Commun.* **2008**, 3980–2.
4. Ferris, D. P.; Zhao, Y.-L.; Khashab, N. M.; Khatib, H. a.; Stoddart, J. F. et al. *J. Am. Chem. Soc.* **2009**, *131*, 1686–8.
5. Liu, D.; Xie, Y.; Shao, H.; Jiang, X. *Angew. Chem. Int. Ed. Engl.* **2009**, *48*, 4406–8.
6. Florea, L.; Scarmagnani, S.; Benito-Lopez, F.; Diamond, D. *Chem. Commun.* **2014**, *50*, 924–6.
7. Ipe, B. I.; Mahima, S.; Thomas, K. G. *J. Am. Chem. Soc.* **2003**, *125*, 7174–5.
8. Benito-Lopez, F.; Scarmagnani, S.; Walsh, Z.; Paull, B.; Macka, M. et al. *Sensors Actuators B Chem.* **2009**, *140*, 295–303.
9. Byrne, R.; Ventura, C.; Benito Lopez, F.; Walther, A.; Heise, A. et al. *Biosens. Bioelectron.* **2010**, *26*, 1392–8.
10. Hayashi, S.; Tajkhorshid, E.; Schulten, K. *Biophys. J.* **2009**, *96*, 403–16.
11. Megerle, U.; Pugliesi, I.; Schriever, C.; Sailer, C. F.; Riedle, E. *Appl. Phys. B* **2009**, *96*, 215–231.
12. Hua, Y.; Flood, A. H. *J. Am. Chem. Soc.* **2010**, *132*, 12838–40.
13. Lednev, I. K.; Ye, T.-Q.; Hester, R. E.; Moore, J. N. *J. Phys. Chem.* **1996**, *100*, 13338–13341.
14. Fujino, T.; Arzhantsev, S. Y.; Tahara, T. *J. Phys. Chem. A* **2001**, *105*, 8123–8129.
15. Nägele, T.; Hoche, R.; Zinth, W.; Wachtveitl, J. *Chem. Phys. Lett.* **1997**, *2614*.
16. Rau, H. *Photoreact. Org. Thin Film.*; 2002; Vol. 1.
17. Satzger, H.; Root, C.; Braun, M. *J. Phys. Chem. A* **2004**, 6265–6271.
18. Dobryakov, A. L.; Kovalenko, S. A.; Weigel, A.; Pérez-Lustres, J. L.; Lange, J. et al. *Rev. Sci. Instrum.* **2010**, *81*, 113106.

19. Berera, R.; van Grondelle, R.; Kennis, J. T. M. *Photosynth. Res.* **2009**, *101*, 105–18.

20. van Stokkum, I. H. M.; Larsen, D. S.; van Grondelle, R. *Biochim. Biophys. Acta* **2004**, *1657*, 82–104.

21. Ruckebusch, C.; Sliwa, M.; Pernot, P.; de Juan, A.; Tauler, R. *J. Photochem. Photobiol. C Photochem. Rev.* **2012**, *13*, 1–27.

22. Foggi, P.; Bussotti, L.; Neuwahl, F. V. R. *Int. J. Photoenergy* **2001**, *3*, 103–109.

23. Maciejewski, A.; Naskrecki, R.; Lorenc, M.; Ziolek, M.; Karolczak, J. et al. *J. Mol. Struct.* **2000**, *555*, 1–13.

24. Bradler, M.; Baum, P.; Riedle, E. *Appl. Phys. B* **2009**, *97*, 561–574.

25. Chang, C.-W.; Lu, Y.-C.; Wang, T.-T.; Diau, E. W.-G. *J. Am. Chem. Soc.* **2004**, *126*, 10109–18.

26. Tamai, N.; Miyasaka, H. *Chem. Rev.* **2000**, *100*, 1875–1890.

27. Dietzek, B.; Pascher, T.; Sundström, V.; Yartsev, a. *Laser Phys. Lett.* **2007**, *4*, 38–43.

28. Lorenc, M.; Ziolek, M.; Naskrecki, R.; Karolczak, J.; Kubicki, J. et al. *Appl. Phys. B Lasers Opt.* **2002**, *74*, 19–27.

29. Devos, O.; Mouton, N.; Sliwa, M.; Ruckebusch, C. *Anal. Chim. Acta* **2011**, *705*, 64–71.

30. Kovalenko, S.; Dobryakov, a.; Ruthmann, J.; Ernsting, N. *Phys. Rev. A* **1999**, *59*, 2369–2384.

31. Ekvall, K.; der Meulen, P. V. *J. Appl. Phys.* **2000**,

32. Neelakantan, P. *Proc. Indian Acad. Sci. - Sect. A* **1964**, 422–425.

33. Boyd, R. *Nonlinear optics*; 2002.

34. Tzankov, P.; Buchvarov, I.; Fiebig, T. *Opt. Commun.* **2002**, *203*, 107–113.

35. Brodeur, A.; Chin, S. *Phys. Rev. Lett.* **1998**, *80*, 4406–4409.

36. Brodeur, A.; Chin, S. L. *J. Opt. Soc. Am. B* **1999**, *16*, 637.

37. Petrov, V.; Ghotbi, M.; Kokabee, O.; Esteban-Martin, a.; Noack, F. et al. *Laser Photon. Rev.* **2010**, *4*, 53–98.

38. Krylov, V.; Gallus, J.; Wild, U.; Kalintsev, A.; Rebane, A. *Appl. Phys. B Lasers Opt.* **2000**, *70*, 163–168.

39. Couairon, A.; Mysyrowicz, A. *Phys. Rep.* **2007**, *441*, 47–189.

40. Kandidov, V.; Kosareva, O.; Golubtsov, I.; Liu, W.; Becker, A. et al. *Appl. Phys. B Lasers Opt.* **2003**, *77*, 149–165.

41. Nagura, C.; Suda, A.; Kawano, H.; Obara, M.; Midorikawa, K. *Appl. Opt.* **2002**, *41*, 3735–42.

42. Johnson, P. J. M.; Prokhorenko, V. I.; Miller, R. J. D. *Opt. Express* **2009**, *17*, 21488–96.

43. Ruckebusch, C.; Sliwa, M.; Réhault, J.; Naumov, P.; Huvenne, J. P. et al. *Anal. Chim. Acta* **2009**, *642*, 228–34.

44. Enderlein, J.; Erdmann, R. *Opt. Commun.* **1997**, *134*.

45. Yager, K. G.; Barrett, C. J. *J. Photochem. Photobiol. A Chem.* **2006**, *182*, 250–261.

46. Beharry, A. A.; Woolley, G. A. *Chem. Soc. Rev.* **2011**, *40*, 4422–37.

47. Woolley, G. A. *Nat. Chem.* **2012**, *4*, 75–7.

48. Fischer, E. *J. Phys. Chem.* **1967**, *71*, 3704–3706.

49. Bortolus, P.; Monti, S. *J. Phys. Chem.* **1979**, *83*, 648–652.

50. Bandara, H. M. D.; Friss, T. R.; Enriquez, M. M.; Isley, W.; Incarvito, C. et al. *J. Org. Chem.* **2010**, *75*, 4817–27.

51. Bandara, H. M. D.; Burdette, S. C. *Chem. Soc. Rev.* **2012**, *41*, 1809–25.

52. Schultz, T.; Quenneville, J.; Levine, B.; Toniolo, A.; Martínez, T. J. et al. *J. Am. Chem. Soc.* **2003**, *125*, 8098–9.

53. Wei-Guang Diau, E. *J. Phys. Chem. A* **2004**, *108*, 950–956.

54. Dias, A. *J. Chem. Thermodyn.* **1992**, *24*, 439–447.

55. Gille, K.; Knoll, H.; Quitzsch, K. *Int. J. Chem. Kinet.* **1999**, 337–350.

56. Whitten, D.; Wildes, P. *J. Am. Chem. Soc.* **1971**, *1192*, 2004–2008.

57. Ciccone, S.; Halpern, J. *Can. J. Chem.* **1959**, *37*.

58. Lednev, I.; Ye, T.; Matousek, P.; Towrie, M. *Chem. Phys. Lett.* **1998**, 68–74.

59. Hoffman, D. P.; Mathies, R. A. *Phys. Chem. Chem. Phys.* **2012**, *14*, 6298–6306.

60. Hamm, P.; Ohline, S.; Zinth, W. *J. Chem. Phys.* **1997**, *106*.

61. Lee, S.; Hua, Y.; Flood, A. *Unpublished Manuscript* **2012**,

62. Lee, S.; Flood, A. H. *J. Phys. Org. Chem.* **2013**, *26*, 79–86.

63. Hua, Y.; Liu, Y.; Chen, C.-H.; Flood, A. H. *J. Am. Chem. Soc.* **2013**, *135*, 14401–12.

64. McDonald, K. P.; Hua, Y.; Lee, S.; Flood, A. H. *Chem. Commun.* **2012**, *48*, 5065–75.

65. Wang, Y.; Bie, F.; Jiang, H. *Org. Lett.* **2010**, *12*, 3630–3.

66. Hua, Y.; Ramabhadran, R. O.; Uduehi, E. O.; Karty, J. a.; Raghavachari, K. et al. *Chemistry* **2011**, *17*, 312–21.

67. Juwarker, H.; Lenhardt, J. M.; Pham, D. M.; Craig, S. L. *Angew. Chem. Int. Ed. Engl.* **2008**, *47*, 3740–3.

68. Juwarker, H.; Jeong, K.-S. K. *Chem. Soc. Rev.* **2010**, *39*, 3664–74.

69. Wenzel, M.; Hiscock, J. R.; Gale, P. a. *Chem. Soc. Rev.* **2012**, *41*, 480–520.

70. Tomasulo, M.; Sortino, S.; Raymo, F. *Org. Lett.* **2005**, 4496–4498.

71. Tomasulo, M.; Sortino, S.; White, A. J. P.; Raymo, F. M. *J. Org. Chem.* **2005**, *70*, 8180–9.

72. Szaciłowski, K. *Chem. Rev.* **2008**, *108*, 3481–548.

73. Deniz, E.; Tomasulo, M.; Cusido, J.; Sortino, S.; Raymo, F. M. *Langmuir* **2011**, *27*, 11773–83.

74. Tomasulo, M.; Sortino, S.; Raymo, F. M. *J. Photochem. Photobiol. A Chem.* **2008**, *200*, 44–49.

75. Deniz, E.; Tomasulo, M.; Sortino, S.; Raymo, F. M. *J. Phys. Chem. C* **2009**, *113*, 8491–8497.

76. Raymo, F. M. *J. Phys. Chem. A* **2012**, *116*, 11888–95.

77. Krysanov, S.; Alfimov, M. *Chem. Phys. Lett.* **1982**, *91*.

78. Monti, S.; Malatesta, V. *Photochem. Photobiol.* **1996**, *64*, 87–91.

79. Barkauskas, M. *Lith. J. Phys.* **2008**, *48*, 231–242.

80. Lakowicz, J. *Principles of fluorescence spectroscopy*; 2007.

81. Bauer, D. R.; Brauman, J. I.; Pecora, R. *J. Am. Chem. Soc.* **1974**, *96*, 6840–6843.

82. Hay, C. E.; Marken, F.; Blanchard, G. J. *J. Phys. Chem. A* **2010**, *114*, 4957–62.

83. Saltiel, J.; Wang, S.; Ko, D.-h.; Gormin, D. A. *J. Phys. Chem. A* **1998**, *102*, 5383–5392.

84. Kirsch, A. D.; Wyman, G. M. *J. Phys. Chem.* **1977**, *81*, 413–420.

85. Görner, H. *Chem. Phys. Lett.* **1998**, *282*, 381–390.

86. Tahara, T.; Toleutaev, B. N.; Hamaguchi, H.-o. *J. Chem. Phys.* **1994**, *100*, 786.

87. Matyushov, D. V.; Schmid, R.; Ladanyi, B. M. *J. Phys. Chem. B* **1997**, *101*, 1035–1050.

88. Shakerizadeh-Shirazi, F.; Hemmateenejad, B.; Mehranpour, A. M. *Anal. Methods* **2013**, *5*, 891.